AN ABSTRACT OF THE THESIS OF

Bethany E. Matthews for the degree of Doctor of Philosophy in Physics presented on September 18, 2018.

Title: Synthesis and Analysis of Heterostructural Semiconductor Alloy $Sn_{1-x}Ca_xCh$ (Ch=S, Se) and Nitrides $Zn_{1-x}W_xN$ and $Zn_{1-x}(W_{1-y}Mo_y)_xN$

Abstract approved: _____
Janet Tate

This work explores the synthesis and characterization of the metastable alloys $Sn_{1-x}Ca_xCh$ (Ch= S, Se) and nitride compounds Zn-W-Mo-N, which have recently been predicted by theorists. Single phase thin films of $Sn_{1-x}Ca_xS$ are prepared by pulsed laser deposition and radio-frequency magnetron sputtering and of $Sn_{1-x}Ca_xSe$ are prepared by pulsed laser deposition. A transition from the rock salt cubic structure at high Ca concentrations to the orthorhombic structure at lower Ca is observed at $x = 0.25$ for the sulfide and $x = 0.18$ for the selenide. Optical bandgaps for both $Sn_{1-x}Ca_xCh$ alloys follow nonlinear trends with a discontinuity near the transition composition range from $1.5 - 2.45$ eV and $0.6 - 3.5$ eV for $Sn_{1-x}Ca_xS$ and $Sn_{1-x}Ca_xSe$ respectively. $Sn_{1-x}Ca_xS$ samples were highly resistive, yielding resistivities of $10^2 - 10^4$ Ωcm at low Ca concentrations ($x < 0.1$) and increasing rapidly with added Ca. $Sn_{1-x}Ca_xSe$ samples were much more conductive with resistivities $10^{-2} - 5 \times 10^1$ Ωcm over the range of compositions ($0 < x < 1$) and exhibited excellent thermoelectric properties with a power factor PF = 2 $\mu W cm^{-1}K^{-2}$ at $x = 0.16$. The phase decomposition of these alloys is also explored using STEM EDS (scanning transmission electron microscopy energy dispersive x-ray spectroscopy).

Thin films of nitride compounds Zn-W-N and Zn-Mo-W-N are deposited by RFMS and the range of compositions for stabilization of the predicted wurtzite phase (at Zn_3WN_4) is tested. Single phase crystalline WZ samples were obtained between $60 - 87\%$ and $50 - 84\%$ Zn cation percent for the Zn-W-N and Zn-Mo-W-N systems respectively. Optical absorption for samples is calculated from measured transmission and reflectance for $800 < \lambda < 1100$ nm, and samples at low Zn percentages are more absorbing in the IR than at higher Zn. Resistivities are measured for all

films and found to be $10^3 - 10^5$ and $10^{-1} - 10^5$ Ωcm for Zn-W-N and Zn-W-Mo-N respectively. Composition uniformity and crystalline uniformity are explored by STEM EDS and TEM respectively. WZ phase films were found to be compositionally uniform, but films at lower Zn concentrations (around 30% Zn) tended to phase separate.

The experimental work presented here shows the viability of computational predictions of metastable materials and materials searches in alternative materials space to expand the number of known materials and understanding of metastable materials.

Synthesis and Analysis of Heterostructural Semiconductor Alloy $Sn_{1-x}Ca_xCh$ (Ch=S, Se) and Nitrides $Zn_{1-x}W_xN$ and $Zn_{1-x}(W_{1-y}Mo_y)_xN$

by
Bethany E. Matthews

A DISSERTATION

submitted to

Oregon State University

in partial fulfillment of
the requirements for the
degree of

Doctor of Philosophy

Presented September 18, 2018
Commencement June 2019

Doctor of Philosophy dissertation by Bethany E. Matthews presented on September 18, 2018.

APPROVED:

_____

Major Professor, representing Physics

_____

Chair of the Department of Physics

_____

Dean of the Graduate School

I understand that my dissertation will become part of the permanent collection of Oregon State University libraries. My signature below authorizes release of my dissertation to any reader upon request.

_____

Bethany E. Matthews, Author

ACKNOWLEDGEMENTS

I would like to acknowledge Janet Tate as one of the greatest scientists I've met and the best adviser I could have asked for. She knows how to work with other scientists and stay on task and has turned out some amazing scientists. She gave me the freedom to pursue my own interests and supported me when they extended to areas of science she didn't have expertise in. I would like to thank her for funding me through the CNGMD EFRC. It was the source of so many good experiences, and I learned far more working with Andriy Zakutayev, Laura Schelhas, Aaron Holder, Sebastian Siol, Brian Gorman, Stephan Lany, Elisabetta Arca and everyone else than I ever could have alone. I would also like to thank the other members of Janet's group: James Haggerty, Okan Agirseven, David Rivella, Chris Reidy for making a welcoming office always ready to talk about science or politics or just life in general. Thanks for making the last five years bearable and even fun, I look forward to seeing what you will become. I would like to also thank all the undergraduates Josh Mutch, James May, Michael Forkner, Aaron Dethlefs, Ryan Lance, Patrick Berry, and Kelda Diffendaffer for all the help with collecting data and for all the conversations about equipment; you all really helped me understand the equipment with your questions. I thank Peter Eschbach for always patiently teaching me about electron microscopy, something I never would have thought I would be so passionate to study, and for speaking well of me. I would like to thank Robert Kokenyesi for being so cheerful when answering my incessant questions about XRD and PLD, I would have been very lost without your help. I would also like to thank my classmates, the first year was rough, but you were all so encouraging and full of good jokes. I want to thank Allison Gicking for being so passionate about diversity. I had not thought that things even needed changing nor about how quickly things could change when you group together to work for something. I thank my brother Jonathan for putting up with me through my ups and downs and always knowing how to make me smile. You're going to do great things someday. Thanks to my sister Rebecca (and Mike) for providing me with two wonderful nephews to have fun with in my spare time, and thanks to my brother (and Jessica) for the new niece I thought I would never have! I would also like to thank my DnD group: Dan, Pernell, Jeff, Scott, Jon, and Jacob, I never thought I could have so much fun with imaginary people! I would also like to thank Erika Hanselman Green for giving me the chance to teach BodyPump at Dixon; it was a life-changing experience. I gained so much confidence and strength from it. I thank my ballet teacher Penny King for teaching me the discipline, patience, and grit required for ballet; it helped

me so much. I also want to acknowledge my mom for working so hard to give her kids the best education and for teaching me to be curious and my dad for consistently checking in on how my research was doing and trying to help even if he didn't quite get it; I don't know where I would be without you. And thanks to my dearest husband Scott Harpool for being so patient with me, for all the late nights and work weekends, for helping deal with my stress even as you were working through your own degree. Thank you for being committed to me. Finally, I want to thank me committee for agreeing so last minute to help me out; it was most gracious!

CONTRIBUTION OF AUTHORS

Aaron Holder and Stephan Lany at National Renewable Energy Laboratory did the all the simulations and calculations for the $Sn_{1-x}Ca_xS$ and $Sn_{1-x}Ca_xSe$ material systems in Chapter 2 and the Zn-W-N system in Chapter 3. Sebastian Siol at National Renewable Energy Laboratory did all the sputtering synthesis of the $Sn_{1-x}Ca_xS$ thin films in Chapter 2 and the XRF, XRD, optical, and resistivity measurements of those films. Brian Gorman prepared and analyzed the $Mn_{1-x}Zn_xO$ and $Sn_{1-x}Ca_xS$ TEM specimen in Chapter 2. Peter Eschbach at Oregon State University and Brian Gorman at Colorado School of Mines helped with the analysis of the $Sn_{1-x}Ca_xSe$ TEM specimen in Chapter 2. James Haggerty and James May in Janet Tate's group assisted in the acquisition and analysis of $Sn_{1-x}Ca_xS$ and $Sn_{1-x}Ca_xSe$ optical data in Chapter 2. Laura Schelhaus ran the synchrotron XRD measurements at the SLAC facility for samples in Chapter 2 and 3. Robert Kokenyesi from Doug Kesaler's group helped prepare the CaSe target used for Chapter 2. John Perkins from National Renewable Energy Laboratory ran the RBS for samples in Chapter 3. Peter Eschbach assisted in conducting and analyzing some EDS and EFTEM measurements in Chapter 3 and 4.

.

TABLE OF CONTENTS

Page

TABLE OF CONTENTS (Continued)

Page

LIST OF FIGURES

Figure Page

LIST OF FIGURES (Continued)

Figure Page

To my dad, I wish you could have seen this.

Chapter 1 Introduction: Metastability

1.1 Background

The exploration for new and innovative materials is an ever-expanding front. Until recently, this exploration has primarily been based around finding, predicting, and explaining ground states of a material system. However, this type of analysis excludes a large category of materials which dominate the library of known materials: metastable materials. Every year increasingly more metastable materials (difference of the blue and green) are discovered and entered into the ISCD relative to ground state materials, which has maintained a relatively flat rate, as illustrated in Figure 1.1, but as yet there is still an untapped, unexplored area of potentially ground-breaking metastable materials. Metastable materials often have useful and desirable properties, such as diamond.

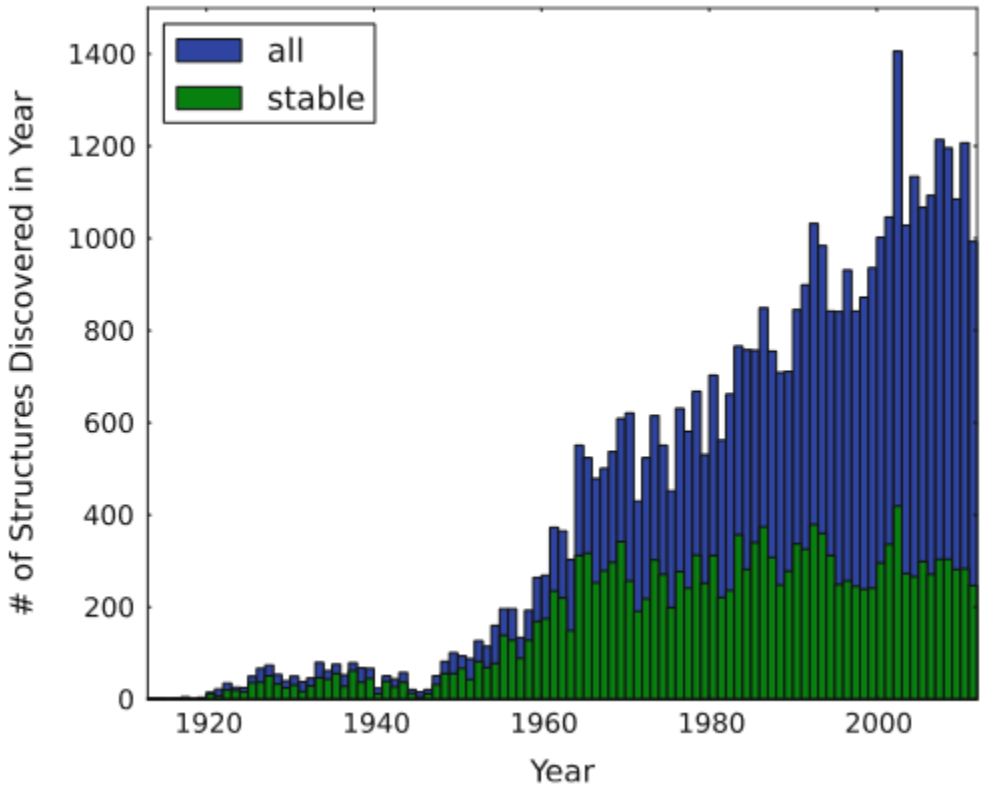

Figure 1.1. Number of materials entered into the ICSD by year for total discovered (blue) and stable (green) materials.[1]

Despite metastable materials being some of the most intriguing, useful, and even common materials, metastability has not been well understood.[2] In order to predict and actively discover new metastable materials, a better understanding of metastability and how to access and control it is needed.

Metastability is often described in terms of an energy landscape or surface, wherein the metastable states are local minima. Biochemists and physicists often describe the folding of proteins and the different conformations or steps in the folding by an energy landscape, similar to the one in Figure 1.2, where the different directions in conformation space are indicative of environmental states or positions for the different parts of the protein. The protein folds by 'falling' into progressively lower metastable states.[3] The energy landscape for materials is often much more simply described by material scientists. Figure 1.3 shows an example with a ground state (green diamond) and the desired metastable state (yellow heart) on an energy surface in configurational space. Two slices

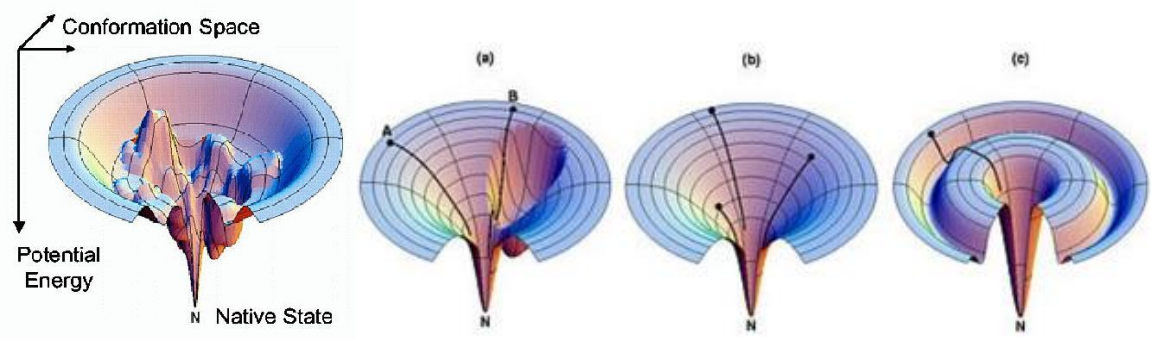

Figure 1.2. Energy surfaces showing different pathways for protein folding.[4]

of configuration space are shown for two instances of pressure (another direction in configuration space) for carbon. In the low-pressure configuration, graphite is the ground state and diamond is metastable, while in the high-pressure state, diamond is the ground state. Manipulation of this energy landscape by high-pressure synthesis is a common method for accessing metastable states, though this method is not conducive to studying metastability in thin films.

In order to better understand metastability, it is important to know what causes metastability or what types of states can be described as metastable. Figure 1.3 shows the convex hull (connected black line) for an arbitrary binary material system, which traces the lowest energy states for different compositions, creating a kind of envelope of phases that are relatively stable compared to the isolated components of the binary (A and X). The states inside this envelope but not on the hull are metastable. Figure 1.3 schematically describes different types of metastable states that commonly occur. Polymorphism is a phenomenon in which different metastable states, corresponding to different crystal structures for the same composition, can be accessed to obtain different properties merely by changing the crystal structure of a given compound. A common example is C as graphite to diamond. Semiconductor alloys are also common phenomena in which

two materials are intermixed and which may allow access to metastable states for property manipulation, such as $In_{1-x}Ga_xAs$ or $Al_{1-x}Sc_xN$. Defect metastable states, such as vacancies on lattice sites or changes in the microstructure, can be one way to control individual properties. For this work, we will discuss semiconductor alloys for metastability.

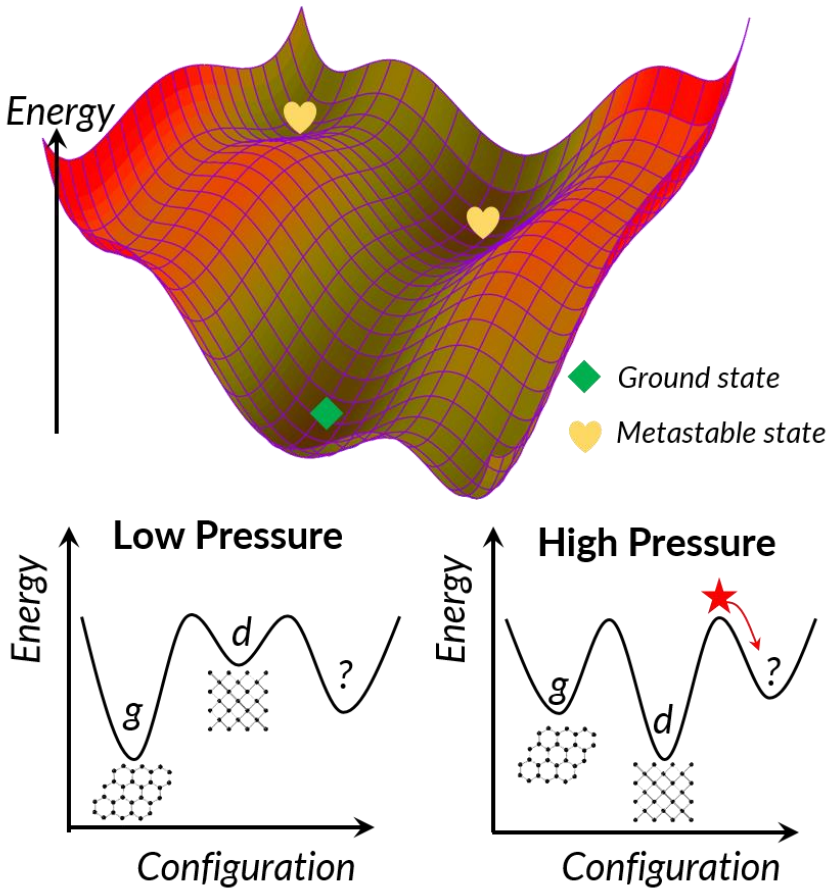

Figure 1.3. Example energy surface for a material and two slices of a energy surface for different pressures in configuration space.[5]

There are two types of semiconductor alloys: isostructural and heterostructural. In isostructural alloying, the crystal structure of the end members is the same as is the structure of the alloy at all compositions. For heterostructural alloying, the two end members may be different, in addition, another crystal structure different from the two end members maybe stabilized. Within heterostructural alloying, there are two different types based on the transition between crystal structures. Heterostructural alloys between two crystal structures were the transition can be

described as continuous and bond-breaking is not required are termed commensurate alloys. Figure 1.4a shows an example of commensurate alloy with a transition from an orthorhombic structure, which is also described as a distorted rock salt structure, to the cubic rock salt structure. The atoms do not have far to move in order to be rearranged into the cubic structure. Alloys for which the structural transition is more abrupt and bond-breaking occurs to put the atoms in the appropriate position for the new structure are called incommensurate alloys. Figure 1.4b is an example of an

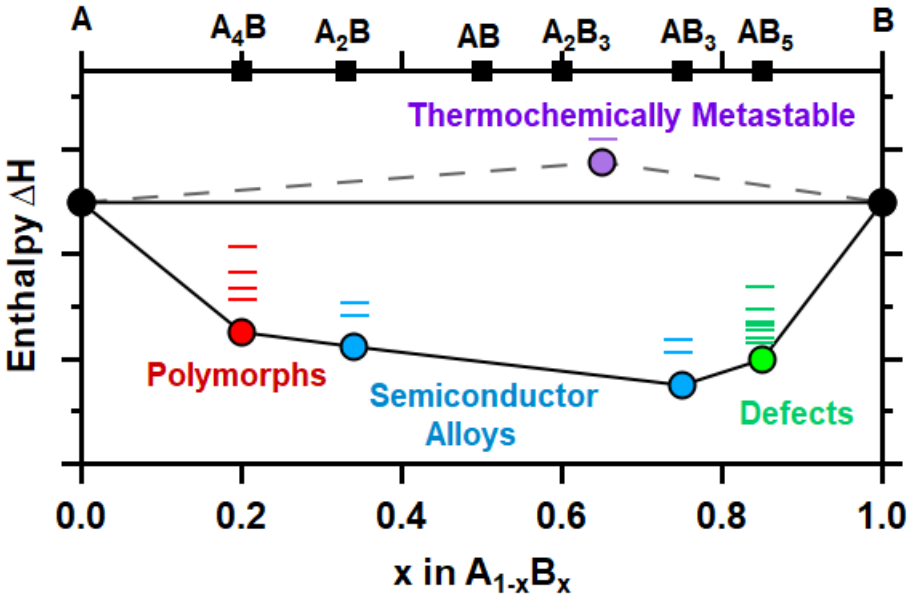

Figure 1.4. Phase diagram for an arbitrary binary material system showing the convex hull and some possible metastable states induced as polymorphs, alloys, or defects.

incommensurate transition between a wurtzite structure to the cubic rock salt structure, which was recently demonstrated by Peng *et al.* in the alloy $Mn_{1-x}Zn_xO$.[6] In this type of alloy, the atoms do not have a clear path to transition to the new structure and bond-breaking must occur to reposition the atoms.

Heterostructural alloys, with their structural transition, are typically quite metastable, frequently having higher energy states than their isostructural brethren which are often stable or close to stable. Therefore, to explore metastable states, their synthesis and what can be gained from them, this work uses the method of heterostructural alloying to access metastable states in a variety of material systems. In order to synthesize these highly metastable materials high temperatures or high energy is required to access the states. To prevent immediate decomposition, kinetic

stabilization was employed in which a high energy technique is used to overcome the high energy barrier and then the material is quickly quenched to ‘freeze in’ the alloyed state. To kinetically stabilize samples, this work used the high energy techniques of pulsed laser deposition and sputtering for synthesis.

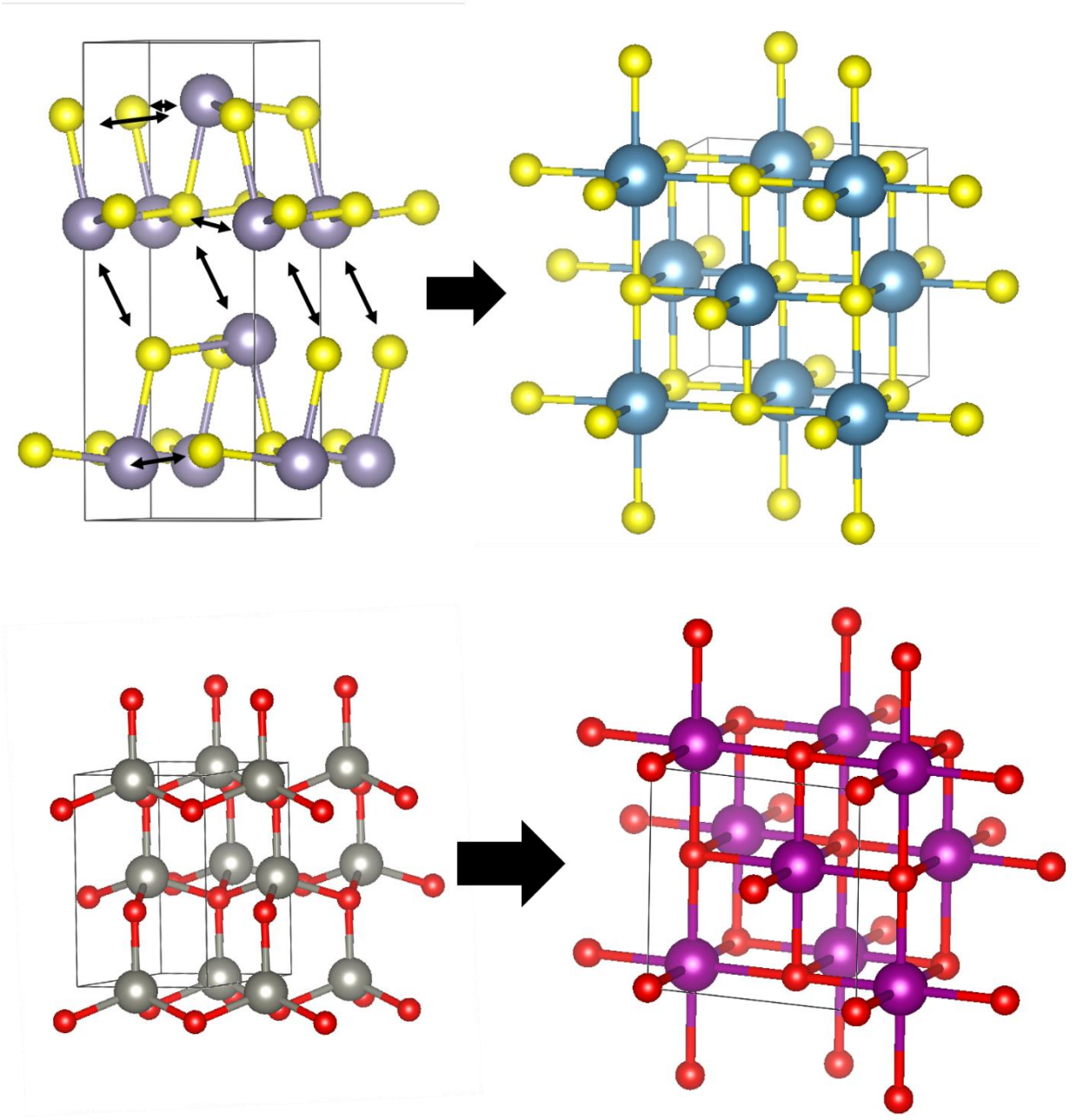

Figure 1.5. a) Commensurate heterostructural alloy transition from orthorhombic (left) to rock salt cubic (right). b) Incommensurate transition from wurtzite (left) to rock salt cubic (right).

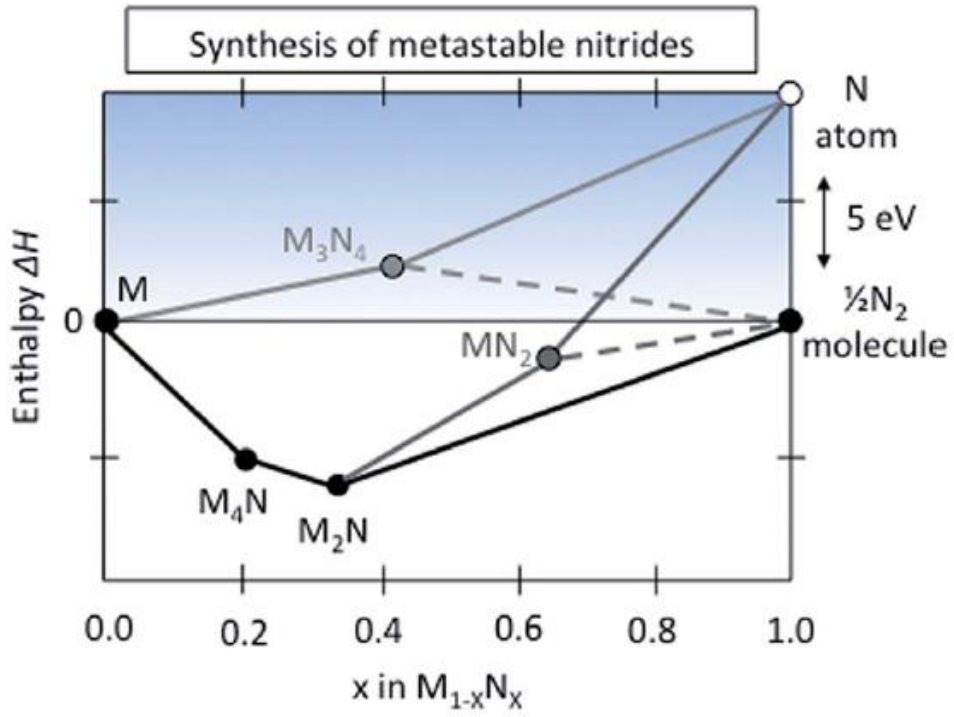

Figure 1.6. Enthalpy of formation for an arbitrary metal nitride system with metastable phases M_2N_4 and MN_2 compared to molecular N (dashed lines) or atomic N (solid lines).[7]

In addition to alloys, nitrides are another family of materials that are often metastable. While some nitrides, such as GaN, are well studied, in general nitrides are far under-explored compared to their oxide brethren. This may be because nitrides seem to have higher formation enthalpies than oxides. A review in 2016 by Andriy Zakutayev[7] showed that when comparing the enthalpies of formation for metal oxides and metal nitrides (e.g. Al_2O_3 and AlN) using molecular O and N, the nitrides had a higher formation energy, but when the formation enthalpies are compared for the oxides and nitrides using atomic O and N, they were comparatively the same. enthalpies of mixing compared to molecular N_2 were often positive (thus highly metastable), but when compared to atomic N the enthalpies were negative. While convex hulls are normally constructed with the more stable versions of an element or compound, Figure 1.6 illustrates the concept that use of atomic N to construct the convex hull changes the relative stability of compounds in the metal nitride system compared to in the convex hull normally constructed with molecular N. The compounds MN_2 and M_3N_4 are metastable or even unstable in the original convex hull (black and dashed lines), but by using atomic N to form the hull, the compounds appear either stable (on the convex hull) or less metastable (closer to the convex hull). This is to show that while nitrides are metastable and may

require high energies for synthesis, maybe even above the end members formation energies, the materials are not necessarily unstable, and can form deep metastable wells.

One goal of this work is to show the viability of avenues of material exploration that previous have not been implemented as often, such as heterostructural alloying and nitride compounds. This work studies metastable alloys containing orthorhombic semiconductors SnS and SnSe, both of which, over the past decade, have been the subject of many studies for their potential as solar absorbers and thermoelectrics, with rock salt insulators CaS and CaSe. Because there has been much interest in making cubic forms of SnS and SnSe,[8],[9],[10] another goal of this work is to stabilize heterostructural alloys $Sn_{1-x}Ca_xCh$, which are predicted to be rock salt cubic for much of the alloy, as single-phase films for the entire range of compositions and to observe the structural transition. To accomplish this goal, alloying between SnS (SnSe) and CaS (CaSe) is performed wherein thin films are synthesized by pulsed laser deposition and radio-frequency magnetron sputtering and the structural and optoelectronic properties measured for the entire range of compositions. A major goal of this work is to test theoretical models of these materials, so the physical properties and trends analyzed here are compared to previously calculated values by theorists, including the metastable phase decomposition pathways.[11,12] The structural transition composition for $Sn_{1-x}Ca_xS$ ($Sn_{1-x}Ca_xSe$) samples was demonstrated to be at $x = 0.25$ ($x = 0.18$), in reasonable agreement with theory. Bandgaps were found to be in the range $1.5 < E_g^i < 2.45$ eV for indirect (range $0.6 < E_g^i < 3.5$ eV for indirect). $Sn_{1-x}Ca_xS$ samples were found to be very resistive even at very low concentrations of Ca, with $\rho = 10^3 - 10^4$ Ωcm at $x = 0.1$, and rapidly increased in resistivity with increasing concentrations of Ca. $Sn_{1-x}Ca_xSe$ samples were much more conductive, with $10^{-2} < \rho < 5 \times 10^2$ Ωcm, and exhibited excellent thermoelectric properties (a room temperature powerfactor of 2 $\mu Wcm^{-1}K^{-2}$ at $x = 0.16$ comparable to the standard high-performance thermoelectric $BiTe_2$ of 2-9 $\mu Wcm^{-1}K^{-2}$).[13] Given the growth conditions for kinetic stabilization, $Sn_{1-x}Ca_xCh$ films were predicted by the phase diagrams to exhibit spinodal phase-decomposition, which was experimentally verified by examination of cross-sectional transition electron microscopy (TEM) samples in scanning TEM energy dispersive x-ray spectroscopy mapping.

In addition to metastable alloys, this work seeks to establish the value of new materials search in metal nitride systems.[14] To sample this relatively unexplored space, transition metal nitride compounds Zn-W-N and Zn-(W, Mo)-N are studied. Thin films are synthesized by radio-

frequency magnetron sputtering; the structural and optoelectronic properties are measured for a wide range of Zn : W and W : Mo ratios and compared to another recently discovered ternary transition metal nitride Zn-Mo-N.[15] A wurtzite phase that has been recently predicted for Zn_3WN_4 was successfully synthesized and stabilized for a wide range of Zn : W ratios and was also stabilized in the Zn-W-Mo-N system.[16] Zn_3WN_4 films were fairly resistive ($\rho = 5 \times 10^4$ Ωcm), but samples became more conductive at lower Zn concentrations ($\rho = 5 \times 10^2$ Ωcm at 50% Zn). While the Zn-W-Mo-N system was roughly the same resistivity at high Zn concentrations, below 60% Zn samples became in general more conductive ($\rho = 5$ Ωcm at 60% Zn). Optically both Zn-W-N and Zn-W-Mo-N systems are transparent at high Zn concentrations and are highly absorbing in the visible range at lower concentrations.

Finally, Chapter 4 outlines electron microscopy techniques that can be helpful for better understanding of metastable materials. Spatially resolving the composition of a material is very important in analyzing materials, particularly ones like metastable materials that may be likely to phase separate. Typical chemical analysis techniques like energy dispersive x-ray spectroscopy are discussed as well as some less-common methods like Z-contrast imaging and energy filtered transmission electron microscopy (EFTEM). Examples of experiments were these have proved useful are provided. Spatial mapping of crystalline regions by bright field TEM is discussed, and the relatively new frontier of in-situ TEM is briefly discussed along with a short example.

---

[1] J.E. Saal, S. Kirklin, M. Aykol, B. Meredig, and C. Wolverton. "Materials Design and Discovery with High-Throughput Density Functional Theory: The Open Quantum Materials Database (OQMD)." *Jom,* **2013.** 65. 1501

[2] W. Sun, S. T. Dacek, S. P. Ong, G. Hautier, A. Jain, W. D. Richards, A. C. Gamst, K. A. Persson, G. Ceder. "The Thermodynamic Scale of Inorganic Crystalline Metastability." *Sci. Adv.* **2016**. 2 (11). e1600225

[3] H. S. Chan and K. A. Dill. "Protein Folding in the Landscape Perspective: Chevron Plots and Non-Arrhenius Kinetics." *Proteins.* **1998**. 30(1). 2-33

[4]K. A. Dill. "Theory for the Folding and Stability of Globular Proteins." *Biochemistry,* **1985**. 24. 1501-09

[5] 2018 Tim Strobel. https://legacy.gl.ciw.edu/static/users/tstrobel/research.html

[6] H. Peng, P. F. Ndione, D. S. Ginley, A. Zakutayev and S. Lany. "Design of Semiconducting Tetrahedral $Mn_{1-x}Zn_xO$ Alloys and Their Application to Solar Water Splitting." *Phys. Rev. X.* **2015.** 5. 021016

[7] A. Zakutayev. "Design of Metal Nitride Semiconductors for Solar Energy Conversion." *J. Mater. Chem. A.* **2016**. 4. 6742

[8] Z. Wang, J. Wang, Y. Zang, Q. Zhang, J. Shi, T. Jiang, Y. Gong, C. Song, S. Ji, L. Wang, L. Gu, K. He, W. Duan, X. Ma, X. Chen and Q. Xue. "Molecular Beam Epitaxy-Grown SnSe in the Rock-Salt Structure: An Artificial Topological Crystalline Insulator Material." *Adv. Mater*. **2015.** 27. 4150

[9] T. Inoue, H. Hiramatsu, H. Hosono and T. Kamiya, "Nonequilibrium Rock-Salt-Type Pb-Doped SnSe with High Carrier Mobilities ≈ 300 $cm^2/(Vs)$", *Chem. Mater*. **2016.** 28. 2278

[10] J. Vidal, S. Lany, J. Francis, R. Kokenyesi and J. Tate, "Structural and Electronic Modification of Photovoltaic SnS by Alloying", *J. Appl. Phys*., **2014**. 115. 113507.

[11] A. M. Holder, S. Siol, P. F. Ndione, H. Peng, A. M. Deml, B. E. Matthews, L. T. Schelhas, M. F. Toney, R. G. Gordon, W. Tumas, D. S. Ginley, J. D. Perkins, B. P. Gorman, J. Tate, A. Zakutayev and S. Lany, "Novel Phase Diagram Behavior and Materials Design in Heterostructural Semiconductor Alloys", *Sci. Adv*. **2017.** 3. e1700270

[12] B. E. Matthews, A. M. Holder, L. T. Schelhas, S. Siol, J. W. May, M. R. Forkner, D. Vigil-Fowler, M. F. Toney, J. D. Perkins, B. P. Gorman, A. Zakutayev, S. Lany, and J. Tate. "Using Heterostructural Alloying to Tune the Structure and Properties of the Thermoelectric $Sn_{1-x}Ca_xSe$." *J. Mater. Chem. A.* **2017**. 5. 16873

[13] C.-H. Kuo, C.-S. Hwang, M.-S. Jeng, W.-S. Su, Y.-W. Chu and J.-R. Ku, "Thermoelectric Transport Properties of Bismuth Telluride Bulk Materials Fabricated by Ball Milling and Spark Plasma Sintering." *J. Alloys Compd*. **2010**. 496. 687

[14] W. Sun, C. Bartel, E. Arca, S. Bauers, B. Matthews, B. Orvananos, Bor-Rong Chen, L. Schelhas, M. F. Toney, W. Tumas, J. Tate, A. Zakutayev, S. Lany, A. Holder, G. Ceder. "A Map of the Inorganic Tenary Metal Nitrides. (submitted to Science September 2018)

[15] E. Arca, S. Lany, J. D Perkins, C. Bartel, J. Mangum, W. Sun, A. Holder, G. Ceder, B. Gorman, W. Tumas, A. Zakutayev. "Redox-Mediated Stabilization in Zinc Molybdenum Nitrides." *J. Am. Chem. Soc.* **2018.** 140 (12) 4293

[16] Y. Hinuma, T. Hatakeyama, Y. Kumagai, L. A. Burton, H. Sato, Y. Muraba, S. Iiurma, H. Hiramatsu, I. Tanaka, H. Hosono, F. Oba. "Discovery of Earth-abundant Nitride Semiconductors by Computational Screening and High-Pressure Synthesis". *Nat. Com.* **2016**. 7. 1192

Chapter 2 Commensurate Heterostructural Alloying in $Sn_{1-x}Ca_xCh$ (Ch = S, Se)

Contribution of Authors:

Aaron Holder and Stephan Lany from the National Renewable Energy Laboratory (NREL) conducted all DFT calculations for the crystal structure, formation enthalpies, phase diagrams, predicted band gaps, and predicted effective masses for the $Sn_{1-x}Ca_xCh$ alloys. They also provided the simulated XRD patterns for select alloy compositions. Sebastian Siol from the NREL synthesized all sputtered $Sn_{1-x}Ca_xS$ samples and conducted the XRD, XRF, four point probe, and optical transmission and reflection measurements on those samples. Sebastian also provided the graphs in Figure 2.9. Laura Schelhas from SLAC National Accelerator Laboratory (previously the Stanford Linear Accelerator Center) provided 2D wide angle x-ray diffraction for both $Sn_{1-x}Ca_xS$ and $Sn_{1-x}Ca_xSe$ and provided the graphs in Figures 2.12 and 2.19. Derek Vigil-Fowler from NREL provided the Bethe-Salpeter equation optical calculations for extinction coefficients and absorption coefficients for select $Sn_{1-x}Ca_xSe$ compositions for both electron-hole interacting and non-interacting cases. TEM samples for the $Mn_{1-x}Zn_xO$ and $Sn_{1-x}Ca_xS$ decomposition pathway study were made and analyzed by Brian Gorman and John Mangum from Colorado School of Mines who also gave advice in the $Sn_{1-x}Ca_xSe$ phase decomposition study. James May from Oregon State University acquired and processed all optical transmission and reflection data.

2.1 Introduction Background Information

The selection of an ideal material for photovoltaic applications is complicated as it depends heavily on the geometry of the device, however there are certainly some optoelectronic characteristics that are undoubtedly helpful. The intensity signature for the solar spectrum can be seen in Figure 2.1. From this, we see the intensity peaks around 0.75 eV but is high for the range of 0.5-1.7 eV, so ideally materials used for solar applications would have a band gap in that range. In addition to an appropriate band gap, the work by T. Kirchartz and U. Rau[1] discusses the parameters needed to make an efficient solar cell based on macroscopic, internal, and microscopic variables. For internal parameters, it is in general desirable to have a high absorption α, mobility μ, and carrier lifetime τ; however, these parameters are somewhat inter-related. Given that τ is related to the carrier density by $\tau = \frac{1}{A+BN+CN^2}$, where *N* is the carrier concentration and *A*, *B*, and *C* are the non-radiative, radiative, and Auger recombination coefficients respectively, it is not advantageous to maximize *N*, as that causes τ to go to zero.[2] Instead, *N* should be minimized to get $\tau = \frac{1}{A}$, though a reasonable number of carriers are needed for the device to work. The number carriers to maximize efficiency depends on the parameters mention above, but typically are in the range $10^{13} - 10^{17}$ cm^{-3}. Materials should also have certain band alignments, consistent with those of the other materials needed to make the devices.

SnS is a material that has been of immense interest for solar applications over the past few decades. It has an orthorhombic (OR) (Pnma) crystal structure, which is highly anisotropic and can be described as a distorted rock-salt structure. It has an indirect bandgap of 1.3 eV (direct 1.7 eV)[3,4] were there is ample solar intensity (Figure 2.1a), a mobility of about 60 cm^2/Vs and a carrier concentration on the order 10^{17} $1/cm^3$,[5] so satisfies many of the desired PV requirements. Current efficiency for single junction cells is about 26.3% for Si,[6] which is nearing the Shockley-Queisser limit (a theoretical limit dictating the efficiency of an ideal solar cell given the material's own black body radiation, recombination, spectrum losses, and impedance matching)[7] of 29.1%.[8] SnS has a Shockley-Queisser limit of about 33%, as seen in Figure 2.1b.[9] Despite all these ideal qualities, solar cells composed of SnS have only managed to reach efficiencies of just over 4%.[9] This may be partly due to the anisotropic nature of the crystal structure and concurrently anisotropy of the desirable properties. SnS tends to grow with the layers parallel to the substrate ((040) texturing),[10,11] thus oriented in such a way that the desired properties are not along the axis of the

cell pile. Growing anisotropic polycrystalline material is not desirable as that considerably decreases the mobility. One way to mitigate this discrepancy in properties is to make the crystal structure uniform.

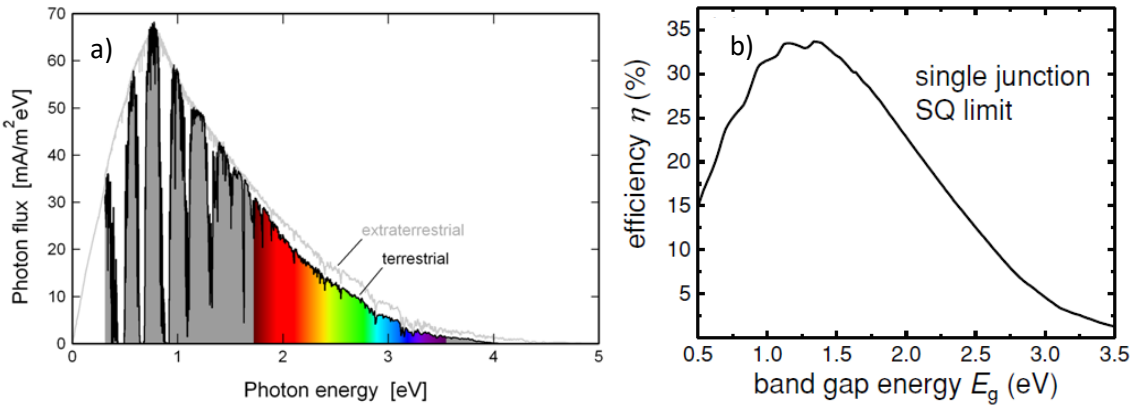

Figure 2.1. a) Terrestrial solar radiation intensity for the range of incident light waves[12] and b) the Shockley-Queisser limit for various band gaps

SnSe is also a material of interest for energy applications and has an OR crystal structure. It has a band gap of 0.9 eV and a carrier concentration of 10^{16}-10^{17} 1/cm^3, so it has also been of some interest for solar uses though has a slightly lower Shockley-Queisser limit for max efficiency and has only achieved solar cell efficiencies of ~2%[13] (6.44% as a heterojunction cell with Si).[14] It primarily has garnered intense interest as a thermoelectric material due to its high scoring thermoelectric figure of merit:

$$ZT = \frac{S^2 \sigma T}{\kappa}$$

where S is the Seebeck coefficient, σ is the electrical conductivity, T is the temperature of measurement, κ is the thermal conductivity. The combination of SnSe's extraordinarily low thermal conductivity ($0.25 < \kappa < 1.25$ W/m·K)[15,16] and fair conductivity (10^{-1}-10^{2} S/cm)[15,17] result in a high ZT score of up to ~2.5 at 900 K.[16] However, this high score is obtained only for very high crystalline films and only along one of the crystal axes. This level of high anisotropy again makes it more difficult for making highly efficient devices and could benefit from a more isotropic crystal structure.

Cubic forms of both SnS and SnSe have been explored in the past with various methods and with limited success. While rock-salt cubic (RS) is the simplest and most obvious form to pursue, it is

unstable under ambient conditions. Recently a simple cubic form of both SnS and SnSe (π-SnS and π-SnSe) have been synthesized. The unit cell for this structure is large, consisting of 64 atoms, so is not very simple. The band gaps for this structure are blue-shifted (E_g=1.66-1.74 eV for π-SnS and E_g=1.4 eV for π-SnSe) from their OR structure band gaps. π-SnS and π-SnSe exhibit p-type conductivity in the range of 10^{-6} and 10^{-3}-10^{-2} S/cm respectively, much more resistive than the OR counter parts (and not as conducive for PVs or TEs). RS SnSe also been epitaxially stabilized on a Bi_2Se_3 substrate, but it was only stable to a thickness of 20 nm. The properties of the material in this form was not explored.[18] A cubic form of SnSe was stabilized by alloying with PbSe, which is stable and cubic. However, the cubic alloy was only realized in the Pb rich alloys, becoming phase separated at about 50% Pb cation concentration.[19] Vidal *et al.* were able to stabilize cubic SnS by alloying with CaS. Though they calculated a theoretical transition to RS at 18% Ca, they did not experimentally explore the lower limit of added Ca to stabilize the cubic structure, only noting that the material was cubic for Ca concentrations above 35% of cation concentration.[20]

Since Ca^{2+} ions in octahedral coordination have a similar size (1.0 Å) to that of Sn 2+ ions (1.18 Å) in a similar coordination[21] so may alloy with Sn more easily than other ions. The approach Vidal *et al.* took (also known as heterostructural alloying)[22] of alloying CaCh (Ch = S, Se) with SnCh was used in this work. CaS and CaSe are both insulators (E_g = 5.2 eV[23] and E_g = 3.9 eV[24] respectively) with RS (Fm-3m) crystal structures, so different in structure and properties than either SnS or SnSe. In order to maintain the majority of SnCh's desirable properties, a low amount of Ca to induce the RS structure would be advantageous. Because of the difference in structures with heterostructural alloying (discussed in chapter 1), there is expected to be a larger change in the material than there would be for simple isostructural alloying. This large change is well illustrated by the system $Mn_{1-x}Zn_xO$, an alloy between wurtzite (WZ) ZnO and RS MnO. For example, RS MnO has a bandgap of ~3.4 eV, but WZ MnO has a bandgap of ~2.4 eV.[25]

For this work, the formation enthalpy is calculated using a parameterized DFT computational approach that is calibrated to highly accurate total energies computed within the random phase approximation (RPA).[26] This predicts that both $Sn_{1-x}Ca_xS$ and $Sn_{1-x}Ca_xSe$ are metastable heterostructural alloys with a composition-controlled phase change between a layered orthorhombic structure and an isotropic cubic structure at a critical composition of x = 0.18 and x = 0.13 respectively. Further, the calculated band gap at the transition composition for each is lower

than their respective SnCh end members, which means that the electrical conductivity is likely to be higher, and may increase their potential for PV and TE applications. With the formation enthalpy for $Sn_{1-x}Ca_xS$ having been previously calculated, our first key result is the calculation of the phase diagram of the metastable heterostructural alloys $Sn_{1-x}Ca_xCh$. Next is the experimental verification of the calculated structural transition by x-ray diffraction (XRD) in kinetically stabilized films and the observation of microstructures consistent with the predicted spinodal decomposition of the alloys at higher temperature. Finally, the electrical and optical properties of kinetically stabilized thin-film $Sn_{1-x}Ca_xSe$ alloys synthesized by pulsed layer deposition (PLD) are reported. We observe the predicted structure change, successfully stabilize the isotropic RS structure over most of the composition range ($x > 0.25$ for $Sn_{1-x}Ca_xS$ and $x > 0.2$ for $Sn_{1-x}Ca_xSe$) and achieve good agreement with the computed band gap trend. While $Sn_{1-x}Ca_xS$ samples become more resistive near the structural transition, in $Sn_{1-x}Ca_xSe$, a large increase in the hole concentration occurs near the structural transition with a large increase in conductivity. The resulting room temperature power factor (S^2/ρ) is strongly enhanced over that of the end-member SnSe films and is comparable to and even greater than reported values for polycrystalline SnSe.[27,28] The polycrystalline nature, isotropic crystal structure, and good thermoelectric properties suggest that $Sn_{1-x}Ca_xSe$ is an appropriate candidate for developing polycrystalline thermoelectric devices. A slight band gap decrease in $Sn_{1-x}Ca_xS$ is seen near the structural transition; however, the conductivity also significantly decreased suggesting the alloy may be better as an insulating layer.

2.2 Theory Review

2.2.1 Theory Method

All calculations were performed by theorists at the National Renewable Energy Laboratory in the Vienna Ab Initio Simulation Package. $Sn_{1-x}Ca_xS$ mixing enthalpies were originally calculated by density functional theory-generalized gradient approximation (DFT-GGA) total-energy calculations in large supercells of more than 200 atoms, yielding a transition composition of $x = 0.18$.[20] These were subsequently recalculated (along with the calculations for $Sn_{1-x}Ca_xSe$) using the projector augmented-wave method with the Perdew-Burke-Ernzerhof (PBE) generalized gradient approximation exchange-correlation functional for DFT. To obtain accurate energies, random phase approximation based on the adiabatic-connection fluctuation-dissipation theorem (RPA-ACFDT) was used. Because mixing enthalpies for commensurate alloys (like $Sn_{1-x}Ca_xS$ and

$Sn_{1-x}Ca_xSe$) must be corrected with an energy-corrected functional, we added an onsite potential of -0.5 eV acting on the Sn-*p* states to the PBE result to increase the hybridization with occupied orbitals.[22] This results in an energy difference of E_{RS}-E_{OR}= 153meV for the sulfide system and E_{RS}-E_{OR}= 57meV for the selenides. The mixing enthalpies were then then fitted by second order polynomials except the transition region for $Sn_{1-x}Ca_xS$ which was fitted with a third order polynomial. With the configurational entropy of the random alloy $\Delta S = -k_B[x \ln x + (1 - x)\ln(1 - x)]$, the phase diagrams were obtained from ΔG_m by constructing the lowest-energy common tangent across all branches, and evaluating the zero-curvature condition for the different branches separately. To correct for the systematic DFT band gap underestimation, yet preserve DFT predicted band gap trends between compositions, theoretical bandgaps for the various compositions were obtained by adding a weighting function between the DFT-predicted gaps and the more-accurate GW calculated gaps for the end members. The weighting factors are $A = E_{g,1}^{GW}/E_{g,1}^{DFT}$ and $B = E_{g,0}^{GW}/E_{g,0}^{DFT}$ for CaCh and SnCh respectively. The intermediate compositions of the alloy are then obtained by $E_{g,x}^{GW} = E_{g,x}^{DFT}(xA - B(1-x))$.[22,29]

Bandgaps and optical absorption spectra were also calculated for various compositions of $Sn_{1-x}Ca_xSe$ using GW Bethe Salpeter equation (GW-BSE) approach. A quasirandom supercell approach with a 32-atom unit cell with periodic boundary conditions was used. The DFT calculations were performed using Quantum ESPRESSO code to generate the mean-field wavefunctions and energies for the bandstructure and optical absorption calculations. The GW calculations were performed by the BerkeleyGW package. The dielectric matrix and self-energies were obtained by a 3x3x2 sampling of the supercell Brillouin zone. The Godby-Needs plasmon pole model was used to perform the needed frequency integrations, which ensures the convergence of a bandgap within 0.1-0.2 eV.[30]

2.2.2 $Sn_{1-x}Ca_xS$ Theory Results

The mixing enthalpies (ΔH_{mix}) for various compositions of $Sn_{1-x}Ca_xS$ in both RS and OR structures are shown in Figure 2.2a. From this we can see that at all compositions for both structures, apart from the end members, have positive mixing enthalpies and thus would phase separate into the thermodynamic ground states OR SnSe and RS CaSe given the thermodynamic limit. If instead thermodynamic phase separation is kinetically hindered by using a nonequilibrium, high-energy growth method such as PLD or sputtering, then the resulting metastable alloy should persist and

most likely will have the structure corresponding to the lower energy structure branch shown. We see that for compositions below the transition composition $x = 0.25$, the more stable branch is OR, with RS being more stable at higher x. We also note the black curve near the transition region in Figure 2.2a, indicating a blending of the two structures as the alloy is a commensurate and the transition should be continuous instead of abrupt as the other two curves would suggest.

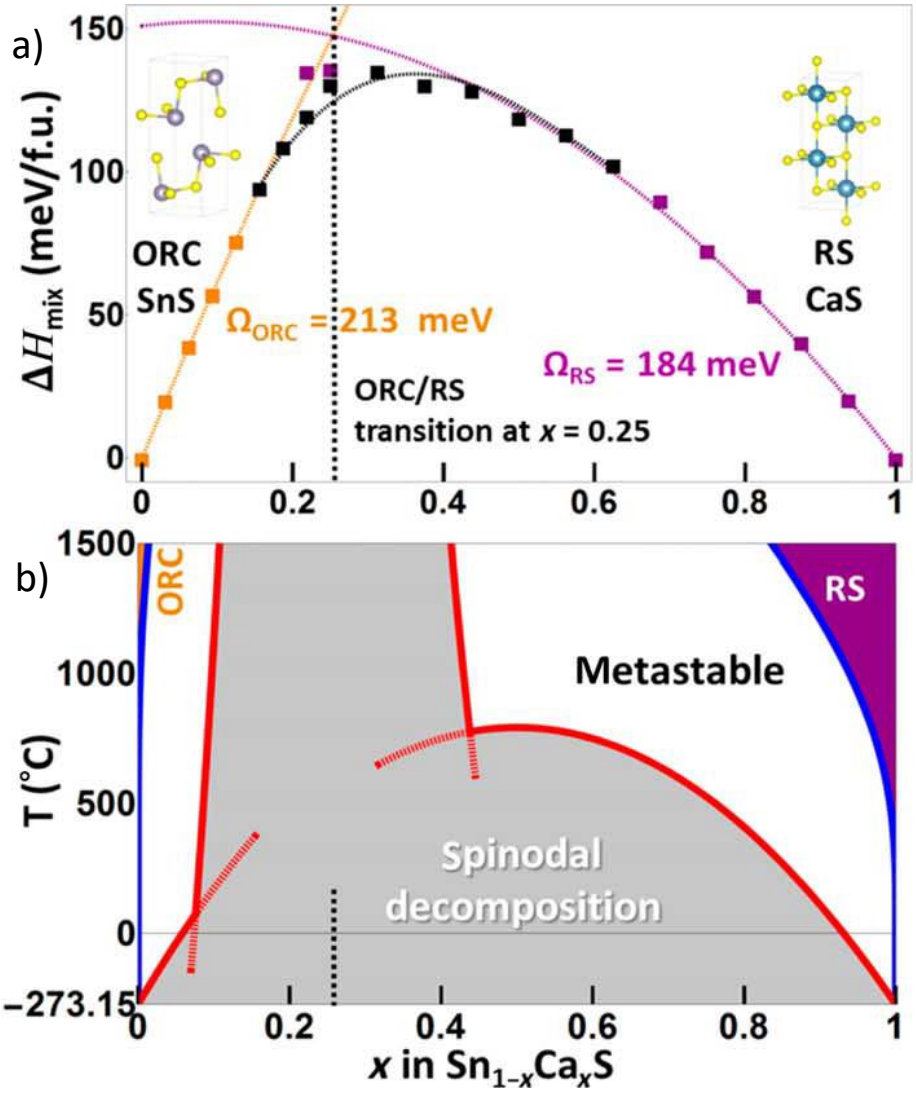

Figure 2.2. a) enthalpy of mix for select compositions of the alloy, showing the energy required at that composition for the OR structure (orange) or the RS structure (purple) to form per fundamental unit and b) the corresponding phase diagram showing the miscible, binodal, and spinodal regions.[22]

The corresponding phase diagram is displayed in Figure 2.2b. The features of this diagram are very different than typical isostructural diagrams. The region of full miscibility (purple and orange) for most of the compositions is much higher than is accessible for most lab settings, aside from

which the materials would have already be melted. The white region is indicative of the binodal or metastable region, where these compositions would be likely to binodally separate if grown by thermodynamic methods but can be kinetically stabilized. The gray regions show the spinodal region where samples grown in this region are predicted to phase separate spinodally, though still may be kinetically stabilized. The spinodal region is capped with a discontinuous spinodal curve. The disjoint in the curve occurs at the transition composition (x = 0.25), and each side of the curve is representative of the spinodal curve for the respective structures: OR for x < 0.25 and RS for x > 0.25. The taller gray region is the pseudo-spinodal region caused the sharp curvature of the black curve in the enthalpy plot due to the commensurate, continuous transition.

Figure 2.3 shows GW weighted DFT calculated band gaps and hole effective masses for select compositions. The red squares indicate the alloy in the OR structure and blue in the RS structure. In Figure 2.3a, there is a noticeable drop in the band gap at the transition point from ~1.2 eV (OR) to ~0.6 eV (RS) demonstrating the effects of the crystal structure on the band gap. A band gap of 0.6 eV is a little low for PV applications, but the gap quickly increases to a more reasonable 0.9 eV and from there increases more like the optical bowing we would expect from an isostructural alloy. In Figure 2.3b, the hole effective mass dips dramatically from 2.35-1.1. As the effective mass is inversely related to the mobility ($\mu = \frac{q\tau}{m^*}$ where q is the carrier charge, τ is the average scattering time, and m^* is the effective mass in the direction of the drift field), this indicates a nice increase in the mobility with the addition of the isotropic structure. It is interesting to see the wide variation of mobility with only small compositional changes, but we note these were taken from a variety of randomized structures, and while the trend should be solid, individual points (such as the large drop in band gap and effective mass at x = 0.8) may be a bit anomalous. These trends were used as motivation and as guidance for experimental synthesis and characterization, particularly in the optical measurements.

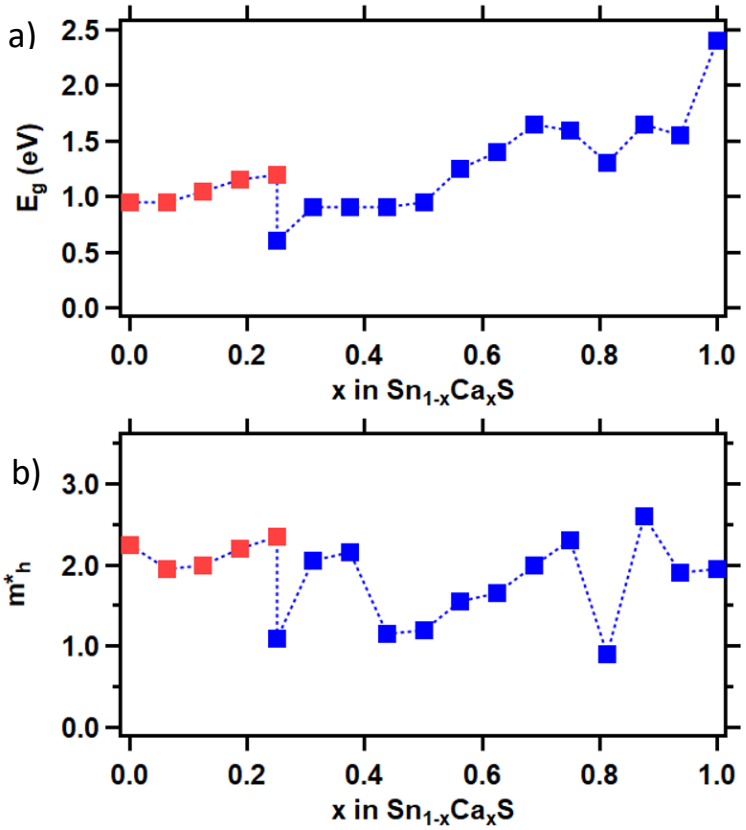

Figure 2.3. a) DFT calculated band gaps scaled by GW calculations of the end members. The effect of the structure on the band gap is quite evident at the transition composition. b) The effective hole mass calculated from DFT, the transition to a RS structure lowers the effective mass on average, leading to a predicted higher mobility for the material.

2.2.3 $Sn_{1-x}Ca_xSe$ Theory Results

Mixing enthalpies for the $Sn_{1-x}Ca_xSe$ alloy are shown in Figure 2.4a. We again see the curves for both OR (red) and RS (blue) structures which are both positive for all compositions and thus not stable in the thermodynamic limit. The predicted transition point or cross over between the two structures at $x = 0.125$ is much lower than that predicted in $Sn_{1-x}Ca_xS$. Because the transition region is so narrow, the heavy curvature of the enthalpy due to the continuous, commensurate transition was not calculated as it was not deemed useful. The overall energy required for mixing at each composition is lower than that for the $Sn_{1-x}Ca_xS$ alloy, suggesting that this alloy should be easier to stabilize. The corresponding phase diagram for the alloy is displayed in Figure 2.4b. The form

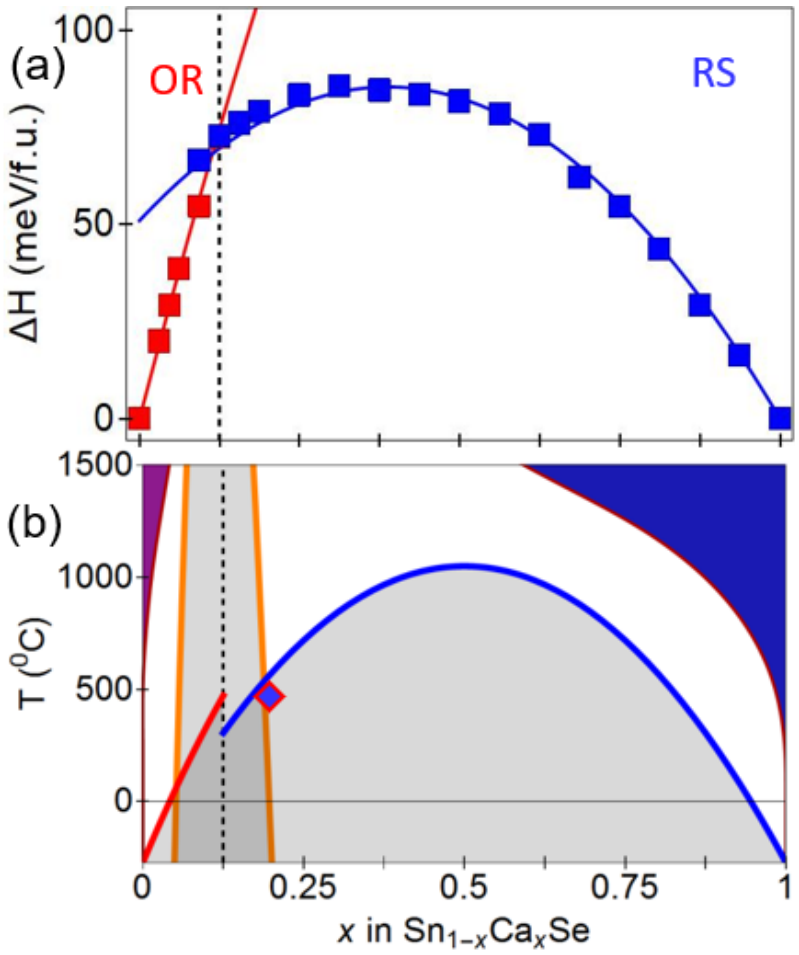

Figure 2.4. a) Enthalpy of mixing per fundamental unit for $Sn_{1-x}Ca_xSe$ in both OR (red) and RS (blue) structures. The cross-over of lowest energy structure occurs at x = 0.125. b) The resulting temperature vs. composition phase diagram for $Sn_{1-x}Ca_xSe$. The blue diamond in b) describes the growth temperature and composition of the sample analyzed by TEM in Figure 2.22.

of the diagram is similar that of $Sn_{1-x}Ca_xS$ with the large metastable space (white) and unstable spinodal region (grey). The temperatures for full miscibility is much more accessible for more compositions than for $Sn_{1-x}Ca_xS$, indicated by the increased blue (Sn incorporated into the RS CaSe structure is stable) and purple (Ca incorporated into the OR SnSe structure is stable) regions, but are still much higher than accessible for most laboratories. Accessible temperatures (~300-500^o C) bring growth of most of the alloy into the spinodal region. The spinodal region, where the sample is predicted to decompose spinodally (a decomposition in response to small composition fluctuations occurring on a large scale, rather than the nucleation and growth expected for binodal decomposition), is nearly symmetric for this alloy, though a disjoint in the curve is again seen at the transition composition. The transition region is again encompassed by the large spike in the

spinodal region, which is due to the curving of the enthalpy and free energy in the continuous transition. Because of the high temperatures required to stabilize the alloy thermodynamically, we again employ the idea of kinetic stabilization wherein the required energies are attained through high energy, non-linear growth methods like PLD. These states are frozen in by quenching, which happens very quickly in PLD,[31] then lightly perturbed through gentle heating to obtain the desired metastable state.

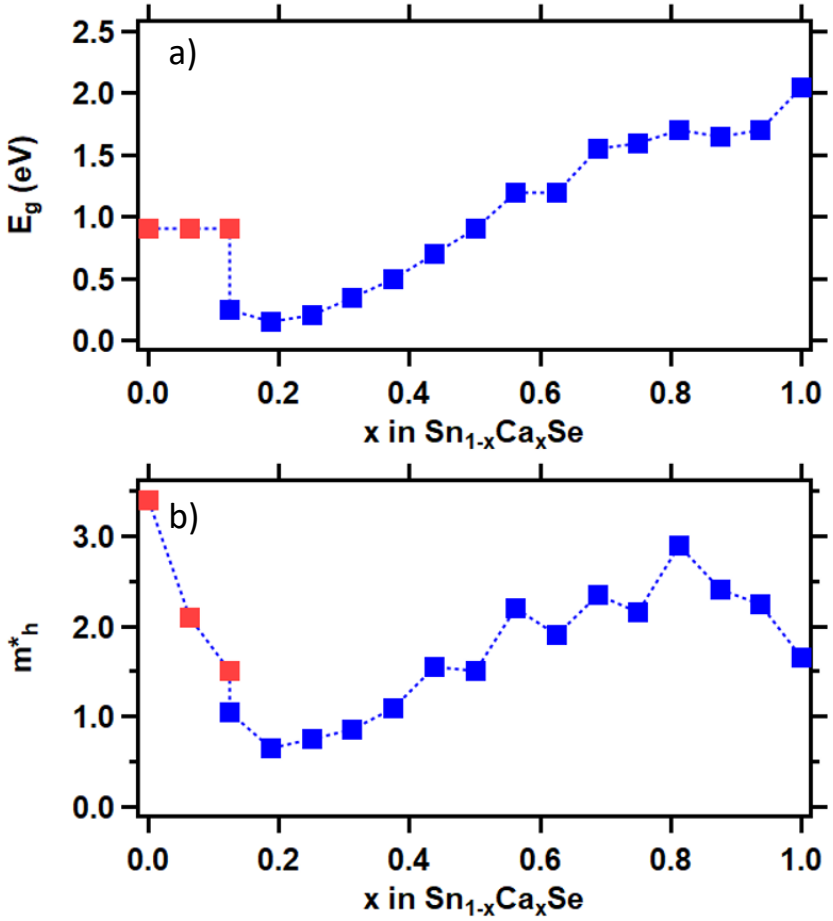

Figure 2.5. a) GW weighted DFT calculated band gaps and b) DFT calculated hole effective masses for the $Sn_{1-x}Ca_xSe$ alloy in the more stable structures.

Figure 2.5a shows the GW weighted DFT calculated band gaps for select compositions of $Sn_{1-x}Ca_xSe$. We again see a large drop in band gap at the OR to RS transition, which appears to be a hallmark of heterostructural alloys. This is not at all surprising when one thinks of the difference in band gaps between polymorphs. In this case, the drop in band gap between OR $Sn_{1-x}Ca_xSe$ to RS (from 0.9 eV to 0.25 eV) is much larger than in $Sn_{1-x}Ca_xS$. Such a large drop in band gap is

likely to cause an increase in carrier concentration and conductivity, as the carriers are more liable to be thermally excited across such a small band. Such an increase in conductivity could be quite beneficial from a device standpoint. After the transition, the band gap steadily increases as Ca is added. Figure 2.5b shows the DFT calculated hole effective masses. Surprisingly, even with the addition of a small amount of Ca, the effective mass is predicted to decrease quite dramatically, corresponding to an increase in hole mobility. Just after the OR to RS transition, the effective mass is predicted drop to about one order of magnitude below what it was at OR SnSe, which is an astounding improvement. Such an increase in mobility would be beneficial for near every type of device. The effective mass increases reasonably steadily with the addition of Ca after the transition until about $x = 0.8$, where it decreases again until $x = 1$. Interestingly, once Ca is added, the effective mass never quite reaches what it was at OR SnSe.

2.3 Experiment Method

Thin films of $Sn_{1-x}Ca_xCh$ (Ch = S, Se) are prepared by pulsed laser deposition (PLD) in ultra-high vacuum (10^{-9} Torr base pressure, 10^{-7} to 10^{-6} Torr pressure during deposition) at a target-substrate distance of 5 cm using a 248 nm KrF excimer laser (Compex 201) with energy fluence between 0.5–1 J cm^{-2} (schematic in Figure 2.6). The substrate is held at a fixed temperature $250^o\,C < T_{sub} < 500^o\,C$. Different alloy compositions corresponding to $0 \leq x \leq 1$ in $Sn_{1-x}Cax Se$ are obtained by alternating ablation between SnSe (SnS_2) and CaSe (CaS) targets, with a total of 50 (100) pulses per cycle divided between the targets according to the desired cation stoichiometry. Each cycle results in about 1–2 nm of $Sn_{1-x}Ca_xCh$ at a substrate temperature of ~300 ^oC. This layering procedure is repeated until the desired film thickness is obtained, amounting to usually about 100–200 nm. A schematic is shown in Figure 2.2 The targets, SnSe (Super Conductor Materials, Inc., purity > 99.999%), CaSe1.1 (American Elements powder purity > 99.5%; pressed in house with added Se), SnS_2 (American Elements, Purity > 99.99%), and CaS (Super Conductor Materials, Inc., purity > 99.9%) are more than 90% of theoretical density. The laser repetition rate is set to 10 Hz, and the time to switch between targets is about 1-2 s. After film deposition, the heater is immediately turned off and the films are moved to an evacuated load-lock, which is then brought to ambient pressure and temperature in the presence of nitrogen gas. The removal process takes about 15 minutes, allowing an average cooling rate of 20–30 $^oC\ min^{-1}$. Prior to deposition, SiO_2

substrates are prepared by a 15 min soak in acetone then methanol in an ultrasonic bath followed by a rinse in DI water and being blown dry in N_2.

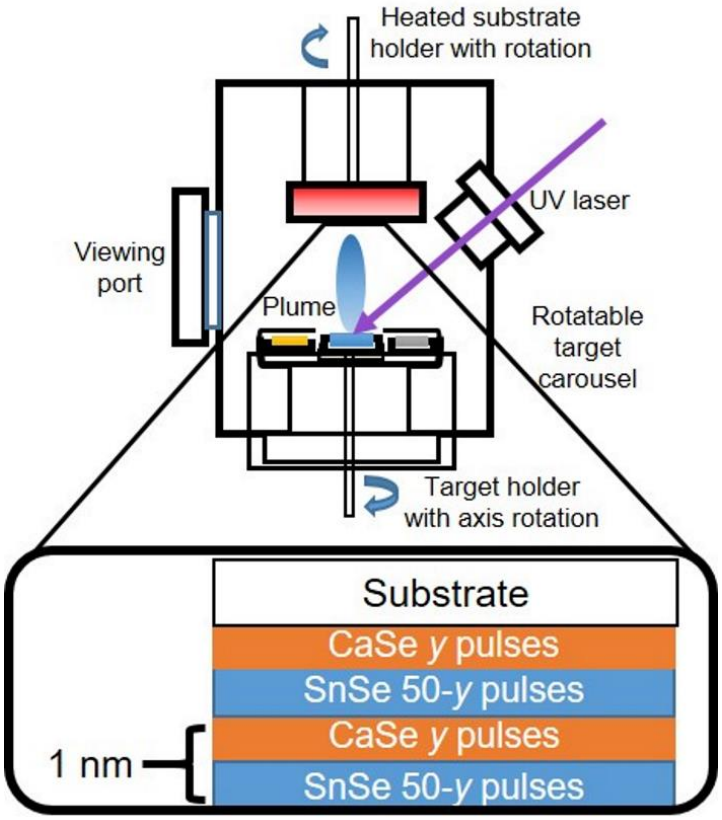

Figure 2.6. Schematic of the vacuum chamber and the deposited layer before interlayer mixing. One set of layers was about 2 nm for the $Sn_{1-x}Ca_xS$ system and about 1 nm for the $Sn_{1-x}Ca_xSe$ system.

The film stoichiometry, and in particular the Sn : Ca ratio in $Sn_{1-x}Ca_xCh$, is nominally controlled by the relative number of pulses directed at each target, though to some extent it is also influenced by the growth temperature. Representative films have been analyzed by electron probe microanalysis (EPMA) in a CAMECA SX100 system to establish a trend. The cation ratios are consistent with those expected from the relative number of pulses on the SnSe and $CaSe_{1.1}$ (SnS_2 and CaS) targets during the layered deposition, as shown in Fig 2.7, and maintains an overall 1 : 1 cation to anion ratio. For the sulfide system, previous experience had shown a tendency for sulfur deficient films. Attempting to mitigate this, a sulfur rich target (SnS_2) was used. Resulting films were still sulfur deficient, so, to achieve stoichiometric sulfur and reduce oxygen in the film, sulfur films were post-annealed at 300^o C (ramp rate 10^o/min) for 10 minutes with H_2S flow during the

ramp and temperature hold. This resulted in some over sulfurized films, evident in the appearance of SnS_2 peaks in x-ray diffraction. For the selenide system, the CaSe target was selenide enriched to $CaSe_{1.1}$. Resulting films had a 1 : 1 cation to anion ratio. It is not clear whether the added Se was necessary, but it is interesting that so much extra sulfurization was needed for the sulfides to reach stoichiometric quantities over the amount of extra selenium needed for the selenide system.

(NOTE: At one point the $CaSe_{1.1}$ target was dropped, causing it to shatter. Films resulting from attempts to use the larger chunks of the target yielded poor quality films. Analysis of the target by Raman showed peaks where there should be none (as CaSe is cubic), and XRD patterns showed additional peaks apart from the expected cubic CaSe peaks. To mitigate this problem, the target was ground into a powder and annealed at 400° C under H_2Se flow do reduce any oxygen contamination. The resulting, analyzed powder showed only clear CaSe XRD peaks, and, when measured in Raman, the previously observed Raman peaks were removed.)

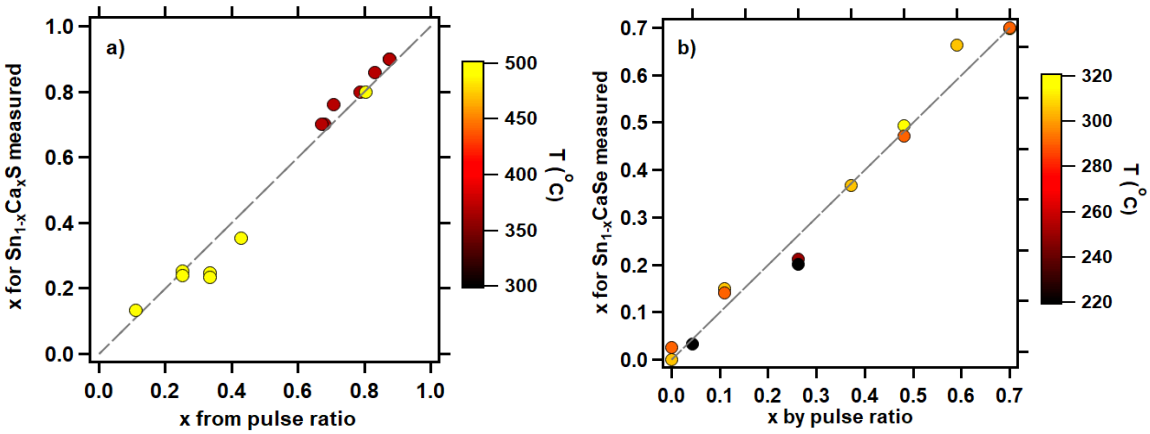

Figure 2.7. Comparison of the intended x (ratio of Ca pulses to total pulses) to x as measured by EPMA (Ca/(Ca+Sn)) for a) $Sn_{1-x}Ca_xS$ and b) $Sn_{1-x}Ca_xSe$

For this study, $Sn_{1-x}Ca_xS$ thin films were also grown by Sebastian Siol by combinatorial RF magnetron sputtering at the National Renewable Energy Laboratory (NREL). The ultra-high vacuum sputter tool used (AJA International) had a base pressure of 1.5×10^{-7} Torr. Thin film libraries were deposited on 2-inch × 2-inch fused silica substrates with a thickness of 1.5 mm. During growth, substrates were heated using a special heating stage set-up resulting in a temperature gradient across the library ranging from 400°C on the hottest side to 240°C on the coldest side. A more detailed description of this setup can be found in the study by Welch et al..[32] A compositional gradient was achieved by co-sputtering from two sputter guns on opposing sides

of the substrate in a concentric setup with a deposition angle of roughly 20° and a target-to-substrate distance of 10 cm. The two sputter guns held ceramic SnS and CaS targets (99.9% purity). Pure argon (99.99% purity) was used as process gas. The process pressure was kept at 1.5 × 10−3 Torr for the deposition and cooling of the sample to room temperature. To sample different composition ranges, the power for the CaS sputter gun was kept constant at 40W, while the SnS sputter gun power was varied from 15 W to 20 W. Depending on the position in the substrate, sputter rates between 2.5 and 1 nm/min were achieved. Deposition times of more than 8 hours were chosen to produce films with thicknesses ranging from 500 nm for the Ca-rich regions of the films to 1500 nm for the Ca-poor regions of the films. Characterization of these films was also conducted by Sebastian Siol. Composition for these films was determined by x-ray fluorescence spectroscopy in a Fischerscope XDV-SDD.[22]

Each of the PLD film's crystal structure and phase are determined by x-ray diffraction (XRD). A Rigaku Ultima IV diffractometer with Cu Ka radiation (λ = 1.541 Å) is routinely used in the grazing incidence geometry with incidence angle of 0.6° and a χ = 90°. A schematic of the grazing incidence configuration is shown in Figure 2.8. When films are strongly textured, the θ–2θ configuration is used to verify the (00l) texturing common to the orthorhombic SnS and SnSe systems.[10,11] To increase peak intensity and reduce orientation effects, 2D wide-angle XRD patterns

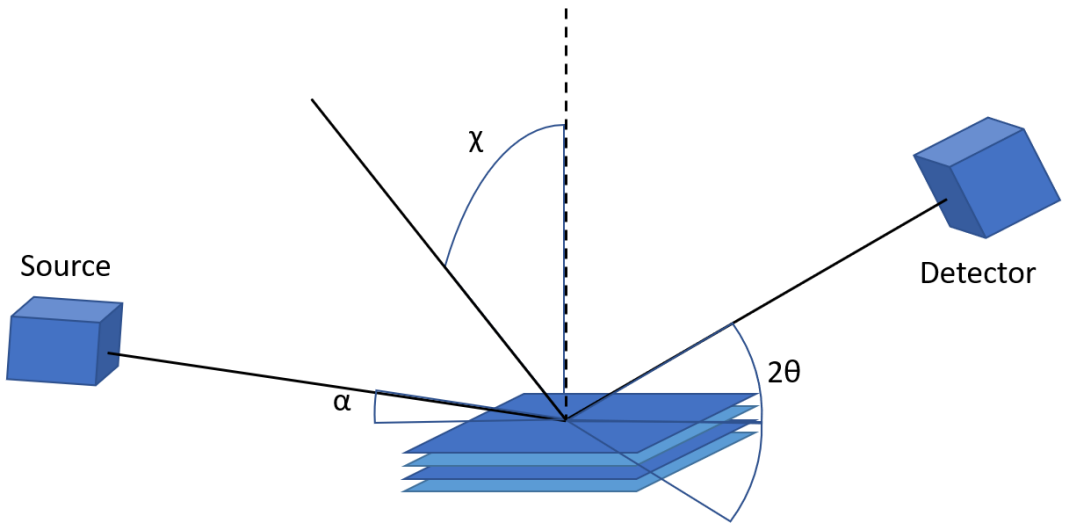

Figure 2.8. The geometry of grazing incidence x-ray diffraction. The angles are not to scale. The angles alpha and chi are held constant while the detector is swept vertically. As the detector moves, the normal for the reflecting planes changes, allowing sampling of a variety of reflecting planes.[33]

are measured on selected films at the Stanford Synchrotron Radiation Lightsource beamline 11-3 in grazing incidence geometry with an incidence angle of 2°, and λ = 0.9744 Å. Due to low availability of time on the beamline, not all samples were measured using the 2D beamline. 2D scattering data are collected with a Rayonix CCD detector, calibrated using a LaB_6 standard, and integrated between $10^o < \chi < 170^o$ using GSAS-II.37. All values of 2θ are reported in terms of Cu K_α radiation and the corresponding reciprocal lattice vector $Q = \frac{4\pi}{\lambda}\sin(\theta)$. For sputtered samples, XRD was again used to establish the structure and phase. These films were analyzed by a Bruker D8 Discover diffractometer in 2θ mode.

Optical transmission (*T*) and reflectance (*R*) for PLD samples were measured in the wavelength range 200–1800 nm in a home-built grating spectrometer. A tungsten or xenon filament lamp was used as a broadband source and made monochromatic to approximately 1 nm in the visible range by a double grating. The detector used was a Si or InGaAs (for $400 < \lambda < 1100$ nm or $900 < \lambda <$ 2600 nm respectively) broadband photodiode as appropriate. The film normal was positioned approximately 15° to the incident beam. The reflection corrected transmission $T/(1-R) \approx e^{-\alpha d}$ (ref. [34]) removed the thin-film interference fringes and yielded the product of the absorption coefficient α and the film thickness *d* at each energy. Using a Tauc analysis of the plot of $(\alpha E)^n$ vs. photon energy E, we determined the optical band gap E_g from the intercept on the energy axis. The analysis required a choice for the value of the exponent *n*, which is not known a-priori, but can be guided by band structure calculations. Usually, the gap is modeled as direct and allowed (n = 2) or indirect and allowed (n = 1/2). For sufficiently thick films, the value of *d* can be calculated from the position of interference fringes with a simple model of the wavelength dependence of the refractive index; an accurate value for *d* is necessary to calculate the absorption coefficient, but it does not strongly influence the determination of E_g. Sputtered samples' optical *T* and *R* were analyzed for wavelengths 300-1100 nm in an Ocean Optics spectrometer. *T* and *R* were used to determine the optical absorption as stated above using a thickness determined by profilometry.

For appropriate PLD films, the room-temperature Hall coefficient R_H and resistivity ρ were measured in the van der Pauw configuration[35] with field and current reversal in a LakeShore Hall measurement system. The films were deposited through a cross-shaped shadow mask to make contacts easier, and ohmic contacts were made with soldered indium. The carrier concentration $p = 1/qR_H$ was calculated from the Hall coefficient R_H and the carrier charge *q* assuming a single

band model. Room-temperature Seebeck coefficient measurements of the films were made with ohmic pressed indium contacts to measure the Seebeck voltage induced by a temperature gradient of 1–5 K between two polished copper blocks measured by a differential chromel–alumel–chromel thermocouple. The electrical resistivity for sputtered films was determined by 4 point probe using a custom built stage with a 4 point probe head.

To determine the compositional uniformity of samples on a micro-scale, cross-sectional transmission electron microscopy (TEM) specimen were prepared by focused ion beam (FIB) lift-out technique for select samples. These specimen were analyzed by energy dispersive x-ray spectroscopy (EDS) mapping using a Bruker ChemiSTEM 4 probe system (four embedded silicon drift detectors) with drift correction for increased signal and spatial accuracy in a FEI Titan (at Oregon State University) for PLD samples and an FEI Talos (at Colorado School of Mines) for the sputtered samples.

2.4 $Sn_{1-x}Ca_xS$ Experimental Results

2.4.1 Structure

In order to distinguish whether alloying was occurring, we established two key trends identified from the simulated XRD patterns shown in Figure 2.9a for the range $0 < x < 0.5$. The first was the nearing, and finally merging, of the OR-SnSe (120) and (021) peaks as Ca concentration increases. The second is the weakening and disappearance of the OR-SnSe (131) peak (and other small peaks that 2θ region). We can see from Figure 2.9a that this (131) peak is far from any RS peaks so allows for easy identification of OR structures in the alloy. Due to the large number of samples with small steps in composition, the combinatorial samples from sputtering exemplified the usefulness of these two trends. XRD patterns for $Sn_{1-x}Ca_xS$ samples grown at 220° C are shown in Figure 2.9b. We can see the (131) diminishing in height until almost disappearing at $x = 0.3$. This suggests that the transition point is nearer to $x = 0.3$ than the predicted $x = 0.25$. We also see the two peaks of (120) and (021) merging. The combination of the (120) and (021) peaks occurs much sooner than predicted, but this is likely due to the decrease in film crystallinity of samples and the resulting peak broadening causing the peaks to overlap. The decrease in crystallinity is assumed to be due to increased disorder in the films and with the addition of Ca into the lattice.

Crystalline samples above about $x = 0.3$ were not attainable by sputtering, so PLD was employed for completeness of this study, though this region of composition space had already been explored

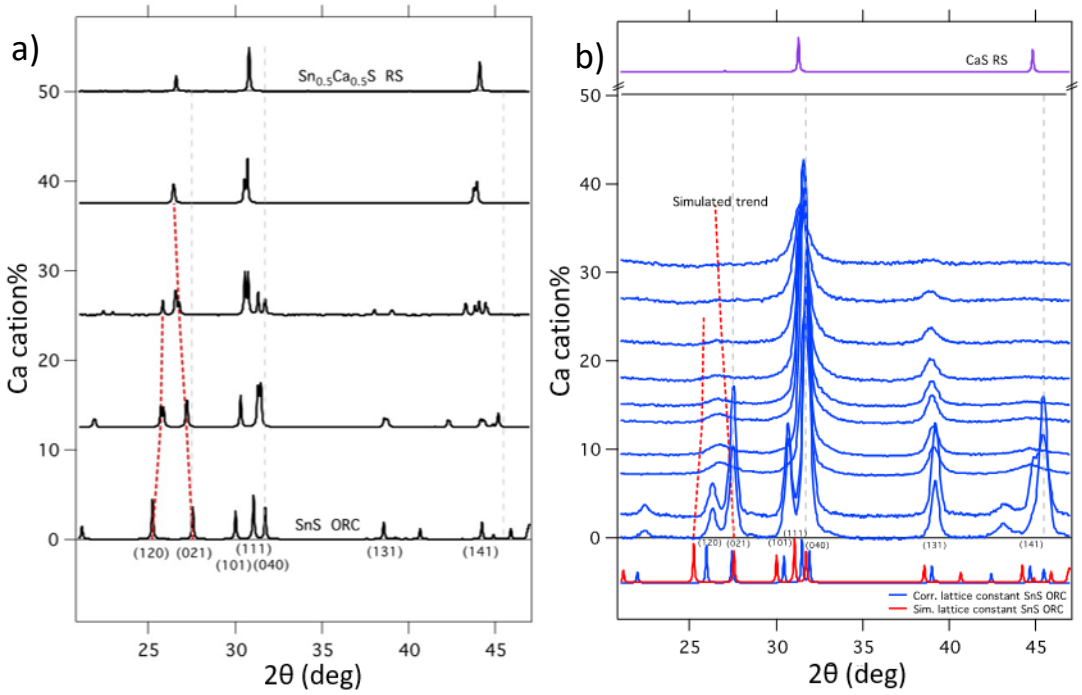

Figure 2.9. a) Simulated XRD patterns for compositions $0 < x < 0.5$ showing the trends which aided in determining whether samples were alloyed. b) XRD patterns for sputtered samples grown at 220° C illustrating how alloyed samples can be shown to follow the established trends. These patterns are plotted with 2θ resulting from Cu K_α radiation. Credit Sebastian Siol.

to some extent by Vidal et al. A few samples at the lower compositions were also synthesized for comparison to the sputtered samples. Figure 2.10a shows simulated XRD patterns for the full range of compositions color coded to correspond to the closest composition of the experimental data in Figure 2.10b. Most OR PLD samples were slightly (040) oriented, making that the main reflection observed. From the simulated data, we see the main peak shift towards lower 2θ at the transition from OR to RS then gradually shift again towards higher 2θ. We see a similar trend in the experimental data although the shift is small. Determining the phase of compositions in the range $0.3 < x < 0.6$ was difficult as most of these had low crystallinity or were highly oriented. So, we determined the phases of these difficult samples by noting the position of the main peak, since in the oriented OR structure, the main peak is (040) at $2\theta = 31.8°$ and the RS main peak is (200) is at $2\theta = 31.2°$. A peak shift of $\Delta 2\theta \approx 0.6°$ is easily discernable between different peaks. The fact that we did not see

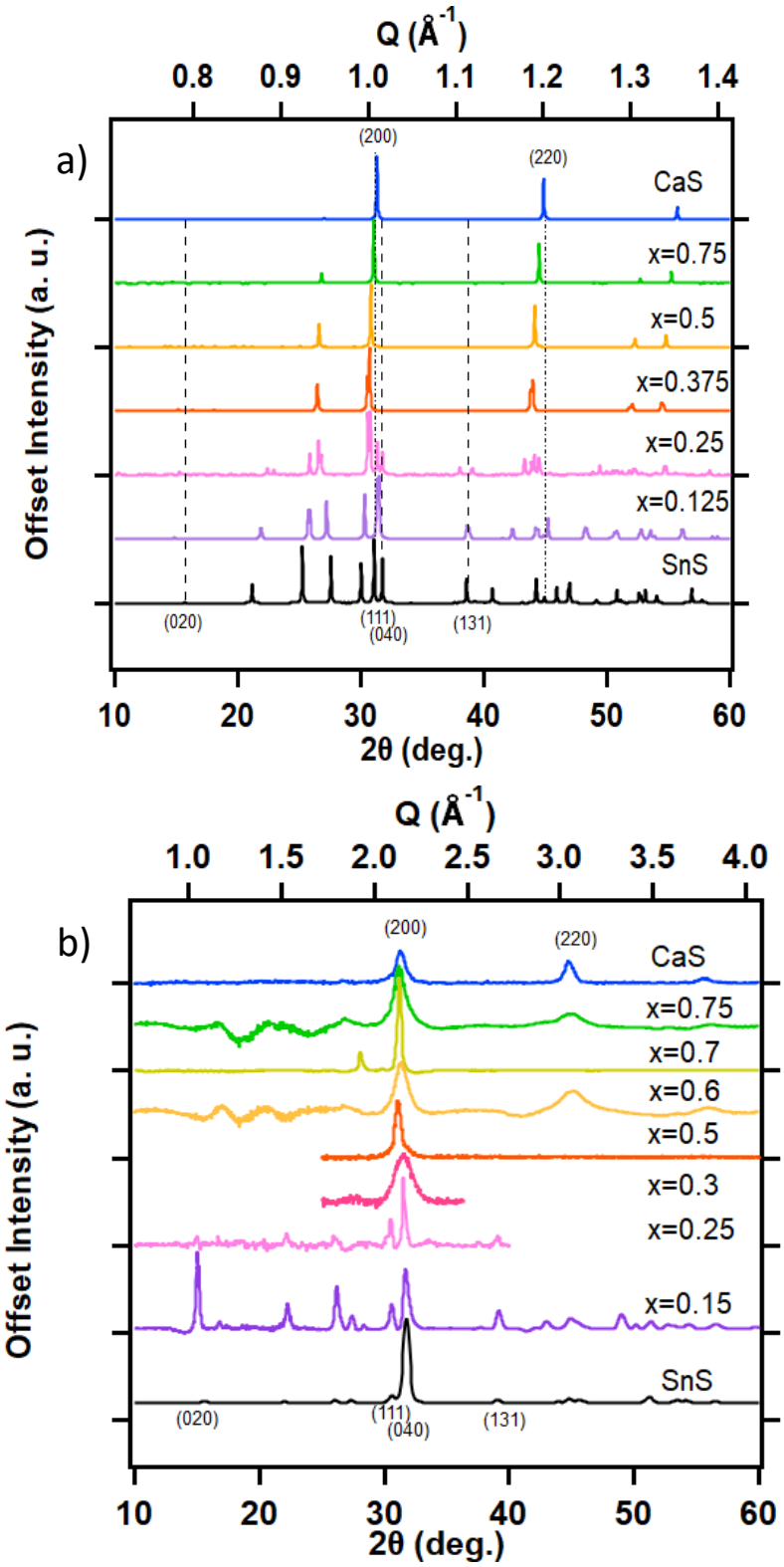

Figure 2.10. a) Simulated XRD for select samples across the entire range of the alloy. b) XRD of select PLD synthesized samples. The colors of XRD patterns for simulated data are chosen to match to the closest corresponding composition of experimental data.

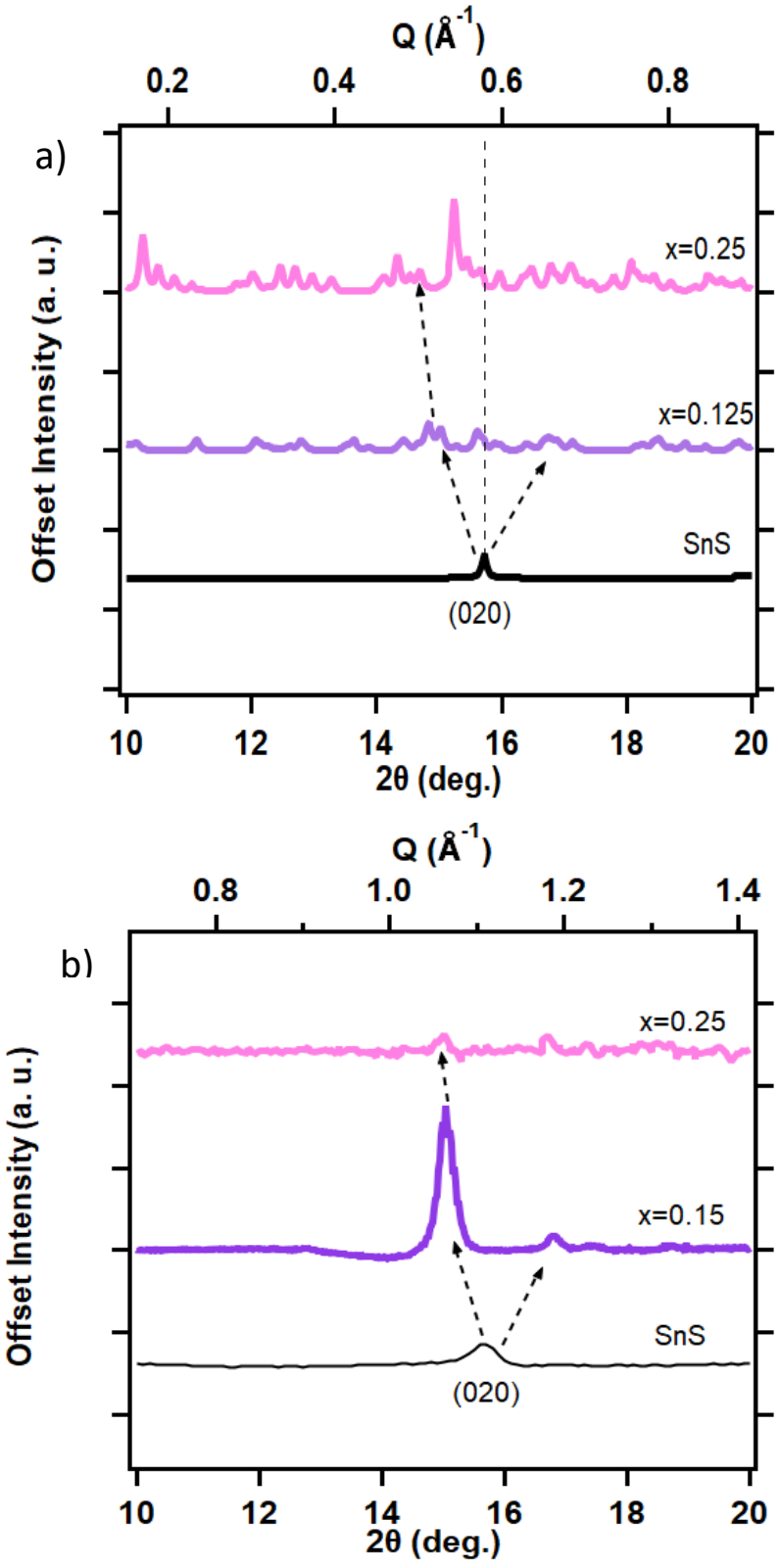

Figure 2.11. a) Simulated XRD for x < 0.25 showing the trend of the OR (020) peak and b) experimental data of the (020) peak.

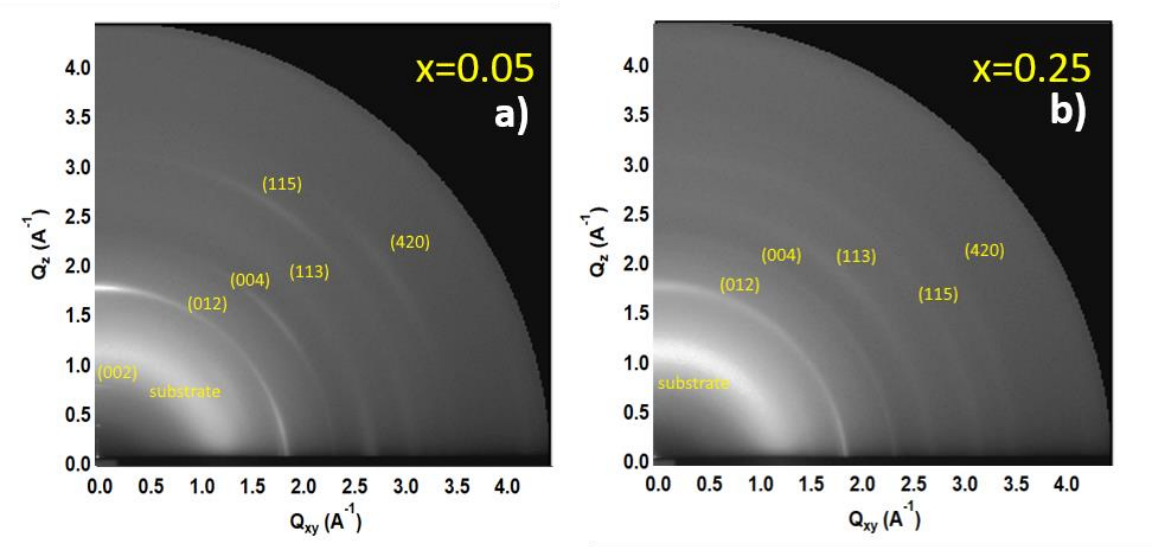

Figure 2.12. 2D wide angle XRD showing increased texturing for low Ca samples (a) x = 0.05) and more polycrystalline samples at higher Ca (b) x = 0.25)

any evidence of the OR (131) peak in samples within this composition range gave confidence to the determination of single-phase films.

For samples with lower Ca concentrations ($x < 0.3$), we see a similar trend to the one observed in the sputtering samples, the OR (120) and (021) peaks shift towards each other and merge before the transition to RS. We also see the weakening of the (131) peak, along with a general decrease in crystallinity, with added Ca. Another interesting peak trend is that of the OR (020) peak. Figure 2.11 illustrates the simulated (2.11a) and experimental (2.11b) XRD 2θ positions of the OR (020) peak at select compositions. The simulated pattern starts to look like a mess of peaks at $x = 0.25$, but there are some more intense groupings of peaks that might appear as a single peak. In the experimental data, there is a similar splitting and shifting of the (020) peak into different peaks, some at higher 2θ and some at lower than the SnS (020).

Figure 2.12 shows 2D wide angle XRD illustrating the effects of Ca on the crystallinity of the films. Films at lower Ca are more textured, as evidenced by the more concentrated spotting or streaking of the peaks (Figure 2.12a). At higher Ca concentrations, films become more polycrystalline, shown by the more complete arcs in Figure 2.12b. The decrease and slight broadening of peak intensity shows a slight decrease of crystallinity. The increase in polycrystallinity can be quite beneficial from a device standpoint, as it makes for a more isotropic film and usually provides much easier processing.

2.4.2 Substrate Temperature Effects

Most of the PLD samples for $x < 0.5$ that alloyed were grown at 460-500° C. Growth temperatures above this caused samples to phase separate into OR SnS and RS CaSe, as clearly indicated by the appearance of the (131) peak for samples with $0.3 < x$. At lower Ca concentrations, phase separation was determined by the absence of the peak shifts described above. At temperatures lower than 460° C, samples were amorphous. As the amorphous state acts as a kind of upper limit for metastability, these samples required the stronger perturbation of the higher temperature to settle to the lower energy crystalline state. For compositions $0.5 < x$, the temperature for accessing this phase was lowered to 220-360° C. Again, above this temperature range, samples phase separated, as indicated by the appearance of the OR (131) peak, and some were amorphous below the temperature range.

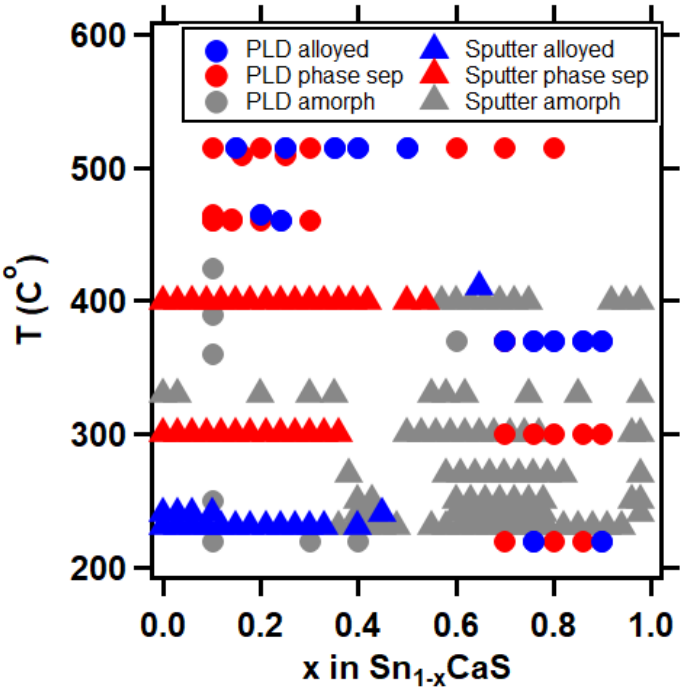

Figure 2.13. Experimental phase diagram showing the temperature regions of stability for the alloy at various compositions for both sputter and PLD samples.

From the collective sputtering and PLD samples, the experimental phase diagram in Figure 2.13 was constructed. Triangle data points indicate the sputtering samples grown at NREL. Circular data points are for samples synthesized by PLD. The blue points indicated alloyed samples, red denotes phase separated samples, and grey shows amorphous samples. This diagram suggests the stability temperature ranges are extensively different between sputtering and PLD. However, this diagram does not account for the differences in quench rate for the different types of heater (the sputtering samples were heated by a resistive heater which cools considerably slower than an IR radiative heater which was used for the PLD samples.) The diagram also neglects the different sputtering powers and laser fluences used to obtain the different samples. The diagram does, however, show a nice temperature/composition range of stability by growth method. It is interesting that the stability temperature decreases at the higher Ca concentrations, but this trend does seem to correspond to the decrease in enthalpy of mixing seen in Figure 2.2a and the decrease in temperature of the lower bound of the miscibility region in Figure 2.2b. From the exceptional agreement between theory and experiment in the XRD patterns, perhaps it should be expected that the samples would also demonstrate agreement with the trends in the predicted phase diagram.

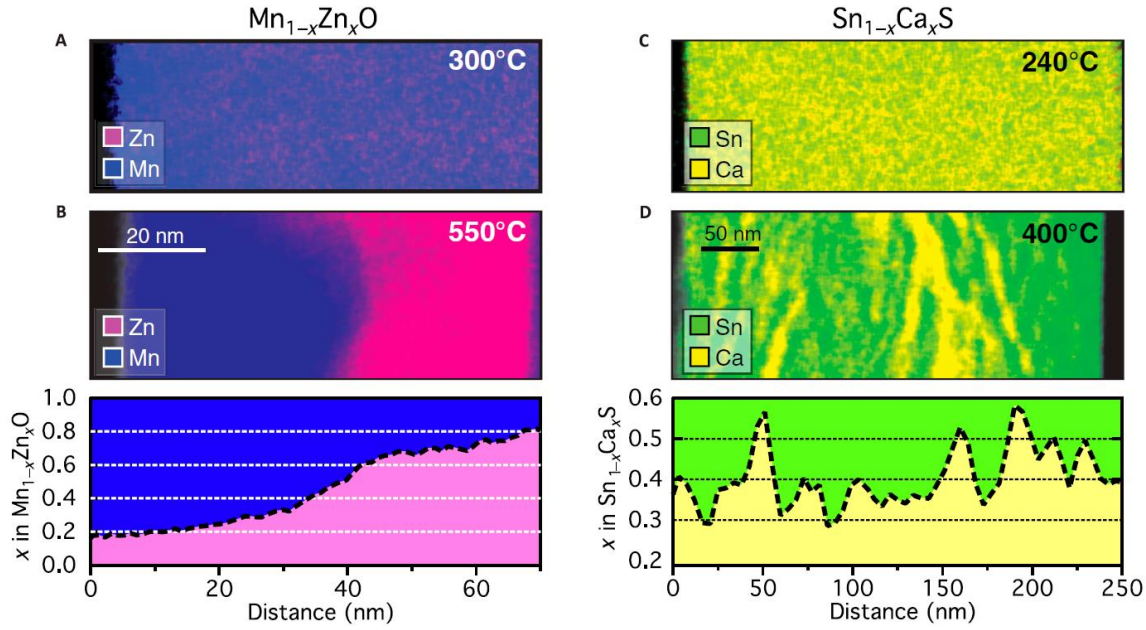

Figure 2.14. EDS for cross-sectional TEM specimen grown at a) 300º C and 550º C for the incommensurate heterostructural alloy $Mn_{1-x}Zn_xO$ and c) 240º C and d) 400º C for commensurate alloy $Sn_{1-x}Ca_xS$. a) and c) show uniform samples while b) and d) show binodally and spinodally separated samples with the results of EDS line scans showing quantitatively the Mn to Zn and Sn to Ca variation in the respective samples.[22]

To confirm the predicted decomposition pathways, cross-sectional TEM specimen were prepared by FIB lift-out and analyzed by STEM EDS. Figure 2.14a and b shows the results for an incommensurate heterostructural alloy $Mn_{1-x}Zn_xO$ (prepared also by PLD), which was predicted to binodally decompose.[22] Figure 2.14a shows the sample is uniform at lower temperatures (300^o C) where it is kinetically stabilized. Figure 2.14b shows that at higher growth temperatures (550^o C), the sample separates into large regions of Zn-rich and Mn-rich material confirming the predicted binodal decomposition pathway. Figure 2.14c and d show the EDS maps for the commensurate alloy $Sn_{1-x}Ca_xS$, which is predicted to spinodally decompose. Again, at the lower growth temperature (240^o C), the material is kinetically stabilized and appears uniform in the EDS map. At a higher growth temperature (400^o C), the sample separates into smaller regions resembling a wave. The EDS line scan shows there is, indeed, a wave-like quality to the compositional variation, validating the prediction of a spinodal decomposition pathway for this material at the temperatures grown.

2.4.3 Optoelectronic Properties

Optical Transmission and Reflectance of both sputter and PLD $Sn_{1-x}Ca_xS$ samples were measured and used to calculate the optical absorption. The optical absorption for sputtered alloyed samples is shown as a heat map for select compositions in Figure 2.15a. The onset of absorption for each sample is roughly at $\alpha = 4 \times 10^4 \text{cm}^{-1}$. This onset roughly translates to the band gap. Recalling Figure 2.3a, there is a slight dip in the band gap at the transition from OR to RS. We observe a similar trend in the absorption in Figure 2.15a near the transition composition. We note that samples grown at higher temperatures and which have phase separated do not demonstrate this dip but instead increase nearly linearly. Figure 2.15b displays band gaps for PLD samples calculated by the Tauc method overlaid onto the calculated bandgaps previously seen for easier comparison. The direct band gaps seem to track the projected trend fairly well, even exhibiting a slight dip in the band gap after the transition. However, the indirect band gap is nearly flat at ~1.5 eV for the entire range of compositions. 1.5 eV is between the direct and indirect band gap of SnS, suggesting that, even for samples that are phase pure by XRD, there may be some amorphous SnS in the sample affecting the properties.

Resistivity measurements taken by four-point probe for sputtered samples grown at various temperatures are shown in Figure 2.16. One PLD sample taken in the Van der Pauw configuration

is also shown. While there seems to be little consistency of resistivity between each composition, even between alloyed samples (230-250^{o} C), there is a general trend between growth temperatures of higher resistivity as Ca is added and a slight leveling off at x = 0.1. The difference between

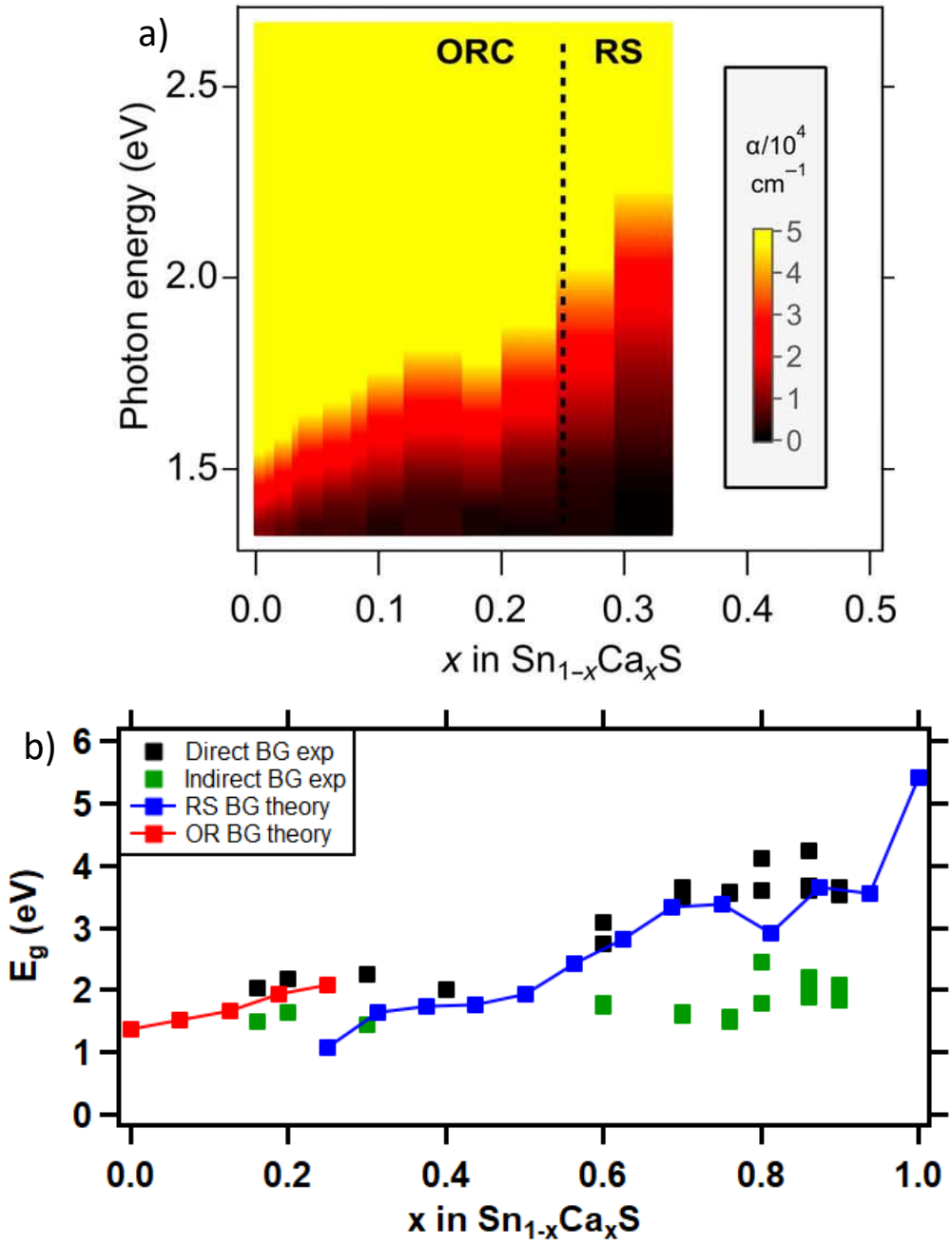

Figure 2.15. a) Optical absorption for select sputtered samples showing the onset of absorption which roughly translates to the optical band gap. b) Optical direct and indirect band gaps for select PLD samples grown at various temperatures and compared to the theoretically calculated band gaps

samples of the same composition but differing growth temperatures may be due to changes in grain size, grain boundaries, and different defects brought about by various growth temperatures. PLD samples showed similar irregularities between samples and even between measurements. The variation between samples with the same growth temperature may be due to small differences in the quality of sample, or possibly from amorphous material embedded in the sample. Since resistivity measurements assume uniformity of the sample, any variation in the sample, such as different amounts of amorphous material, could greatly change the measured results. The one PLD sample shown in Figure 2.16 gave consistent measurement results that were similar to the sputtered alloyed samples shown. It should be noted that samples became much more resistive, even with small amounts of Ca incorporated ($x \sim 0.05$) and consistent readings could not be obtained on samples above $x = 0.1$ (shown in the Figure 2.16).

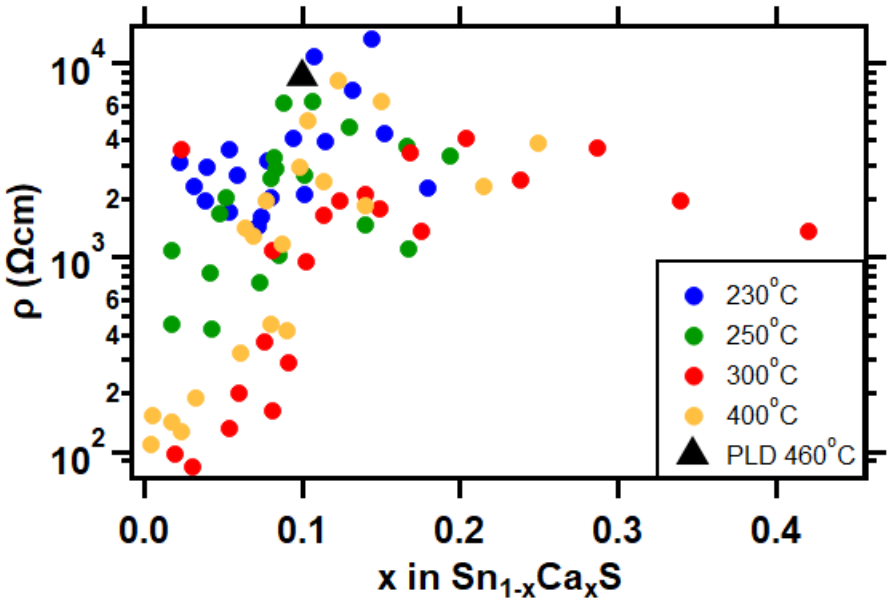

Figure 2.2. Resistivity of sputtered samples grown at various temperatures. One PLD sample is shown for comparison.

2.5 $Sn_{1-x}Ca_xSe$ Experimental Results

2.5.1 Structure

We used XRD to determine each film's crystal structure and whether it was single phase alloys or phase-separated. In general, films deposited at intermediate temperatures, 290-370° C, formed single-phase alloys and phase separate when deposited above about 450° C. When deposited at

low temperatures, below ~250° C, films' XRD patterns exhibit broad peaks characteristic of nanocrystalline or amorphous material, making it difficult to determine whether or not the films are solid solutions and whether PLD-deposited layers are properly intermixing at this low substrate temperature.

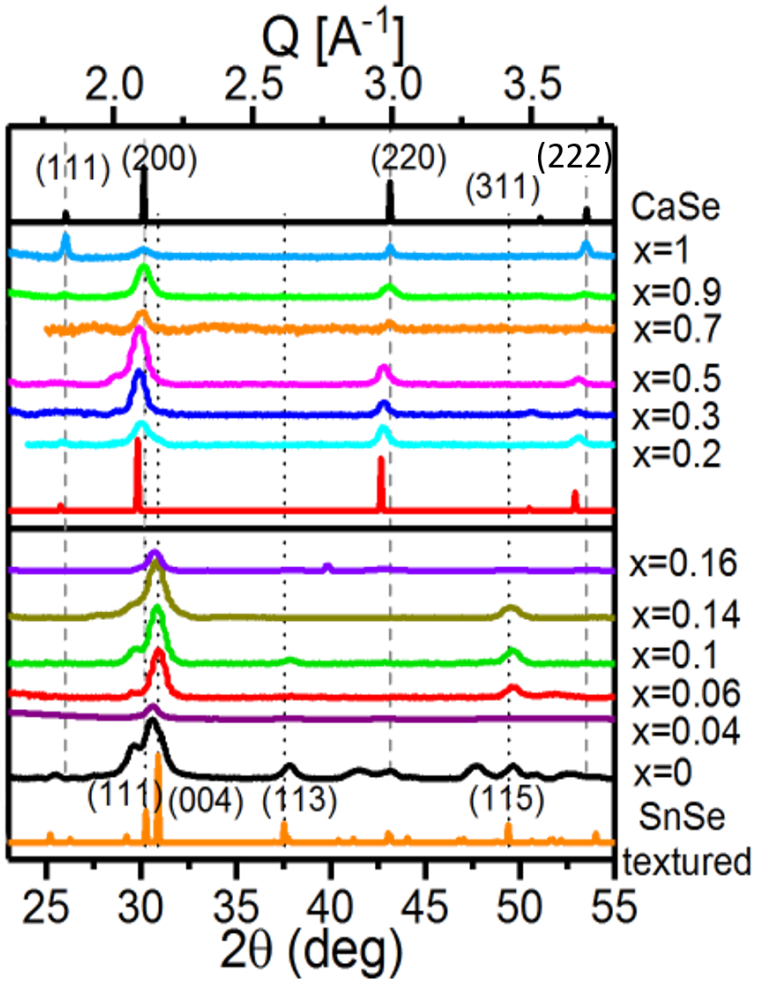

Figure 2.17. XRD patterns for the $Sn_{1-x}Ca_xSe$ in a) the RS structure for $0.2 < x < 1$ with simulated patterns for RS SnSe (red) and RS CaSe (black) and b) the OR structure of $0 < x < 0.16$ with simulated OR SnSe with 40% (00l) texturing (orange).

Figure 2.17 illustrates the change of structure from OR to RS in a single-phase alloys via background-subtracted, grazing incidence XRD patterns of a series of $Sn_{1-x}Ca_xSe$ alloys grown at $T_{sub} \approx 300^o$ C. Figure 2.17a shows the patterns for films with compositions $0.2 < x < 1$ and the simulated patterns for RS SnSe (ICDD 01-075-6132) and RS CaSe (ICDD 00-018-0304) for reference. All observed reflections in the samples in Figure 2.17a can be indexed to the RS phase.

From our experience growing OR samples by PLD, any OR phase would present reflections near $2\theta = 49.7^o$ (151), $2\theta = 37.9^o$ (131), and $2\theta = 64.2^o$ (080) which are absent in these patterns. Figure 2.17b has the patterns for films with compositions $0 < x < 0.16$ and the simulated OR (Pnma) SnSe pattern (ICDD 00-014-0159). As PLD OR samples tend to be highly textured, we added 40% (00l) texturing to the simulated reference. All reflection angles observed in Figure 2.17b are consistent with the OR structure, and the relative intensities of the reflections are consistent if the (00l) texture is assumed. We note that the film texture depends strongly on the film deposition temperature as shown by Figure 2.18 for a series of OR SnSe samples grown at different temperatures. The samples

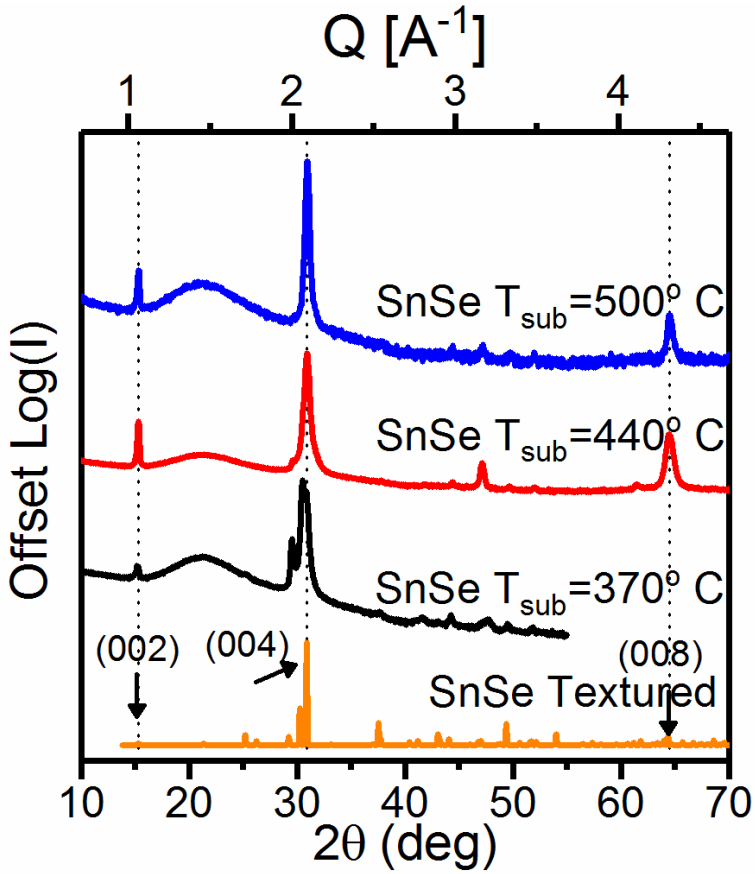

Figure 2.18. OR SnSe samples grown at different temperatures compared to a simulated OR SnSe pattern with 40% (00l) added texturing. The (00l) texturing for PLD samples tends to increase with temperature.

grown at higher temperatures tend to be more textured, as seen by the amplification of the (020), (040), and (080) reflections with respect to other peaks. We also note, while the OR samples are

prone to texturing, RS samples were highly polycrystalline. This difference is illustrated in Figure 2.19. 2D wide angle x-ray diffraction (WAX) of an OR sample taken at the Stanford Linear Accelerator National Laboratory is shown in Figure 2.19a. Qualitatively, 2θ is read radially and χ is the polar angle (refer to Figure 2.4 for the geometrical description of χ). The bright intense spots indicate high texturing in the sample. Figure 2.19b shows 2D WAX for a cubic sample demonstrating wide arcs across all χ. This indicates the sample is fully polycrystalline, which, for many applications, is beneficial from a device standpoint.

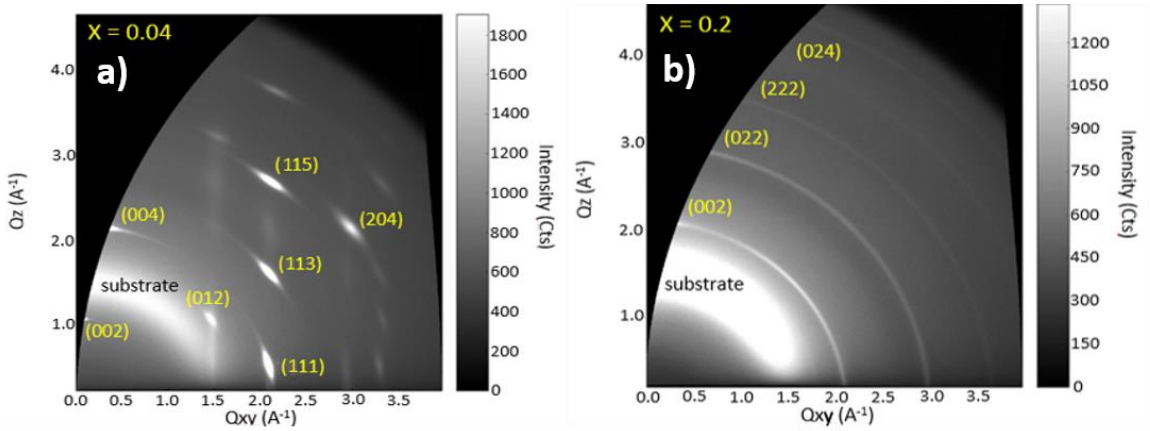

Figure 2.19. 2D WAX patterns for $Sn_{1-x}Ca_xSe$ samples grown at 300° C. a) An OR sample with x = 0.04 has high texturing as indicated by the intense bright spots. b) A RS sample with x = 0.2 exemplifying high polycrystallinity as shown by the full arcs.

For all the samples displayed in Figure 2.17, there is no evidence in XRD of the impurity phases most likely to occur. In particular we rule out $SnSe_2$ as an impurity phase because the (0001) peak at 2θ = 14.4° is quite distinct from the OR SnSe (020) at 2θ = 15.3°, and the prominent (10-12) peak of $SnSe_2$ near 2θ = 40° is absent. Moreover, as previously mentioned, the stoichiometry is consistent with a 1 : 1 (Sn + Ca) : Se ratio so is less likely to form Se-rich phases. We note that though the transition composition is predicted to be at x = 0.125 from the mixing enthalpy and phase diagram, the OR structure is observed to persist through x = 0.16. The RS structure is observed to occur at x = 0.2, from which we conclude the transition occurs at about x = 0.18. This is consistent with the experimental transition composition for $Sn_{1-x}Cax$S ($x \approx 0.3$) being slightly higher than the predicted transition composition (x = 0.25).The alloy lattice parameters changed with the addition of Ca as expected from simulation as shown in Figure 2.20 with the comparison of certain RS (Figure 2.20a) and OR XRD peaks (Figure 2.20b) at different compositions to the

corresponding simulated XRD peak (black open marks in Figure 2.20) of the same or similar composition. RS peaks of (200), (220), and (222) were chosen to represent these trends as these three peaks appeared in all RS XRD patterns and were easily tracked. The OR pattern is much

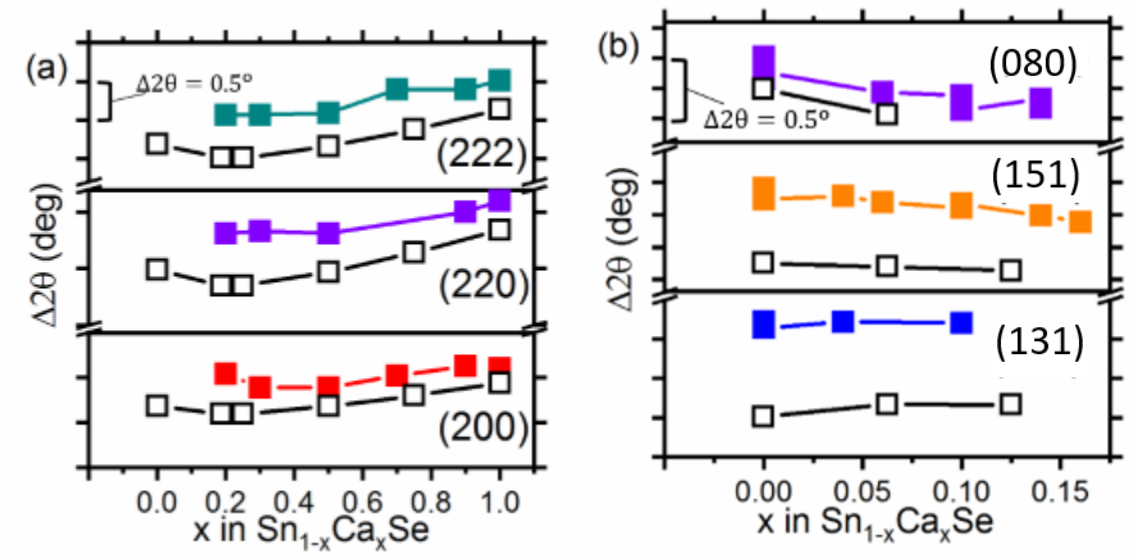

Figure 2.20. 2θ peak positions tracking peak shift trends for select peaks in a) the RS structured samples and b) the OR structured samples compared to the same peak position in simulated XRD patterns.

more complicated, so the (131), (151) and (080) peaks were chosen to track this trend as they were more isolated than other peaks and quite distinct from any RS peaks. While absolute XRD peak positions for samples were a bit higher than predicted by simulation, the trend of peak shifts matched quite well for most compositions but seemed generally to fit better for samples in the RS structure than for the OR structure.

Combining the phase information determined from XRD, the experimental phase diagram in Figure 2.21 was constructed. It is interesting that there is very few samples, compared to the $Sn_{1-x}Ca_xS$ phase diagram, that were deposited amorphous. Even films with low growth temperatures exhibited low crystallinity, though it seemed clear that samples were not demonstrating inter-layer mixing. Low temperatures samples had XRD peaks consistent with RS CaSe, suggesting that the SnSe layers remained amorphous. The phase diagram shows the temperature window of stabilization for this alloy is very narrow. Again this phase diagram does not take into account

other growth factors which were very important in addition to the growth temperature, most important of which seemed to be base pressure.

Since the calculated phase diagram predicted phase separation of samples (ignoring kinetic stabilization) as well as different phase decomposition pathways depending on the growth conditions (binodal or spinodal), we were interested also in the phase separated samples. When a $Sn_{1-x}Ca_xSe$ sample decomposes binodally, it separates into large regions of stable compositions, in this case the two end members. If instead the sample spinodally decomposes, it should separate into Sn-rich and Ca-rich regions within the same type of structure into smaller, fluctuating regions characterized by the spinodal 'wavelength'. Figure 2.22 shows XRD patterns for a series of samples grown at 500^o C, which is above the temperature of kinetic stabilization for this alloy. We see in this sample that even with just a small amount of Ca added (x = 0.06), the RS (222) peak near 2θ = 54^o appears. While there is an SnSe peak at a similar 2θ, it is clear the peak in question

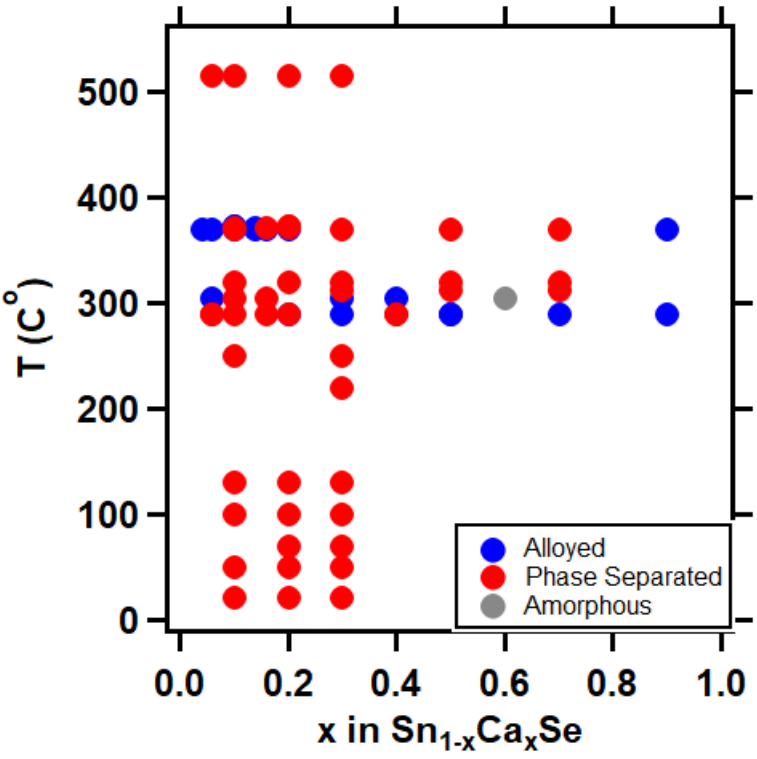

Figure 2.21. Experimental temperature vs. composition phase diagram showing the very narrow window of stable growth.

it is a RS peak from the increase in intensity with added Ca (along with the appearance of other RS peaks). That two phases appear with XRD peaks consistent with the two end members indicates that binodal decomposition is occurring, as we might expect for most of those compositions given the phase diagram.

To explore spinodal decomposition, we took samples that had been grown in the spinodal region to examine the phase and the spatial composition on a nanoscale. Figure 2.23a shows Z-contrasted, dark field scanning transmission electron microscope (STEM) images of two cross-sectional TEM specimen prepared by FIB lift-out from films with composition x = 0.2. The images were taken at low camera lengths (75mm) to reduce diffraction contrast and increase elemental contrast (higher element containing regions appear brighter). The sample on the left was grown at

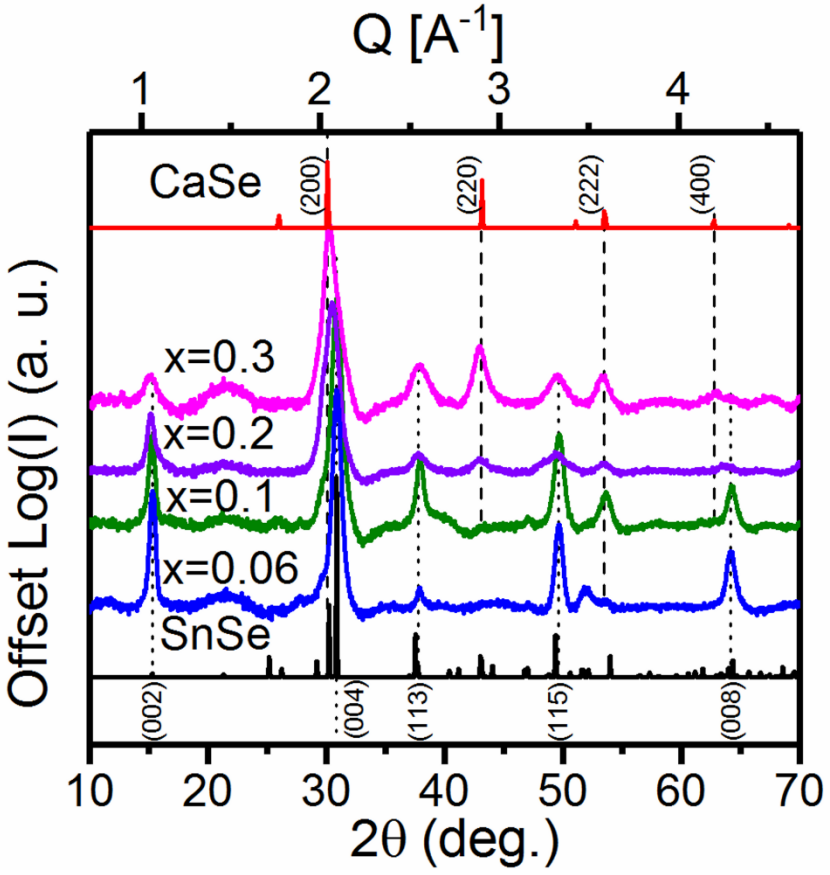

Figure 2.22. Samples of select composition around the transition region grown at 500° C showing phase separation as indicated by the persistence of OR peaks and subsequence appearance of RS peaks.

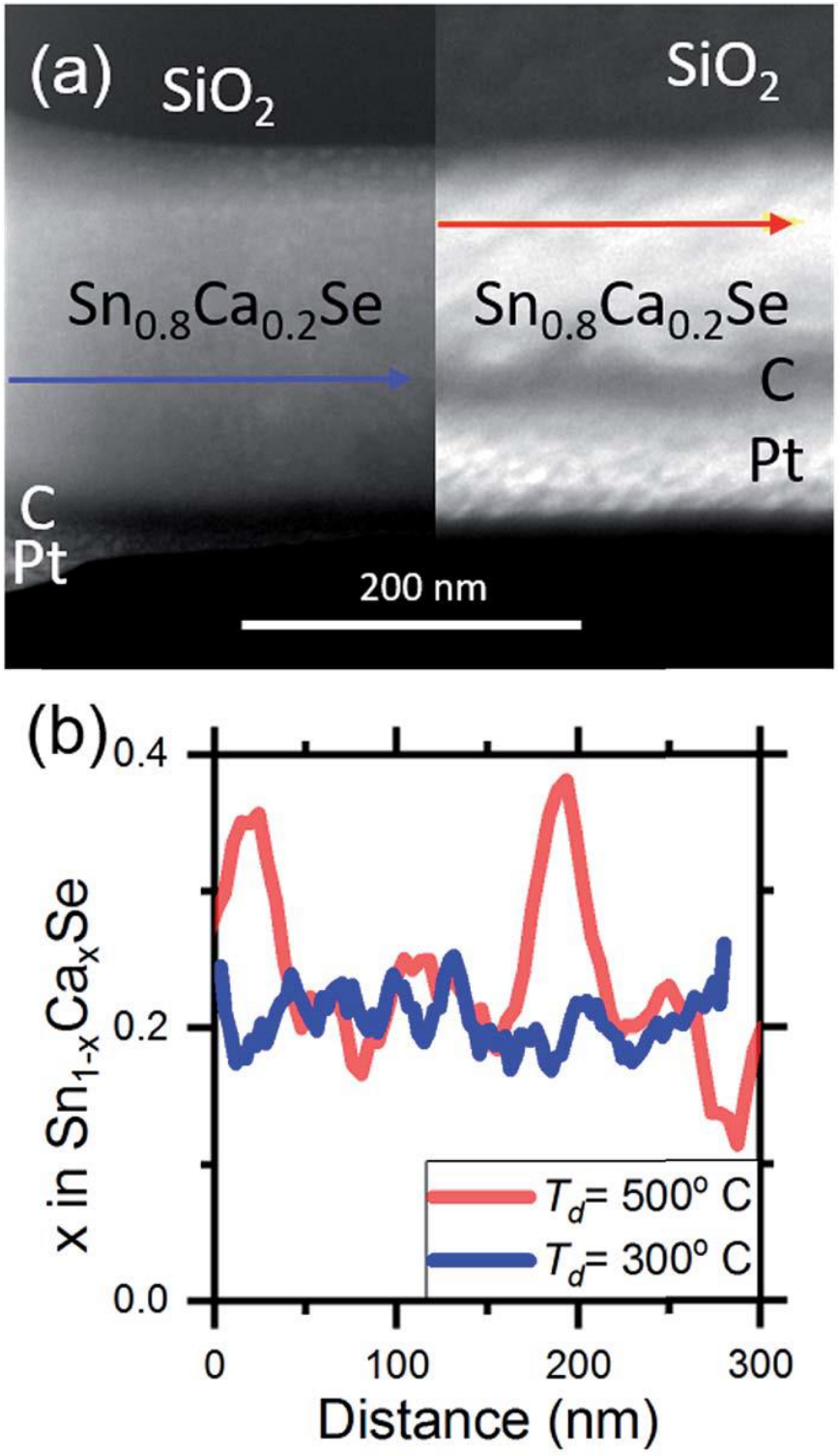

Figure 2.23. a) Cross-sectional Z-contrasted STEM images of $Sn_{0.8}Ca_{0.2}Se$ films grown at 300° C (left) and 500° C (right) along with the position of EDS scans performed. b) Results of EDS line scans showing the Ca content x along the lines in a) showing the compositional variation is much greater in the 500° film than in the 300° film.

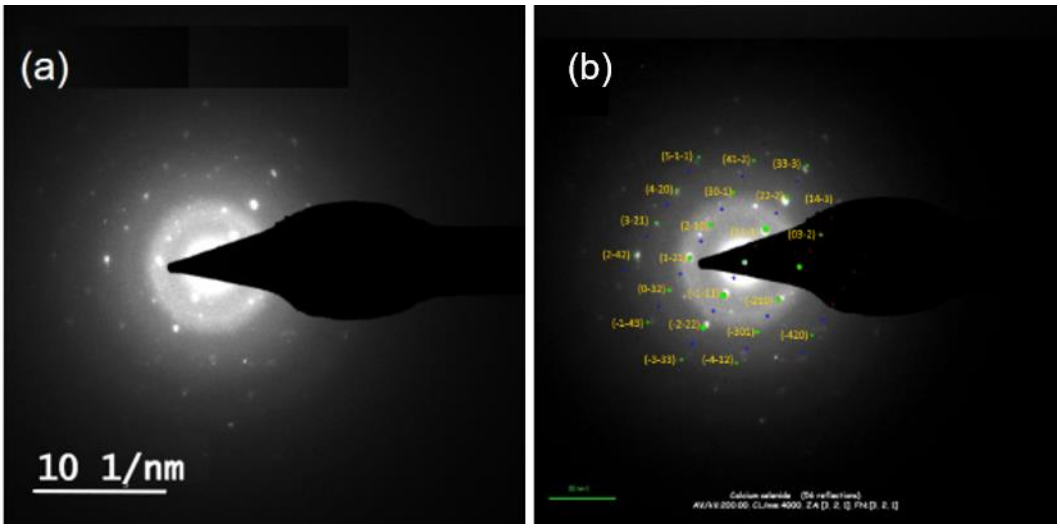

Figure 2.24. Electron diffraction pattern of the spinodally-separated sample showing the RS pattern. a) The pattern displayed without the labeled reflections for clarity and b) the labeled reflections consistent with the RS [123] zone axis.

300^{o} C and was kinetically stabilized in the RS structure while the sample shown on the right was grown at 500^{o} C and was suspected to show some spinodal decomposition. The sample on the left looks uniform in the STEM image, while the higher temperature film has dark grey striations, suggestive of higher concentrations of Ca. Figure 2.23a also shows the positions and directions along which EDS line scans were performed (perpendicular to the growth direction) to authenticate the reason for the dark streaks in the STEM image and to determine compared the spatial compositions of both samples in Figure 2.23b. The compositional line for the sample grown at 500^{o} C (red) varies quite extensively, from nearly Δx = 0.3 in only 150 nm compared the 300^{o} C sample (blue) which is comparatively uniform on that length scale. The composition of the higher temperature sample also appears to fluctuate in a wavelength manner consistent with a spinodal wavelength of ~150 nm. To verify the crystal structure is maintained throughout the region of compositional variation expected for spinodal decomposition, we employed electron nanodiffraction of a FIB cross-sectional TEM sample. While in the standard method of selected area electron diffraction (SAED) the size of beam-illuminated sample is chosen by selecting between a few pre-installed apertures (the smallest of which illuminates ~100nm in diameter), in electron nanodiffraction, the beam can be manually narrowed to nearly the size of a single crystal in the film (~5-10 nm in diameter). The film was analyzed at multiple tilt angles and at multiple positions to try to determine if the film was single phase on this scale. Patterns were found to be

consistent with the RS structure. Figure 2.24a shows one resulting electron diffraction pattern along the [123] zone axis. The main reflections are labeled in Figure 2.24b. From this we conclude the veracity of the predicted phase diagram and note that samples grown near the edge of the spinodal region may separate both binodally and spinodally.

2.5.2 Optoelectronic Properties

Figure 2.25 plots the experimentally measured optical band gaps of alloyed $Sn_{1-x}Ca_xSe$ films (black) along with the GW weighted, DFT calculated band gaps (blue and red) (see Methods 2.21) from Figure 2.16a for comparison over the entire composition range. These films are the same as those whose XRD patterns are depicted in Figure 2.17.

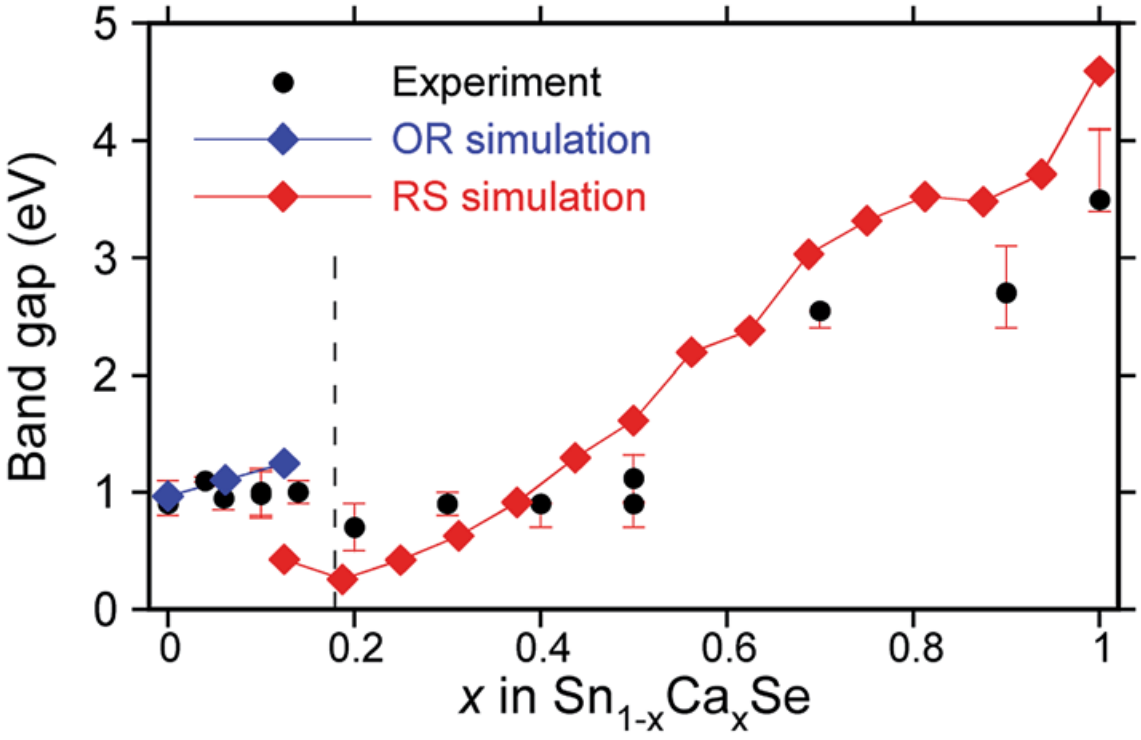

Figure 2.25. $Sn_{1-x}Ca_xSe$ experimental band gaps (black) with GW weighted DFT calculated band gaps for OR (blue) and RS (red) structures for reference.

The calculated band gap increases non-linearly from SnSe to CaSe with a sharp, discontinuous decrease at the predicted structural change. While measured band gaps do not absolutely align with the theory, they do qualitatively follow the trend of the theoretical band gaps. Although the abrupt non-linear jump in band gap near the transition region is not as pronounced, the band gap in the RS structure is lower than the OR band gap near the critical composition, and the gap increases

strongly at large Ca concentration. As with the $Sn_{1-x}Ca_xS$ alloys, the experimental gaps are only a single measure of the optical properties and can be easily influenced by even small levels of impurities and by the choice of range of data to extrapolate to the absorption onset. Nonetheless, the agreement between these calculated and measured band gap trends is quite encouraging. The film thicknesses, obtained from the reflectance and transmission interference fringes, are used for calculation of carrier concentrations and resistivity (below) and are in good agreement with direct measurements in the TEM.

Figure 2.26 shows the carrier concentration *p*, resistivity ρ, mobility μ, Seebeck coefficient *S*, and power factor $PF = S^2/\rho$ for the $Sn_{1-x}Ca_xSe$ alloy films shown in Figure 2.17 and 2.25. SnSe and the conductive alloys exhibit hole-type conductivity as measured by the Hall and Seebeck effects. The most striking feature that has been consistently observed is the large increase in carrier concentration near the structural phase transition, and the concomitant change of 3 orders of magnitude in resistivity. This composition also corresponds to the minimum in the optical band gap. Such a feature is reasonable as defect states become more accessible and more effective at producing charge carriers if the gap is small, which is consistent with our observed optical measurements. The mobility μ is generally moderate (1–10 $cm^2V^{-1}s^{-1}$) and while much lower that the best single-crystal SnSe (100–200 $cm^2V^{-1}\ s^{-1}$),[36,37] is similar to oxides and other chalcogenides useful for thermoelectric applications.[38] The mobility does initially increase as predicted from the DFT effective mass (Figure 2.5b) but then decreases to about 1 $cm^2V^{-1}s^{-1}$, likely due to disorder in the film with the incorporation of Ca into the lattice. The Seebeck coefficient *S* follows a similar trend to ρ, as in most materials (in metals ρ and *S* are small while in semiconductors they are larger). The tradeoff between *S* and ρ is revealed by the *PF*, with larger values being more useful for thermoelectric applications. In this alloy system, the dramatic drop in resistivity at the structural transition is accompanied by only a modest decrease in the Seebeck coefficient from about 350 mV K^{-1} to about 40 mV K^{-1} (one order drop instead of three), with the result that the PF is strongly enhanced. We measure a room temperature *PF* of 1.7 mW cm^{-1} K^{-2} at a composition of $x = 0.16$. Bi_2Te_3, the standard high-performance thermoelectric material, has a room temperature *PF* of 2–9 mWcm^{-1} K^{-2},[39] and $Bi_2(Se,Te)_3$ alloys similarly have a room temperature *PF* = 1–10 mW cm^{-1} K^{-2}.[40] Polycrystalline films of SnSe reportedly have *PF*s of order ~1.25 mW cm^{-1} K^{-2}.[27,28] We note that at room temperature with the parameters reported for these alloy films, the thermal conductivity will be determined by the phonon contribution because the electronic contribution is

small: $\kappa_{el} = LT/\rho \approx 0.025$ W m_{-1} K_{-1}, where L = 2.44 × 10^{-8} WΩK^{-2} is the Lorenz number for degenerate semiconductors. We do not know the origin of the change in the Seebeck coefficient near alloy structure transition, nor why it seems to lag the change in conductivity, causing the maximum in the power factor, but we note a report of a similar change

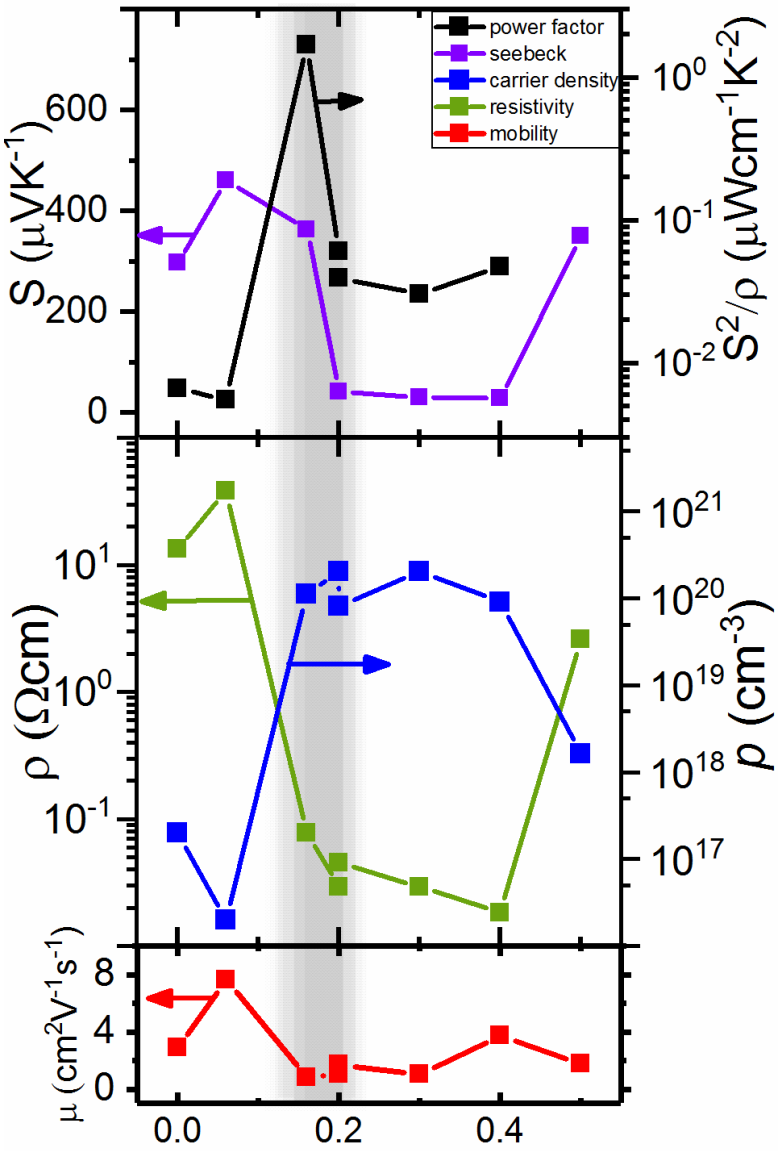

Figure 2.26. Electrical transport properties for select compositions of $Sn_{1-x}Ca_xSe$. Seebeck Coefficient S (top, left axis), Power Factor S^2/ρ (top, right axis), resistivity ρ (middle, left axis), carrier concentration p (middle, right axis), and Hall mobility μ (bottom).

in Seebeck coefficient over a very narrow composition range in $Sn_{1-x}Ge_xSe$,[41] although in that case, the change occurs only within the orthorhombic phase.

Because CaSe has strong electron-hole interactions, appearing as the occurrence of excitons which heavily affect the observed optical properties, it seemed likely that the optical properties of $Sn_{1-x}Ca_xSe$ might also be affected by these electron-hole interactions, particularly in the cubic phase, and thus may not be accurately described by the DFT or GW calculated optical properties. To confirm whether there might be excitonic effects in the alloys, BSE calculations were performed by Derfor both electron-hole interacting and non-interacting cases. The resulting extinction coefficients for both cases are shown in Figure 2.27 for select compositions, the thinner curves with black dots are for the non-interacting case. These curves roughly correspond to the shape expected for the

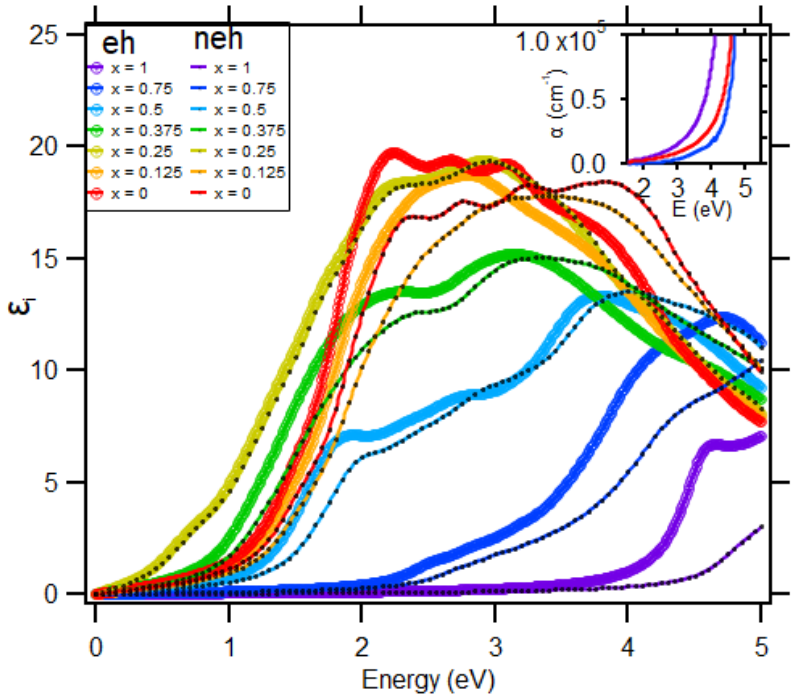

Figure 2.27. Extinction coefficients for both electron-hole interacting (wide curves) and non-interacting (thin curves with black dots) calculations. The inset compares experimental absorption (blue) to the interacting theoretical absorption (purple) and non-interacting theoretical absorption (red).

optical absorption. As we might expect, the onset does not linearly march towards higher energies but instead initially increases, jumps to lower energies, then increases steadily from there. The energy at which the onset occurs for each composition is different between the interacting and

non-interacting cases, and the deviation between the two increases with Ca, as we might expect since the we know the interactions are important for the CaSe case but not for SnSe. We can see

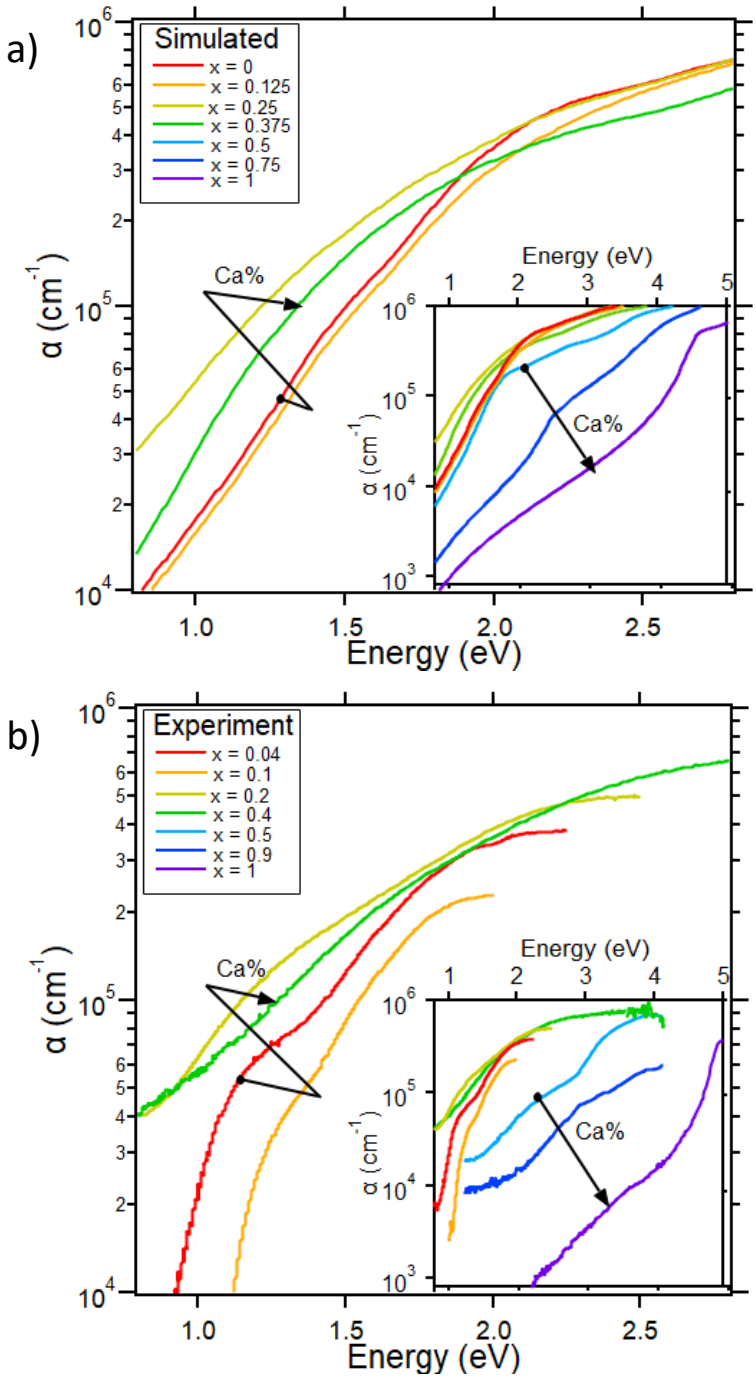

Figure 2.28. Optical absorption for select compositions a) resulting from the electron-hole interacting theory and b) resulting from the experimentally determined transmission and reflectance. The insets show the full ranges of compositions, while the larger frame shows more closely the trend at lower Ca concentrations.

that the onset is lower for the interacting case, which is encouraging for the experimentally derived band gaps, which were a bit low for the higher Ca concentrations. The inset in Figure 2.27 compares the optical absorption of experimental CaSe (blue), electron-hole interacting theory (purple), and electron-hole non-interacting (red) theory. We see that the shape of the interacting curve matches much closer to experiment than the non-interacting. The optical absorption for the full range of compositions of the interacting calculation is shown in Figure 2.28a and for the experimental in Figure 2.28b. For both experiment and calculation, the trend for low Ca samples is shown in the larger window and the trend for the full range is shown in the inset. We see that the overall trends of the onsets of absorption for the experimental follow that of the calculated, and, while there is clearly more structure in the experimental data, the overall shapes fit surprisingly well, particularly for $x = 0.9$ and $x = 1$. From this we conclude that the more advanced calculations which incorporate appropriate interactions can be very beneficial in understanding and predicting the optical properties of new, and even metastable, materials.

2.6 Summary

Metastable heterostructural alloys $Sn_{1-x}Ca_xS$ and $Sn_{1-x}Ca_xSe$ (and select properties for each alloy) have been predicted and then synthesized by PLD (and RF sputtering for $Sn_{1-x}Ca_xS$) in thin film form. Single-phase, crystalline samples were stabilized over the entire range of compositions ($0 < x < 1$). The predicted structural change was observed in both $Sn_{1-x}Ca_xS$ and $Sn_{1-x}Ca_xSe$ near the predicted transitional composition, showing that theory can predict metastable materials and be relatively helpful in the experimental synthesis and subsequent characterization. The optoelectronic properties were measured and were compared to the theory, showing reasonable accuracy. While most $Sn_{1-x}Ca_xS$ alloys synthesized in this study are likely too resistive for satisfactory PV devices, there is much room for improvement in the sample quality. On the other hand, $Sn_{1-x}Ca_xSe$ alloys were surprisingly conductive and demonstrated extraordinarily good thermoelectric properties. We also established that, while DFT and GW are generally accurate for calculating optical properties, materials that exhibit excitonic behavior require higher quality calculation methods to account for the electron-hole interactions.

---

[1] T. Kirchartz and U. Rau. “What Makes a Good Solar Cell?” *Adv. Energy Mater*. **2018.** 1703385

[2] L.A. Coldren and S.W. Corzine. "Diode Lasers and Photonic Integrated Circuits." *Wiley Interscience*. **1995**

[3] A. Abdelrahman, W. Yunus, A. Arof. "Optical Properties of Tin Sulphide (SnS) Thin Film Estimated from Transmission Spectra." *Journal of Non-Crystalline Solids*. 358. **2012**. 1447-1451
[4] R. Banai, H. Lee, M. Motyka, R. Chandrasekharan, N. Podraza, J. Brownson, M. Horn. "Optical Properties of Sputtered SnS Thin Films for Photovoltaic Absorbers." *IEEE Journal of Photovoltaics.* **2013**. 3(3) 1084-1089
[5] J. Vidal, S. Lany, M. d'Avezac, A. Zunger, A. Zakutayev, J. Francis, and J. Tate. "Band-Structure, Optical Properties, and Defect Physics of the Photovoltaic Semiconductor SnS." *Appl. Phys. Lett*. **2012**. 100. 032104.
[6] K. Yoshikawa, H. Kawasaki, W. Yoshida, T. Irie, K. Konishi, K. Nakano, T. Uto, D. Adachi, M. Kanematsu, H. Uzu, and K. Yamamoto. "Silicon Heterojunction Solar Cell with Interdigitated Back Contacts for a Photoconversion Efficiency over 26%." *Nature Energy.* **2017**. 2(5) 17032
[7] W. Shockley and H. J. Queisser. "Detailed Balance Limit of Efficiency of p-n Junction Solar Cells." *Journal of Applied Physics*. **1961**. 32(3). 510-519,
[8] M. H. Futscher and B. Ehrler. "Efficiency Limit of Perovskite/Si Tandem Solar Cells." *ACS Energy Lett.* **2016.** 1(4). 863
[9] P. Sinsermsuksakul, L. Sun, S. W. Lee, H. H. Park, S. B. Kim, C. Yang, and R. G. Gordon. "Overcoming Efficiency Limitations of SnS-Based Solar Cells." *Adv. Energy Mater.* **2014**. 4. 1400496
[10] P. A. Fernandes, M. G. Salomé, J. P. Leitão, and A. F. da Cunha. "Thermodynamic Pathway for the Formation of SnSe and SnSe2 Polycrystalline Thin Films by Selenization of Metal Precursors." *Cryst. Eng. Comm.* **2013**. 15. 10278
[11] E. Barrios-Salgado, M. T. S. Nair, and P. K. Nair. "Chemically Deposited SnSe Thin Films: Thermal Stability and Solar Cell Application." **2014**. 3(8). Q169
[12] C. Gueymard, "The Suns Total and Spectral Irradiance for Solar Energy Applications and Solar Radiation Models," *Solar Energy*. **2004.** 423
[13] Conversion J.P. Singh, and R.K. Bedi. "FTO/SnSe Heterojunction for Photovoltaic." *Jpn. J. Appl. Phys*. **1990**, 29, L792
[14] K.F.A.E. Rahman, A.A.A. Darwish, and E.A.A.E. Shazly. "Electrical and Photovoltaic Properties of SnSe/Si Heterojunction." *Mater. Sci. Semicond. Process*. **2014**. 25. 123
[15] S. Sassi, C. Candolfi, J.-B. Vaney, V. Ohorodniichuk, P. Masschelein, A. Dauscher, and B. Lenoir. "Assessment of the Thermoelectric Performance of PolycrystallineP-type SnSe." *App. Phys. Lett*. **2014**. 104. 212105
[16] L.-D. Zhao, S.-H. Lo, Y. Zhang, H. Sun, G. Tan, C. her, C. Wolverton, V. P. Dravid, and M. C. Kanatzidis. "Ultralow Thermal Conductivity and High Thermoelectric Figure of Merit in SnSe Crystals." *Nature*. **2014**. 508. 373
[17] T. Inoue, H. Hiramatsu, H. Hosono, and T. Kamiya. "Heteroepitaxial Growth of SnSe Films by Pulsed Laser Deposition Using Se-rich Targets." *Jour. App. Phys*. **2015.** 118. 205302
[18] Z. Wang, J. Wang, Y. Zang, Q. Zhang, J. Shi, T. Jiang, Y. Gong, C. Song, S. Ji, L. Wang, L. Gu, K. He, W. Duan, X. Ma, X. Chen and Q. Xue. "Molecular Beam Epitaxy-Grown SnSe in the Rock-Salt Structure: An Artificial Topological Crystalline Insulator Material." *Adv. Mater*. **2015**. 27. 4150
[19] T. Inoue, H. Hiramatsu, H. Hosono and T. Kamiya. "Nonequilibrium Rock-Salt-Type Pb-Doped SnSe with High Carrier Mobilities ≈ 300 $cm^2/(Vs)$." *Chem. Mater*. **2016.** 28. 2278.
[20] J. Vidal, S. Lany, J. Francis, R. Kokenyesi and J. Tate. "Structural and Electronic Modification of Photovoltaic SnS by Alloying." *J. Appl. Phys*. **2014**. 115. 113507.

[21] Claude Yoder. Wired Chemist. **2018**. http://www.wiredchemist.com/chemistry/data/atomic-and-ionic-radii
[22] A. M. Holder, S. Siol, P. F. Ndione, H. Peng, A. M. Deml, B. E. Matthews, L. T. Schelhas, M. F. Toney, R. G. Gordon, W. Tumas, D. S. Ginley, J. D. Perkins, B. P. Gorman, J. Tate, A. Zakutayev and S. Lany. "Novel Phase Diagram Behavior and Materials Design in Heterostructural Semiconductor Alloys." *Sci. Adv*. **2017**. 3 e1700270
[23] S. Poncé, B. Bertrand, P.F. Smet, D. Poelman, M. Mikami, and X. Gonze. "First-Principles and Experimental Characterization of the Electronic and Optical Properties of CaS and CaO." *Optical Materials.* **2013**. 35. 1477
[24] L. Louail, K. Haddadi, D. Maouche, F. A. Sahraoui, and A. Hachemi. "Electronic Band Structure of Calcium Selenide Under Pressure." *Physica B.* **2008**. 403. 3022
[25] H. Peng, P. F. Ndione, D. S. Ginley, A. Zakutayev and S. Lany. "Design of semiconducting tetrahedral $Mn_{1-x}Zn_xO$ alloys and their application to solar water splitting." *Phys. Rev. X*. **2015**. 5. 021016.
[26] J. Harl and G. Kresse. "Cohesive Energy Curves for Noble Gas Solids Calculated by Adiabatic Connection Fluctuation Dissipation Theory." *Phys. Rev. B.* **2008**. 77. 045136.
[27] C.-L. Chen, H. Wang, Y.-Y. Chen, T. Day and G. J. Snyder. "Thermoelectric Properties of P-type Polycrystalline SnSe Doped with Ag." *J. Mater. Chem. A.* **2014**. 2. 11171
[28] S. Sassi, C. Candolfi, J.-B. Vaney, V. Ohorodniichuk, P. Masschelein, A. Dauscher and B. Lenoir. "Assessment of the Thermoelectric Performance of Polycrystalline P-type SnSe." *Appl. Phys. Lett*. **2014**. 104. 212105
[29] B. E. Matthews, A. M. Holder, L. T. Schelhas, S. Siol, J. W. May, M. R. Forkner, D. Vigil-Fowler, M. F. Toney, J. D. Perkins, B. P. Gorman, A. Zakutayev, S. Lany, and J. Tate. "Using Heterostructural Alloying to Tune the Structure and Properties of the Thermoelectric $Sn_{1-x}Ca_xSe$." *J. Mater. Chem. A.* **2017**. 5. 16873
[30] D. Vigl-Fowler, S. Lany, A. M. Holder, B. E. Matthews, J. May, and J. Tate. "Optical Properties of $Sn_{1-x}Ca_xSe$ Alloys." (Awaiting submission)
[31] X. Xu, "Perturbation of the Substrate Temperature by the Impingement of Laser Ablated Particles". *J. Appl. Phys*. **1995** .77(12). 6715
[32] A. W. Welch, P. Zawadzki, S. Lany, C. A. Wolden, A. Zakutayev. "Self-regulated Growth and Tunable Properties of $CuSbS_2$ Solar Absorbers." *Sol. Energ. Mater. Sol. Cells.* **2015**. 132. 499
[33] T. Mitsunaga. "X-ray Thin-film Measurement Techniques II. Out-of-plane Diffraction Measurements." *The Rigaku Journal.* **2009.** 25(1)
[34] Y. P. J. Lensch-Falk, E. S. Toberer, D. L. Medlin and G. J. Snyder. "High Thermoelectric Performance in PbTe Due to Large Nanoscale Ag_2Te Precipitates and La Doping." *Adv. Funct. Mater.* **2011**, 21, 241–249.
[35] L. J. Van der Pauw. *"*A Method of Measuring Specific Resistivity and Hall Effect of Discs of Arbitrary Shape*." Philips Research Reports.* **1958.** 13 1–9
[36] B. B. Nariya, A. K. Dasadia, M. K. Bhayani, A. J. Patel and A. R. Jani. "Electrical Transport Properties of SnS and SnSe Single Crystals Grown by Direct Vapour Transport Technique." *Chalcogenide Lett*. **2009**. 28(10). 549
[37]A. Agarwal. "Synthesis of Laminar SnSe Crystals by a Chemical Vapour Transport Technique." *J. Cryst. Growth*. **1998**. 183. 347
[38] K. Koumoto, I. Terasaki and R. Funahashi. "Complex Oxide Materials for Potential Thermoelectric Applications." *MRS Bull.* **2006**. 31. 206.

[39] C.-H. Kuo, C.-S. Hwang, M.-S. Jeng, W.-S. Su, Y.-W. Chu and J.-R. Ku. "Thermoelectric Transport Properties of Bismuth Telluride Bulk Materials Fabricated by Ball Milling and Spark Plasma Sintering." *J. Alloys Compd.* **2010**. 496. 687.
[40] M.-P. Lu and C.-N. Lia. "Mechanical and Thermal Processing Effects on Crystal Defects and Thermoelectric Transport Properties of $Bi_2(Se,Te)_3$ Compounds." *J. Alloys Compd.* **2013**. 571. 178–182
[41] M. Gharsallah, F. Serrano-S´anchez, N. M. Nemes, F. J. Mompe´an, J. L. Mart´ınez, M. T. Fern´andez-D´ıaz, F. Elhalouani and J. A. Alonso. "Giant Seebeck effect in Ge doped SnSe." *Sci. Rep.* **2016**. 6. 26774

Chapter 3 Transition Metal Nitrides Zn-W-N and Zn-Mo-WN

Contribution of Authors

Stephan Lany from the National Renewable Energy Laboratory (NREL) calculated the stable phases for the Zn-W-N system and constructed the stable phase diagram in Figure 3.3. For quality of transfer of ideas, much of the description on the calculations conducted is his. John Perkins from NREL conducted and analyzed the Rutherford backscattering measurements for select Zn-W-N and Zn-Mo-W-N samples. Elisabetta Arca from NREL contributed much advice on sputtering and appropriate synthesis parameters for the nitride systems. Laura Schelhas from SLAC National Accelerator Laboratory with the help of Elisabetta Arca, Celeste Melamed, and Kevin Talley (all from NREL) provided 2D wide angle x-ray diffraction measurements with integrated data for select Zn-W-N and Zn-Mo-W-N samples.

3.1 Introduction:

Nitrides are a materials group which have achieved increased interest in recent years for the variety of relevant functional properties they possess such as super conductivity, high hardness, piezoelectricity, and even catalytic properties[1,2,3,4]. Nitrides are also interesting because they have been historically understudied and are certainly less understood than their oxide counter parts.[5] Transition metal nitrides are especially interesting as the ability to hold multiple oxidation states allow for broad compositional variations, even in just the binary systems, though ternary nitrides offer even more interesting possible combinations.

Zn-N and W-N are two very different material systems. Zn-N typically is found as the phase Zn_3N_2 which is a mid to wide band gap semiconductor (1.25-3.3 eV)[6,7,8] with an antibixbyite (cubic) lattice. It has a high mobility (~100 cm^2/Vs) so is a candidate to improve transistors and other electronic devices.[9] WN_x exists in a variety of phases with a variety of bandgaps (0-3 eV)[10,11] and has many different use: from high hardness coatings to catalysis in water splitting.[12,13,14] While the most theoretically stable binary, disputed to be W_2N_3 or WN_2, is nitrogen rich,[14],[15] the most stable experimentally observed phase is W_2N.[11]

Ternary nitrides are also a subject of recent interest. Recently a new ternary nitride system Zn-Mo-N has been predicted with a WZ phase ($Pmn2_1$) stable at composition Zn_3MoN_4 and a hexagonal phase stable at $ZnMoN_2$. This system, when synthesized, was found to have intriguing properties optically, electronically, and chemically.[16] The same WZ phase predicted for Zn_3MoN_4 had already been predicted for the Zn-W-N ternary system by Hinuma et al., but not experimentally realized.[17] Due to the vast number of similarities between Mo and W, and even Mo and W nitrides, it was considered whether a version of this ternary nitride substituting W for Mo could be readily synthesized and if the Zn-W-N system would have similar properties to the Zn-Mo-N system. Here we explore the synthesis and stability of $Zn_xW_{1-x}N$, characterizing its electronic and optical properties and comparing them to $Zn_xMo_{1-x}N$. We then briefly explore the alloy of these two systems, $Zn_x(W_yMo_{1-y})_{1-x}N$, and the effect of alloying on the phase stability, crystallinity, and properties.

3.2 Computational Method:

First principles calculations were performed by Stephan Lany from the National Renewable Energy Laboratory using the VASP code[18] in the generalized gradient approximation (GGA)[19] with a Coulomb U = 3 eV parameter[20] for W. Compound formation energies were calculated using the fitted elemental reference energies[21], using $\mu^{fere} = -10.06$ eV determined here for the W_{pv} pseudopotential of the VASP version 4 distribution. Structure prediction was performed using the kinetically limited minimization approach[22,16] for W_2N, WN, W_3N_4, and Zn_3WN_4. The newly predicted structures of W_3N_4 and Zn_3WN_4 have been re-relaxed using the optB86b functional[23] for an improved description of the lattice parameters. The symmetry analysis was performed using the FINDSYM code, and the resulting structure files are given in the supplementary information.

3.3 Experimental Method:

Thin films of $Zn_xW_{1-x}N$ and $Zn_x(W_yMo_{1-y})_{1-x}N$ are produced by reactive sputtering from Zn, W, and Mo metal targets in a high vacuum system (10^{-6} Torr base pressure). Argon gas is used as the sputter gas with flow rates of 10 sccm, with N_2 process gas at 15 sccm. The pressure is raised to 10-20 mTorr for deposition. The samples are grown in a sputter chamber with sputter guns in the configuration indicated in Figure 1a. For the Zn-W-N system, Zn and W metal targets were placed in guns opposite each other as in Figure 1a. Forward powers $W_{Zn} = 35$ W and $25 < W_W < 40$ W, were used to obtain the different compositions reported. For the Zn-Mo-W-N system, another gun (holding the Zn target) was added near the N_2 inlet in Figure 1a and pointed down towards the substrate leading to a light Zn gradient in the y direction. For these samples, the W and Mo metal targets were place across from one another, and powers $25 < W_{Zn} < 35$ W, $25 < W_W < 37$ W, $30 < W_{Mo} < 40$ W. For all samples, each substrate is divided into 44 smaller regions (0.4 cm x 1 cm), as indicated in Figure 1b, to obtain sections which are approximately uniform. The targets are pre-sputtered for 30-60 min before exposing the substrate to the gun plasma, then films are allowed to grow for 60 min at set temperatures $25^o < T_s < 400^o$ C. Before deposition, 2" square EXG glass substrates are cleaned with Liquinox detergent to remove any oil from handling, then washed in an ultrasonic bath of acetone, then isopropel alcohol, for 15 minutes each then blown dry in N_2. Samples grown with substrate heating are adhered to the heater on the sample holder with silver paste to create better thermal contact and allowed to cool under N_2 flow following deposition to reduce loss of N in the sample.

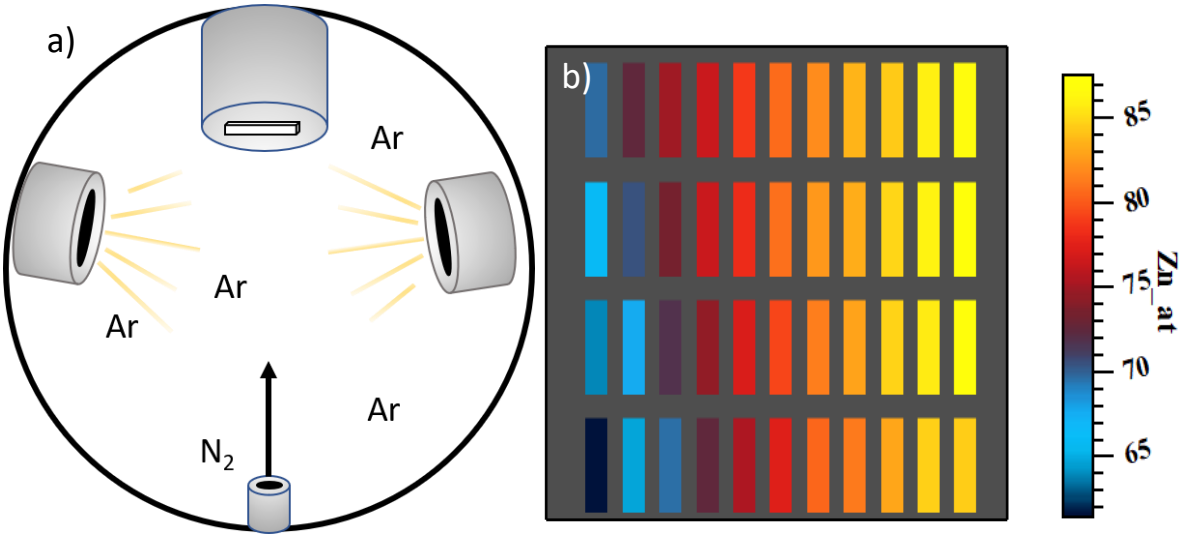

Figure 3.1. a) Configuration of sputtering chamber and b) geometry of sample with separated regions showing the compositional gradient across the rows.

Film composition for all samples is determined by x-ray fluorescence spectroscopy (XRF) for relative metal (M) content. Since N is decidedly difficult to measure reliably by XRF, Rutherford backscatter spectroscopy (RBS) is conducted for select samples to determine the relative M: N and O: N content (some film oxidation is expected due to residual moisture present in the chamber even at high vacuum conditions), as well as, to verify the compositions determined by XRF. Figure 2a shows samples measured in RBS were found to be slightly Zn rich relative to values measured by XRF at low Zn%(1 $Zn\%_{RBS}=1.16Zn\%_{XRF}$). Samples grown with substrate heating, were more oxidized than samples grown at room temperature (~13% at.% and 7% at.% respectively). Almost all samples were slightly nitrogen rich as shown by the M : N ratio in Figure 2b.

Structure and phase are determined by x-ray diffraction (XRD) with a Bruker D8 diffractometer equipped with a HI-STAR 2D detector ($45 < \chi < 135^{o}$) and a spot size ~2 mm x 3 mm. 2D patterns from this detector are integrated to increase signal to noise and reduce orientation effects. All samples are scanned in the range $19 < 2\theta < 53^{o}$, the range where most large and characteristic peaks were expected to be located.

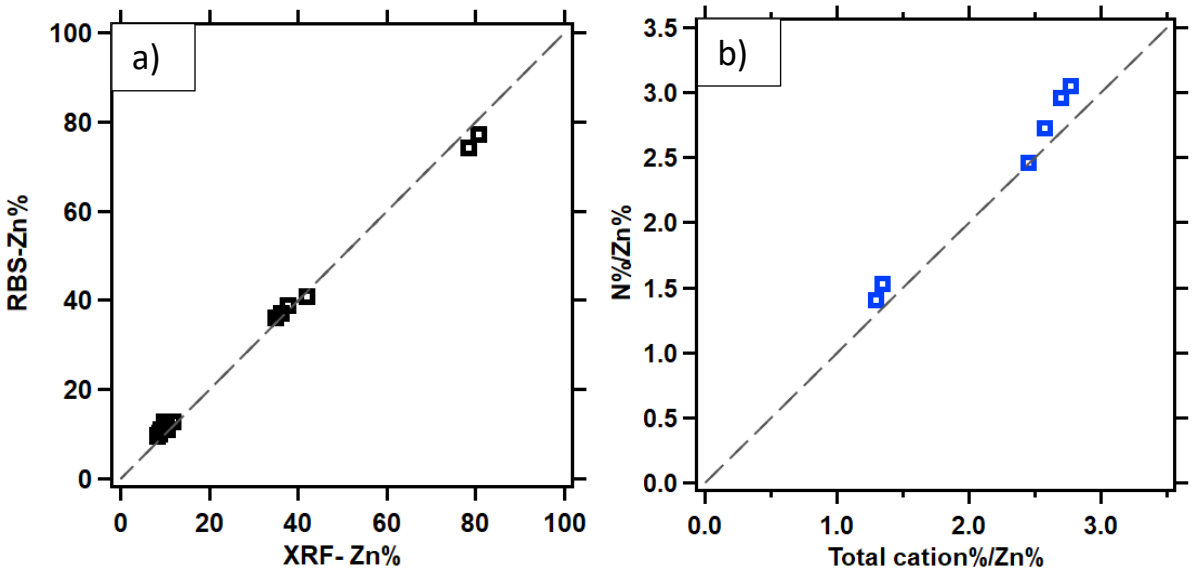

Figure 3.2. a) Zn content as measured by XRF compared to as measured by RBS. XRF deviated more from agreement with RBS at high and low Zn% than at the mid-range compositions. b) RBS measured nitrogen content compared to the total cation content normalized to the Zn content showing samples were relatively nitrogen rich.

For further structural and compositional analysis on a micro-scale, cross-sectional transmission electron microscopy specimens were prepared by focused ion beam lift-out. Scanning electron microscopy (STEM) images were obtained in a Titan 80-200 keV TEM/STEM microscope to observe film quality and uniformity. The specimens were examined for spatial composition by energy dispersive x-ray spectroscopy (EDS) mapping using a ChemiSTEM 4 probe system (four embedded Bruker silicon drift detectors) with drift correction for increased accuracy. For investigating the structure, electron diffraction patterns taken in TEM mode.

The optical transmittance, T, and reflectance, R, are measured in a home-built ultraviolet−visible light−near-infrared (UV-vis-NIR) spectrometer with wavelengths $300 < \lambda < 1100$ nm with a beam diameter of ~1 mm. Optical absorption α is given using the measured transmission and reflectance by

$$\alpha = -\frac{1}{d}\ln\left(\frac{T}{1-R}\right)$$

Electronic sheet resistance R_s are measured by a custom made four-point probe system with ohmic contacts. Resistivity ρ is calculated using thickness obtained using fringes from the optical reflectance which is discussed in more detail in the SI.

3.4 Computational Results:

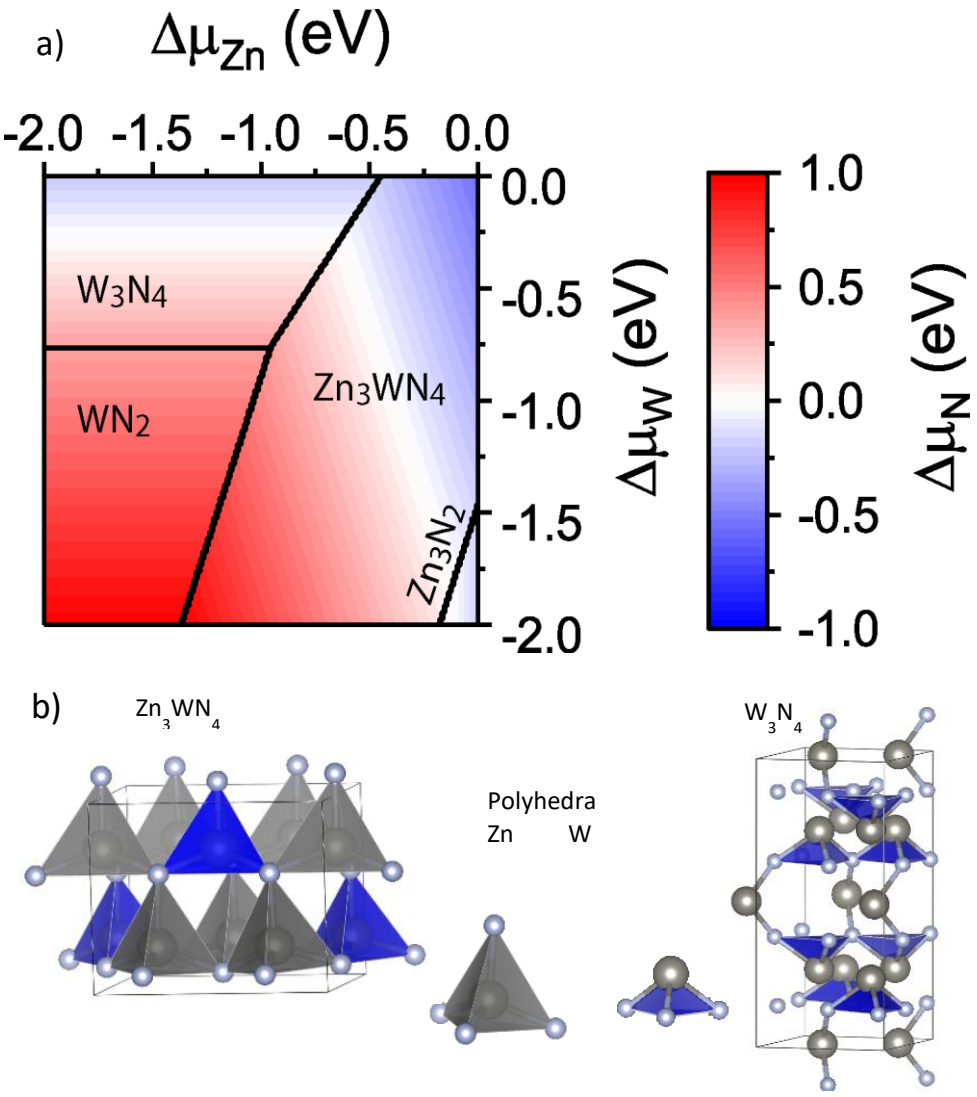

Figure 3.3. a) Stability phase diagram of the alloy $Zn_xW_{1-x}N$ and its respective nitride binaries b) crystal structure for the composition x=0.75 (Zn_3WN_4) and the calculated binary W_3N_4.

Figure 3a shows the predicted phase diagram for then Zn-W-N compound space. We observe a relatively wide stability range for the ternary Zn_3WN_4 between the Tungsten nitrides and the known Zn_3N_2 nitride. Our structure predictions determined a wurtzite-derived orthorhombic structure ($Pmn2_1$; space group 31) for Zn_3WN_4 (Figure 3b left), i.e., the same structure type as we reported in Ref. [16] for Zn_3MoN_4. This 314 composition is an equilibrium stable phase requiring a minimal N chemical potential $\Delta\mu_N \geq -0.54$ eV. In contrast to the Zn-Mo-N, where we predicted a stable $ZnMoN_2$ phase, the corresponding $ZnWN_2$ structure is slightly unstable and does not occur in the phase diagram (Fig. 3a). For the binary nitrides, we find that the pernitride WN_2 is stable for

high non-equilibrium N potentials $\Delta\mu_N \geq +0.38$ eV. The pernitride structure with space group 194 ($P6_3/mmc$) is the same structure type as originally predicted by Wang et al. [24], and recently confirmed by us for MoN_2[16]. We further performed structure sampling for the binary tungsten nitrides with the stoichiometries W_2N, WN, and W_3N_4, and found in all cases lower energy structures compared to the existing entries in the Inorganic Crystal Structure Database. We also considered a recently reported W_2N_3 phase.[3] However, only W_3N_4 occurs as a stable phase in the phase diagram (Fig. 3a). The structure file for the predicted W_3N_4 phase ($CmC2_1$; space group 36) is given in the supplementary material. In the following, we will merely use wurtzite structure (WZ) to describe either the ordered or disordered arrangements of Zn and W on the lattice.

3.5 $Zn_{1-x}W_xN$ Experimental Results

3.5.1 Structure:

The binary end members of this system are Zn_3N_2 (antibixbyite) and W_2N (rock salt cubic). The Zn_3N_2 anitbixbyite structure is not stable under these growth conditions, turning amorphous with even the little of W added (6%; x = 0.94). When enough W is added (x = 0.87), even at room temperature (RT), the predicted WZ phase is stabilized and persists for much of the range of compositions ($0.6 < x < 0.87$). Figure 4a shows a heat map of XRD patterns for $Zn_xW_{1-x}N$ for the range of compositions grown at room temperature (RT). We see from peaks at $2\theta = 32^o$, $2\theta = 34^o$, and $2\theta = 36^o$ that RT samples are crystalline in the range $0.6 < x < 0.9$ and amorphous in the range just above and below. Figure 4b shows the full pattern of a sample with composition $x = 0.74$ measured at SLAC for increased intensity and extended 2θ range. The peaks are all very slightly shifted to lower 2θ when compared to the predicted XRD pattern for the structure, but nearly all peaks are present, and the relative intensity of peaks fit fairly well. Figure 5 is a heat map of $Zn_xW_{1-x}N$ samples grown at 400° C showing two broad peaks which shift between $36.3 < 2\theta < 36.65^o$ and $42.21 < 2\theta < 42.7^o$ which could be consistent with a multitude of alloyed phases such as the (10-10) and (10-11) peaks (at 35.36° and 42.4°) of hexagonal WN_2 (space group 187), (111) and (200) peaks (at 36.82° and 42.78°) of cubic W_3N_4 (space group 221), (111) and (200) peaks (at 35.6° and 41.36°) of cubic WN (space group 225), or the (400) and (332) peaks (at 36.4° and 42.99°) Zn_3N_2 (space group 206). Though the hexagonal $ZnWN_2$ phase fits best, more study is needed for phase confirmation.

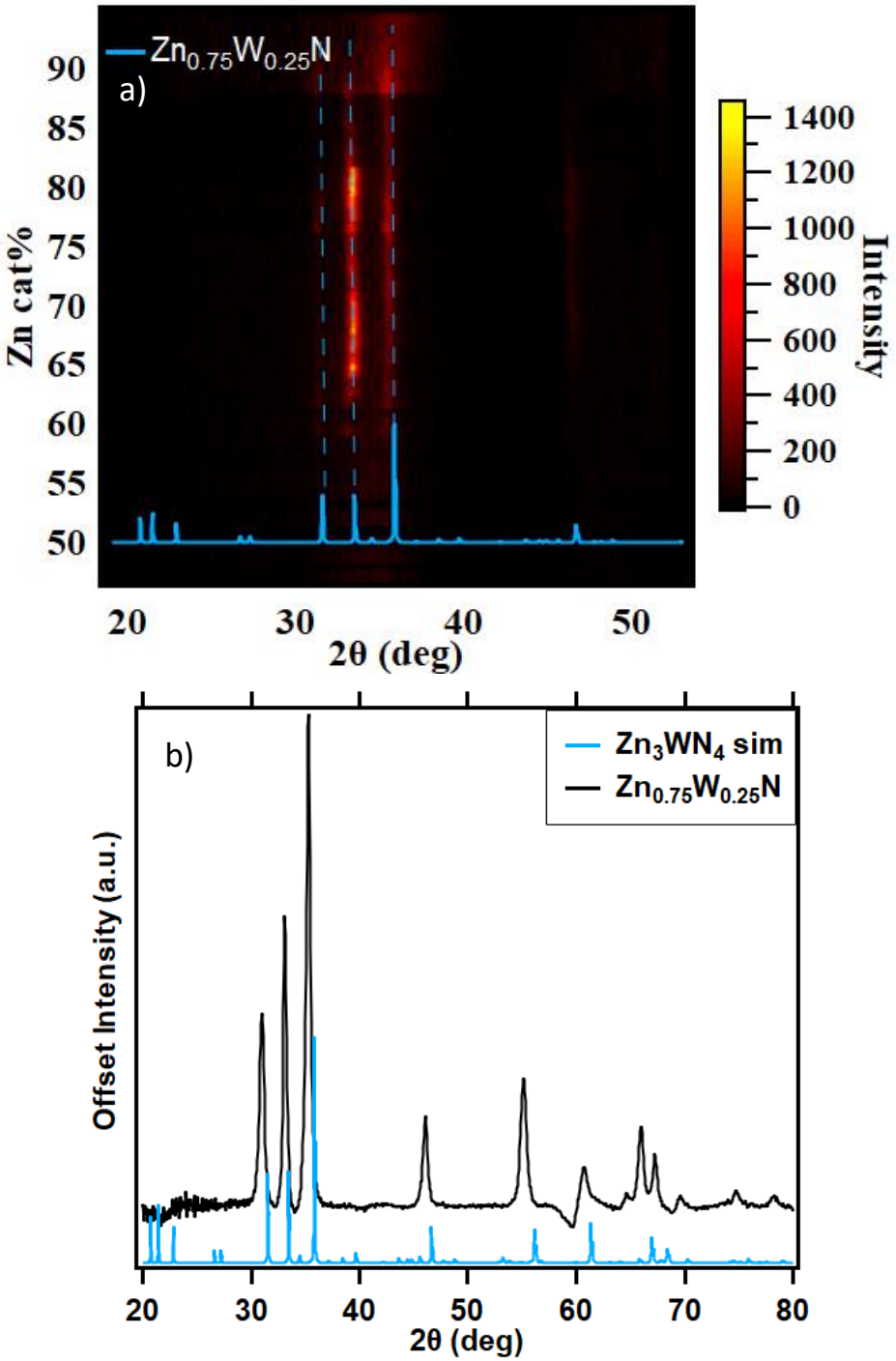

Figure 3.4. a) XRD heat map of $Zn_xW_{1-x}N$ samples grown at RT with lines for peaks of simulated WZ pattern (blue) b) XRD pattern for x = 0.75 with the WZ phase simulated XRD pattern for comparison.

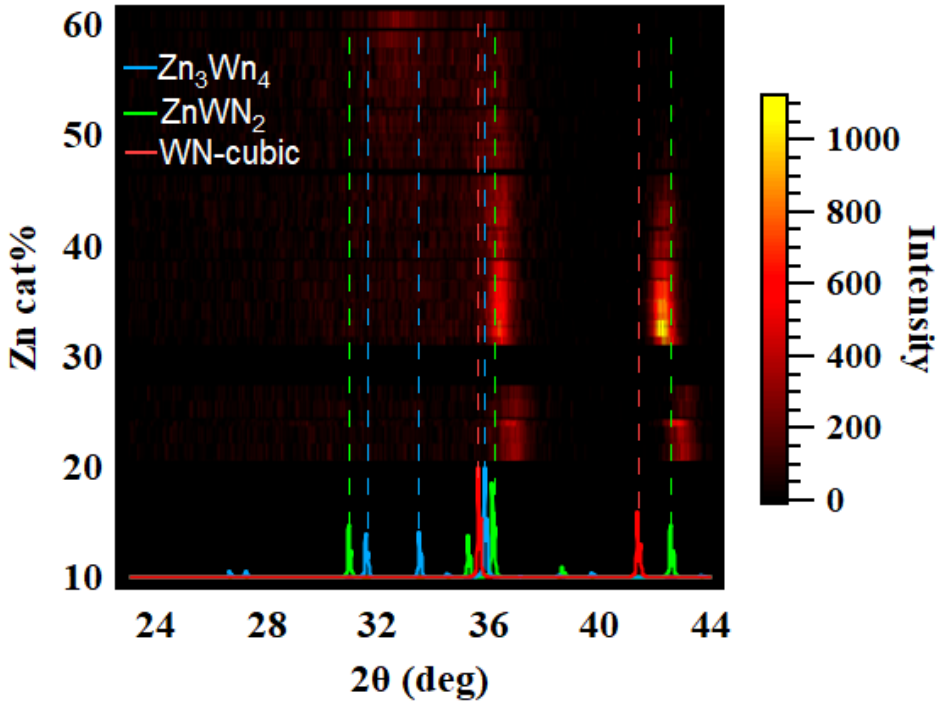

Figure 3.5. XRD heat map of $Zn_xW_{1-x}N$ samples grown at 400° C, with lines for WZ (blue), hexagonal (green), and cubic WN (red) simulated diffraction patterns.

3.5.2 Optoelectronic Properties:

Resistivity measured by 4 point probe method for $Zn_xW_{1-x}N$ samples grown at RT is shown in Figure 6a. We see that for the range of stability for the WZ phase, as shown by the crystalline samples (blue circles), the resistivity does not change significantly, whereas the resistivity changes a nearly two orders of magnitude at lower Zn content ($0.5 < x < 0.6$). Samples' resistivities range from 600 Ωcm to 10^5 Ωcm, which is much more resistive than either Zn_3N_2 (10^{-2} Ωcm)[7,9,25] or WN_x (10^{-5}-10^{-3} Ωcm).[10,26,27] While we expect samples to become more conductive as W changes from a 6+ oxidation state at $Zn_{0.75}W_{0.25}N$ to a 4+ oxidation state at $Zn_{0.5}W_{0.5}N$, similar to the Zn-Mo-N system,[16,28] it is interesting that the resistivity is nearly constant down to about $Zn_{0.6}W_{0.4}N$.

Optical absorption for various compositions calculated using transmission and reflectance is shown in Figure 6b. We see that as Zn is added samples become less absorbing and the onset of absorption becomes sharper, indicative of films becoming less disordered. Such a change is expected since the higher Zn containing samples shown are close to the stable composition. In addition to being optically akin to Zn-Mo-N, Zn-W-N samples are also visually similar, being a

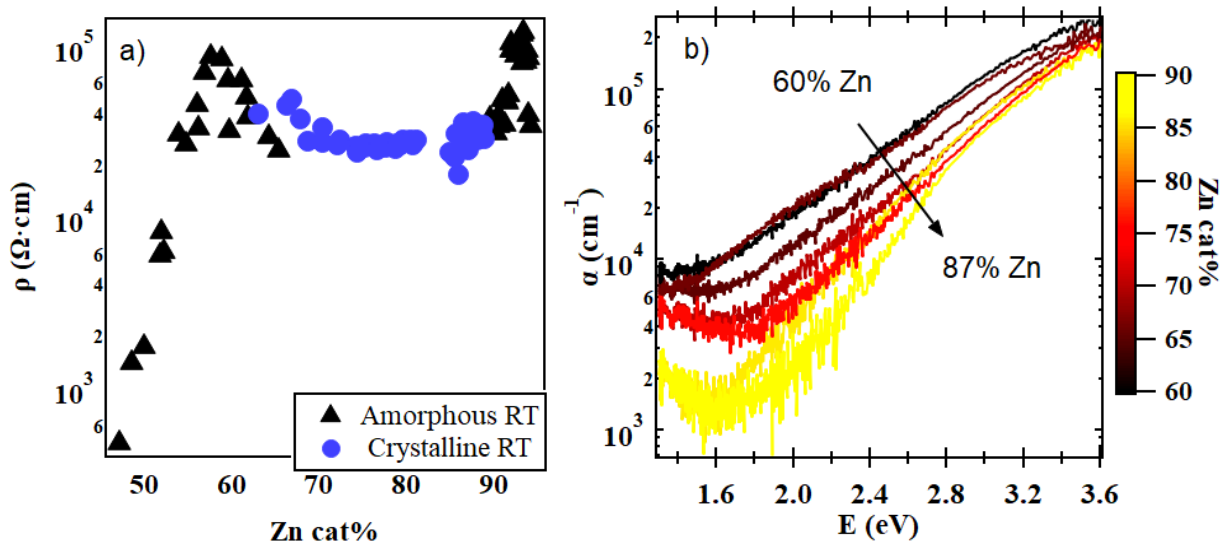

Figure 3.6. a) Four point probe resistivity for $Zn_xW_{1-x}N$ for RT crystalline (blue) and amorphous (black) samples. b) Optical absorption for various compositions of RT samples in the WZ structure.

light transparent yellow at $x = 0.75$ and darkening to a brown as W is added. [16] Optical bandgaps for these samples determined by Tauc plots are in the range 1.7-2.5 eV which is comparable to the range reported for Zn_3N_2.[25,29]

3.6 $Zn_{1-x}(W_{1-y}Mo_y)_xN$ Experimental Results:

3.6.1 Structure:

Figure 7a and 7b show the WZ (002) XRD peak for $Zn_x(W_{1-y}Mo_y)_{1-x}N$ for constant Zn concentrations and compared to the simulated pattern for $Zn_xW_{1-x}N$. This peak clearly shifts to higher 2θ values with increased Mo as might be expected for a lattice contraction to accommodate the smaller atom (tetrahedrally coordinated Mo 6+ or W 6+ ions 0.41 and 0.42 Å respectively).[30]

Figure 7c shows XRD patterns of a higher Zn concentration ($x = 0.8$) for a range of relative Mo/(Mo+W) compositions ($0.58 < y < 0.81$). Compared to stoichiometric Zn_3WN_4, peaks are shifted to lower 2θ, consistent with the tetrahedrally coordinated Zn 2+ ions being a larger (0.6 Å) compared to tetrahedrally coordinated Mo 6+ or W 6+ ions (0.41 and 0.42 Å respectively).[30] There is much less shift of the (002) peak with change y at this Zn concentration since there is less total change in the absolute percentage of Mo to W. The crystallinity of samples as measured by the FWHM is also increases with Mo. Figure 7d shows XRD patterns of a much lower Zn concentration ($x = 0.3$) for a range Mo/(Mo+W) compositions ($0.49 < y < 0.72$). Near $x = 0.35$,

even at RT, we see a similar trend as in $Zn_xW_{1-x}N$: a broad peak at $2\theta = 37^o$ appears, and, as Mo is added, the peak narrows and shifts toward lower 2θ, and another peak appears at $2\theta = 42^o$. These

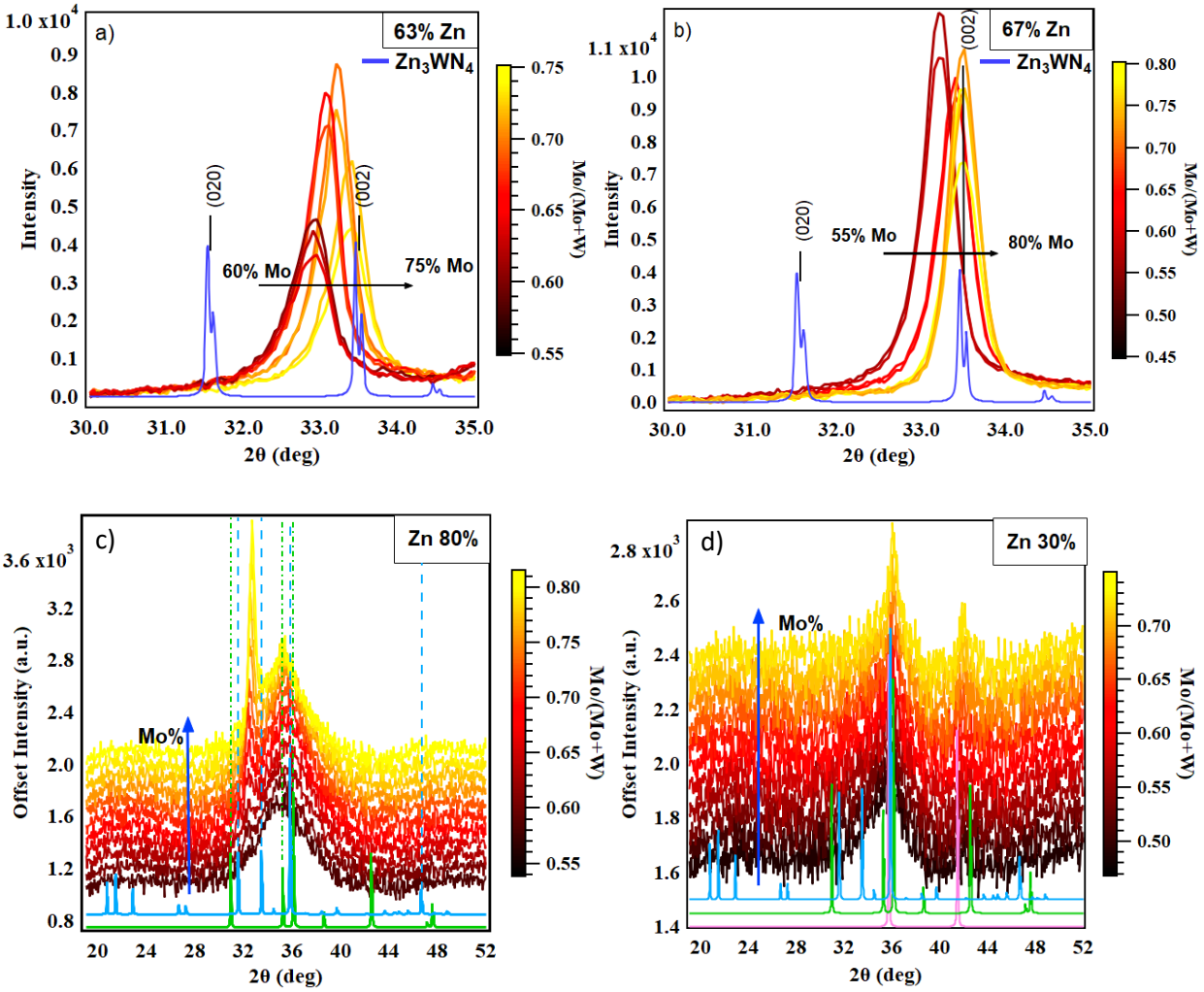

Figure 3.7. XRD patterns for the WZ (002) peak illustrating the shift in 2theta due to Mo/W variation for constant a) 63% and b) 67% Zn with simulated pattern for the phase (blue). XRD patterns for $Zn_x(Mo_yW_{1-y})_{1-x}N$ for constant Zn c) 80% andd) 30% with lines for simulated patterns the WZ phase (blue), hexagonal phase (green), and cubic MoN (cyan).

peaks are consistent with many possible secondary phases, so 2D wide angle x-ray spectroscopy was performed at SLAC to increase the intensity, reduce effects of texturing, and to extend the range of 2θ sampled. Integrated XRD patterns taken at SLAC with $\lambda = 0.9736$ Å (peaks are shifted to lower 2θ relative to the XRD patterns taken with $K_{Cu\alpha}$) are shown in Figure 8 and compared to various reference patterns. Figure 8a shows a 28% Zn sample grown at RT with peaks consistent with cubic WN or MoN, implying as samples become more Zn poor, there is a higher tendency for separation into the binary nitrides.

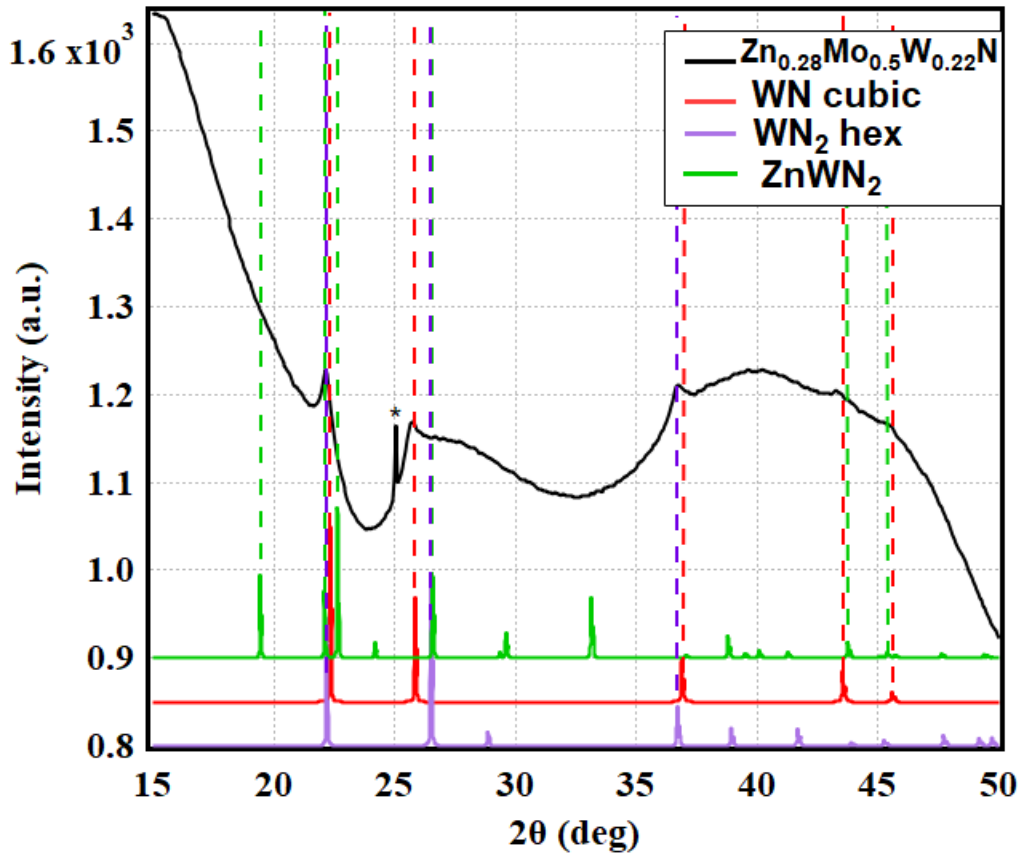

Figure 3.8. X-ray diffraction taken at SLAC (wavelength about equal to a Ag source) for samples with a) 28% Zn grown at RT compared to the predicted hexagonal $ZnWN_2$ (green), cubic WN (red), and hexagonal WN_2 (purple). The large broad humps are due to the amorphous substrate. Stars indicate peaks due to cosmic rays detected by the instrument.

It is not clear from XRD if any of the Zn is incorporated into the lattice of these binary phases or if it is forming amorphous nitride structures, so STEM EDS maps were collected from cross-sectional specimen prepared by focused ion beam (FIB) lift out. Figure 9 shows energy dispersive x-ray spectroscopy (EDS) maps of these samples.

A Zn-Mo-W-N TEM specimen from the sample shown in Figure 3.8 was prepared by FIB lift-out. This sample was analyzed by STEM EDS mapping to check the compositional uniformity. Figure 3.9a shows EDS maps of W (cyan) and Zn (yellow) overlaid for comparison. A Zn-poor region appears near the substrate which correlates with a W-rich region. Figure 3.9b shows the HAADF STEM image of the region analyzed by EDS which was taken at low camera lengths for better

3.6.2 TEM

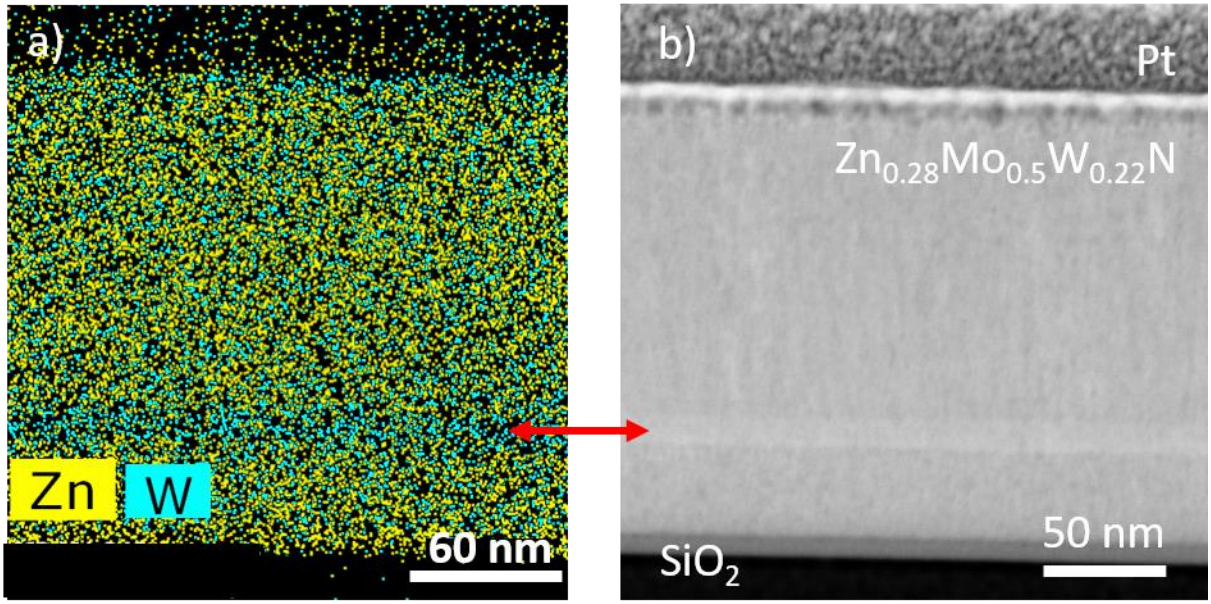

Figure 3.9. a) Overlaid Zn and W EDS maps of TEM specimen from samples grown at RT with 28% Zn and 50% Mo showing a narrow Zn-poor and W-poor layer near the substrate and b) a HAADF STEM image of the region showing the Zn-poor and W-rich region as a bright spot.

elemental contrast. The image clearly shows a bright region indicating a higher concentration of higher atomic number, implying some WN_x or MoN_x has separated from the rest of the film. This agrees with the XRD findings from Figure 3.8 which found the crystalline part of the film to be primarily cubic WN. The rest of the film appeared fairly uniform. While the bulk of the film was not WN, there were also not many other crystalline regions, which may be why no other phases were observed in XRD.

3.6.3 Optoelectronic Properties:

Four-point resistivity is shown in Figure 3.10a, 3.10b, and 3.10c for $Zn_x(W_{1-y}Mo_y)_{1-x}N$ for various concentrations of Mo at constant Zn%. Samples shown in Figure 3.10a were phase separated and the transport properties were dominated by WN but are still shown for comparison. For the rest of the samples, the resistivity ranged between $4 - 6 \times 10^4 \Omega$cm across all samples. The effect of the Zn content in the samples on the resistivity was clearly larger than the effect of changing the amount of Mo. The resistivity increased about two orders of magnitude between $x = 0.62$ and $x = 0.8$, whereas for each constant x and a similar variation of 20% Mo results in a difference in resistivity of less than an order of magnitude. It is interesting to note that for the samples with

lower Zn%, resistivity decreases with increased Mo%, while at the highest Zn%, resistivity increases with increased Mo. Further transport studies to find the carrier type and coordination studies may be able to explain this behavior.

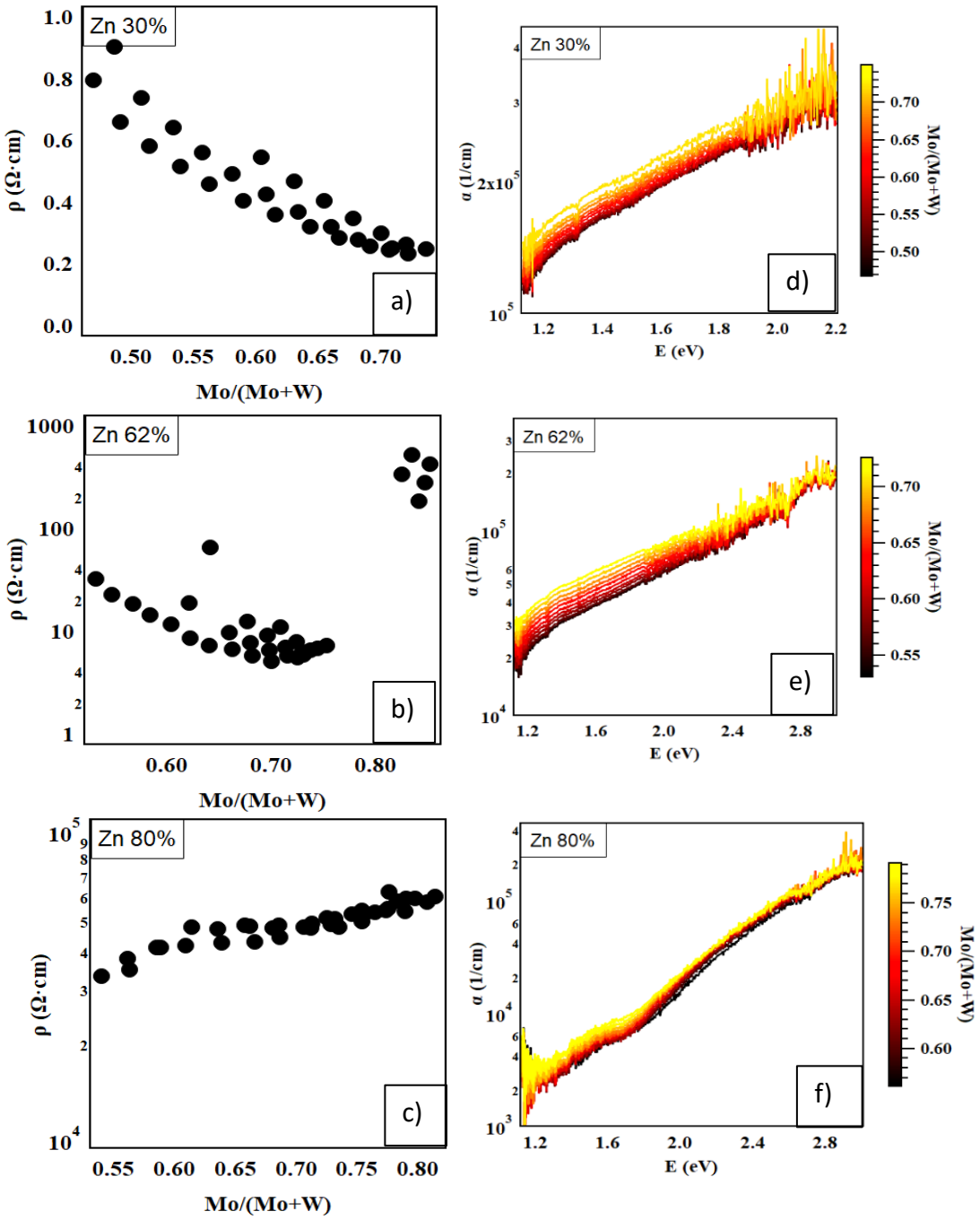

Figure 3.10. Four-point probe resistivity a), b), and c) and optical absorption d), e), and f) of various values of y for constant values of x, a) and d) x=0.8, b) and e) x=0.62, and c) and f) x=0.8. a) and d) samples were known to have WN in them which dominated the electronic measurements but are left for comparison.

Optical absorption for constant Zn% is shown in Figure 10d, 10e, and 10e for the same range of Mo concentration as shown for resistivity. Again, Figure 10d shows samples with WN, which likely affected the optical absorption. The trend for single phase samples is similar to that observed in $Zn_xW_{1-x}N$: at higher Zn content (x = 0.8), the samples are less absorbing, particularly in the visible range, and the onset of absorption is stronger which is consistent with the lower disorder or higher crystallinity seen in the XRD patterns for higher Zn content. For each constant Zn%, the absorption is stronger for higher Mo%. The highest total measurable absorption is about the same for all the samples, peaking around $2x10^5$ cm^{-1}. As with the $Zn_xW_{1-x}N$ samples, samples with higher Zn concentrations were transparent light yellow, as Zn decreased samples became more-opaque indicating absorption in the visible range. Samples with 30% Zn start absorbing in the near infrared as they are already absorbing strongly at the start of the visible range.

3.7 Summary:

We have shown alloys $Zn_xW_{1-x}N$ and $Zn_x(Mo_yW_{1-y})_{1-x}N$ can been synthesized at room temperature by thin film sputtering. Both alloys were stabilized in the WZ structure for Zn rich samples ($0.55 < x < 0.85$), consistent with the structures and enthalpies predicted. Much of the compositional range outside of this is amorphous under the explored growth conditions. Around $x = 0.35$ another phase appears for $Zn_xW_{1-x}N$, consistent with the predicted hexagonal phase at (at T = 400° C for $Zn_xW_{1-x}N$) and with the rock salt cubic phase of either WN or MoN. Optical transmission and reflectance of samples were measured and found have wide range of band gaps (1.7-2.5 eV) and high absorption over a wide range of wavelengths (from the near infrared to near ultra-violet). Electrical resistivities were measured on the order 10^4 Ωcm for the entire range of WZ $Zn_xW_{1-x}N$ and in the range $4 - 6 \times 10^4$Ωcm for $Zn_x(W,Mo)_{1-x}N$. While Zn-W-N can be stabilized into the WZ phase similar to the Zn-Mo-N compound, its material properties are very different, illustrating how a similar structure can be substantially changed by a simple elemental substitution.

---

[1] R.S. Ningthoujam, N.S. Gajbhiye. "Synthesis, Electron Transport Properties of Transition Metal Nitrides and Applications." *Progress in Materials Science.* **2015**. 70. 50–154

[2] J.S.J. Hargreaves. "Hetergeneous Catalysis with Metal Nitrides." *Coordination Chemistry Reviews.* **2013**. 257. 2015– 2031

[3] S. Wang, X. Yu, Z. Lin, R. Zhang, D. He, J. Qin, J. Zhu, J. Han, L. Wang, H. Mao, J. Zhang, and Y. Zhao. "Synthesis, Crystal Structure, and Elastic Properties of Novel Tungsten Nitrides." *Chem. Mater*. **2012**. 24(15). 3023−3028

[4] A. Alexander, J. S. J. Hargreaves. "Alternative Catalytic Materials: Carbides, Nitrides, Phosphides and Amorphous Boron Alloys." *Chem. Soc. Rev.* **2010**. 39. 4388–4401
[5] A. Zakutayev. "Design of Nitride Semiconductors for Solar Energy Conversion." *J. Mater. Chem. A,* **2016**. 4. 6742–6754
[6] A. Trapalis, J. Heffernan, I. Farrer, J. Sharman, and A. Kean. "Structural, Electrical, and Optical Characterization of as Grown and Oxidized Zinc Nitride Thin Films." *J. Appl. Phys*. **2016**. 120. 205102
[7] X. Cao, Y. Ninomiya, N. Yamada. "Zinc Nitride as a Potential High-mobility Transparent Conductor." *Phys. Status Solidi A.* **2017**. 214(2). 1600472
[8] A. Redondo-Cubero, M. Góñmez-Castaño, C. G. Núñez, M. Domínguez, L. Vázquez. J. L. Pau. "Zinc Nitrid Thin Films: Basic Properties and Applications.": *Proc. of SPIE Vol. 10105.* **2017.** 101051B-1
[9] C. G. Núñez, J. L. Pau, M. J. Hernández, M. Cervera, E. Ruiz, J. Piqueras. "On the Zinc Nitride Properties and the Unintentional Incorporation of Oxygen." *Thin Solid Films.* **2012**. 520. 1924–1929
[10] S.H. Mohamed, A. Anders. "Structural, Optical, and Electrical Properties of WOx(Ny) Films Deposited by Reactive Dual Magnetron Sputtering." *Surface & Coatings Technology.* **2006**. 201. 2977–2983
[11] S. Asgary, A. H. Ramezani. "Dependence of Nitrogen/Argon Reaction Gas Amount on Structural, Mechanical and Optical Properties of WN_x Films." *Chin. Phys. Lett*. **2017**. 34(12). 126801
[12] Y. G. Shen, Y.W. Mai, D. R. McKenzie, Q. C. Zhang, W. D. McFall, and W. E. McBride, "Composition, Residual Stress, and Structural Properties of Thin Tungsten Nitride Films Deposited by Reactive Magnetron Sputtering." *J. Appl. Phys*. **2000**. 88(3). 1380
[13] Y. L. Wang, T. Nie, Y. H. Li, X. L Wang, L. R Zheng, A. P Chen, X. Q. Gong, H. G. Yang. "Black Tungsten Nitride as a Metallic Photocatalyst for Overall Water Splitting Operable at up to 765 nm." *Angewandte Chemie*. **2017**. 56(26). 7430
[14] M. J. Mehl, D. Finkenstadt, C. Dane, G. L. W. Hart, and S. Curtarolo. "Finding the Stable Structures of N1-xWx with an Ab Initio High-throughput Approach." *Phys. Rev. B.* **2015**. 91. 184110
[15] Materials Project-W. materialsproject.org
[16] E. Arca, S. Lany, J. D. Perkins, C. Bartel, J. Mangum, W. Sun, A. Holder, G. Ceder, B. Gorman, G. Teeter, W. Tumas, A. Zakutayev. "Redox-Mediated Stabilization in Zinc Molybdenum Nitrides." *J. Am. Chem. Soc.* **2018**. 140(12). 4293
[17] Y. Hinuma, T. Hatakeyama, Y. Kumagai, L. Burton, H. Sato, Y. Muraba, S. Iimura, H. Hiramatsu, I. Tanaka, H. Hosono, F. Oba. "Discover of Earth-Abundant Nitride Semiconductors by Computational Screening and High-Pressure Synthesis." *Nat. Comm.* **2016**. 7
[18] G. Kresse and D. Joubert. "From Ultrasoft Pseudopotentials to the Projector Augmented-wave Method." Phys. Rev. B. **1999**. 59. 1758
[19] J. P. Perdew, K. Burke, and M. Ernzerhof, "Generalized Gradient Approximation Made Simple." *Phys. Rev. Lett.* **1996. 77.** 3865
[20] S. L. Dudarev, G. A. Botton, S. Y. Savrasov, C. J. Humphreys and A. P. Sutton. "Electron-Energy-Loss-Spectra and the Structural Stability of Nickel Oxide: An LSDA+U Study." *Physical Review B.* **1998.** 57. 1505

[21] V. Stevanovic, S. Lany, X. Zhang, and A. Zunger. "Correcting Density Functional Theory for Accurate Predictions of Compound Enthalpies of Formation: Fitted Elemental-phase Reference Energies." Phys. Rev. B **2012**. 85. 115104
[22] P.P. Zawadzki, J.D. Perkins, and S. Lany. "Modeling Amorphous Thin Films: Kinetically Limited Minimization." Phys. Rev. B. **2014**. 90. 094203
[23] J. Klimes, D. R. Bowler, and A. Michaelides, "Van Der Waals Density Functionals Aplied to Solids." *Phys. Rev. B* **2011**. 83. 195131
[24] H. Wang, Q. Li, Y. Li, Y. Xu, T. Cui, A.R. Oganov, and Y. Ma, "Ultra-incompressible Phases of Tungsten Dinitride Predicted from First Principles." *Phys. Rev. B.* **2009**. 79. 132109
[25] T. Wen. "Fabrication of Zinc Nitride Thin Films using RF Sputtering Deposition of Optoelectronic Applications" Disseration. University of Toledo, Dec. 2012
[26] J. Lin, A. Tsukune, T. Suzuki, and M. Yamada. "Different Effect of Annealing Temperature on Resistivity for Stoichiometric, W rich, and N rich Tungsten Nitride Films." *J. Vac. Sci. Technol. A.* **1999**. 17(3). 936
[27] P. Jiang, J. S. Chen, and Y. K. Lin. "Structural and Electrical Characteristics of W-N Thin Films Prepared by Reactive RF Sputtering." *J. Vac. Sci. Technol. A.* **2003**. 21(3). 616
[28] R. P. Tandon and S. Hotchandani. "Electrical Conductivity of Semiconducting Tungsten Oxide Glasses." *Phys. Stat. Sol*. (a). **2001**. 185(2). 453
[29] F. Zong, H. Ma, W. Du, J. Ma, X. Zhang, H. Xiao, F. Ji, C. Xue. "Optical Band Gap of Zinc Nitride Films Prepared on Quartz Substrates from a Zinc Nitride Target by Reactive RF Magnetron Sputtering." *Applied Surface Science.* **2006**. 252. 7983
[30]The Atomistic Simulation Group in the Materials Department of Imperial College. http://abulafia.mt.ic.ac.uk/shannon/ptable.php

Chapter 4 (Scanning) Transmission Electron Microscopy for Metastable Characterization

Contribution of Authors

Elisabetta Arca from the National Renewable Energy Laboratory contributed the MoN_x sample to be studied. Peter Eschbach from Oregon State University helped obtain the EFTEM jump-ratio map and thickness map in Figure 4.4.

4.1 Background

While there are many techniques available to develop an understanding of a material on the micro-scale (e.g. secondary ion mass spectroscopy, x-ray photoelectron spectroscopy, atomic force microscopy, time of flight-secondary ion mass spectroscopy, atom probe tomography …), (scanning) transmission electron microscopes ((S)TEMs) are unique in their ability to run multiple types of experiments on the same sample, sometimes even simultaneously. With the increased prevalence of in-situ experiments, the level of sophistication of equipment used, such as specialized holders (Figure 4.1), has also increased, with new companies (e.g. Hummingbird, DENSsolutions, FEI) being initiated to advance and expand the types of experiments possible.

Figure 4.1. A sample of different TEM holders which allow for different in-situ experiments. From left to right: A holder allowing gas flow onto the sample, a holder allowing voltage biasing of the sample, a holder allowing viewing of liquids, and a holder allowing sample heating[1].

Even without in-situ experiments, there a variety of techniques used in S/TEM for material analysis: energy dispersive x-ray spectroscopy (EDS) and electron energy loss spectroscopy (EELS) for chemical composition and spatial compositional mapping, EELS for analysis of oxidation states of particular elements, various types of electron diffraction for crystal characterization, convergent beam electron diffraction and energy filtered TEM (EFTEM) (and EELS) for cross-sectional thickness, dark field (DF) and bright field (BF) imaging for diffraction

or orientation contrast/imaging, high angle annular DF (HAADF) imaging with higher collection angles for more Z-contrast (rather than diffraction contrast, BF TEM for spatially mapping crystallinity, and likely many more. In this chapter, we will examine how some of these techniques can be used for analysis of metastable materials and provide some examples as well as some cautionary notes.

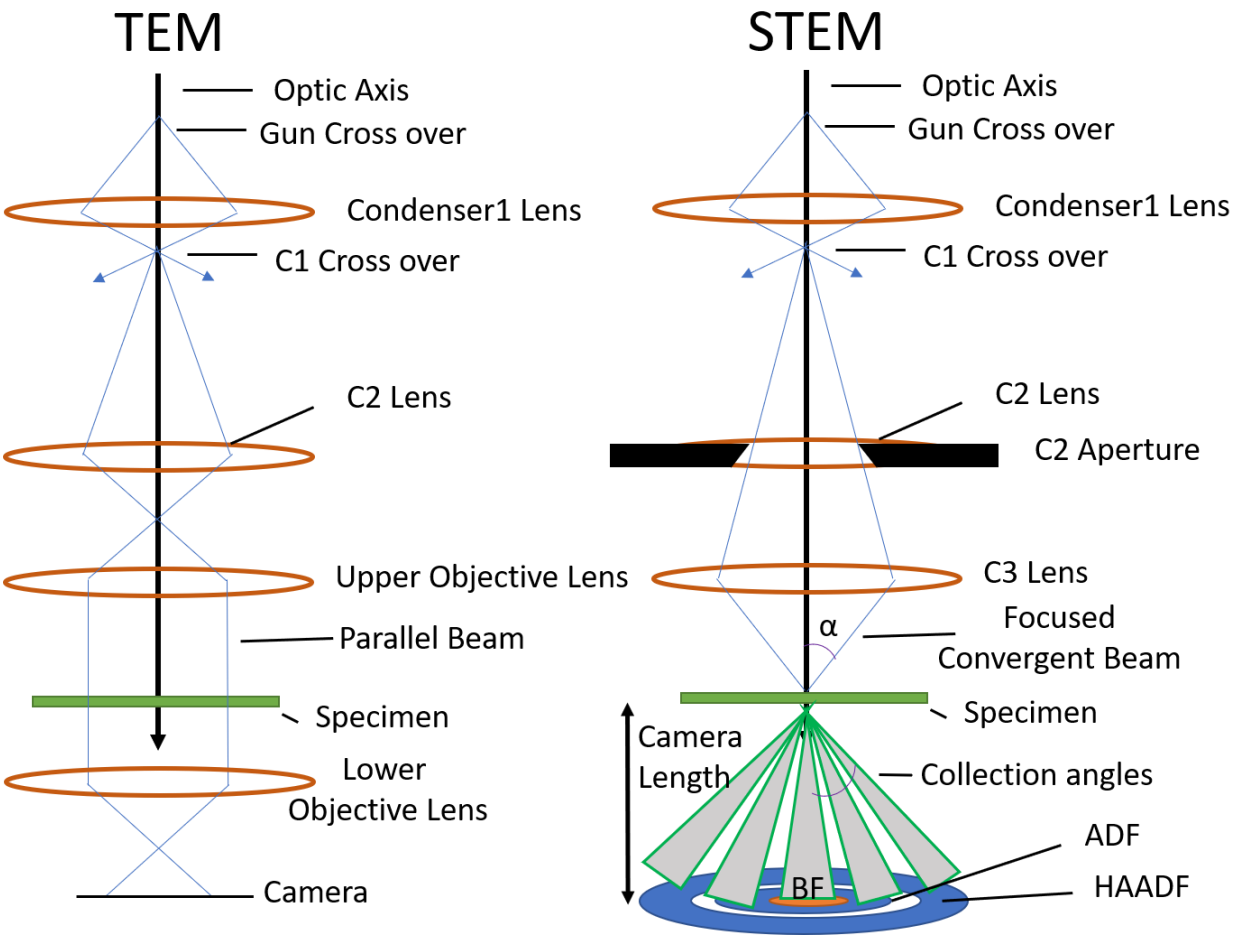

Figure 4.2. Schematics of the lens system of a typical TEM (left) and a STEM (right).

4.2 TEM vs. STEM

Transmission electron microscopy (TEM) is a technique which uses a beam of high energy electrons (typically 200 eV which leads to a small wavelength ~6.22 pm) passing through a specimen to image and analyze small volumes of material. A schematic of the lens system and electron beam is shown in Figure 4.2. Different TEMs may have different numbers of magnetic lenses, but the beam passing through the specimen is usually a parallel beam which allows for

diffraction. A TEM can switch between imaging or diffraction by changing the strength of the lenses after the specimen. A scanning TEM (STEM) makes use of different lenses and apertures to create an image. A focused sub-nanometer beam (typically now < 0.2 nm)[2] is quickly rastered across the specimen (dwell time of 20 μs)[3]. This rastering of the small beam allows for a fine point by point analytics. Additionally, some electrons from the beam spread out by different amounts as they pass through the sample dependent upon the elements they are near to (where proximity to nuclei of higher atomic numbers deflects them further from the center of the beam). This spread can be utilized by having different detectors at different collection angle regimes. At very small collection angles, a bright field (BF) detector is used, and very light elements, which deflect the beam very little, will appear bright in images. At higher angles, an annular dark field (ADF or just DF) detector is used and mid-sized elements appear brighter and diffraction contrast is stronger. Finally, at even higher angles, a high angle annular dark field (HAADF) detector is used in which heavier elements appear bright and light elements appear dark.

4.3 Analytical TEM: EDS

Many of the useful techniques for metastable materials involve checking for compositional uniformity or phase separation. Energy dispersive x-ray spectroscopy (EDS) is a technique run in STEM mode with a highly-focused rastered beam. Electrons in the beam passing through the sample displace electrons from their shells and characteristic x-rays are emitted as the electron falls back into its orbital shell. These x-rays are collected and binned according to energy, resulting in a record of which elements and how much are present. EDS is one of the most commonly used analytical tools in electron microscopy for composition, partly due to it being extremely easy to use. As algorithms created to automatically read the resulting spectra and calculate elemental percentages become faster and more accurate, this technique becomes increasingly easy. This technique is particularly useful for heavier elements like transition metals but is often used for lighter elements even as small as O; however, the accuracy detection and thus of calculating atomic percentages decreases quite a bit below Si due to lower x-ray counts from the lighter elements. EDS is particularly nice because line scans or point spectra can often be pulled from the maps to show into what compositions the material separates into and those compositions can be compared to regions of a theoretical diagram if one is available. EDS algorithms occasionally have issues

with sample drift and if elements are close in energy and will report odd things, so it is advisable to check the collected spectrum.

Spatial mapping of relative amounts of different elements can be instrumental for demonstrating phase decomposition pathways where separation into large regions (microns or bigger), for binodal decomposition, or smaller wave-like regions, for spinodal decomposition, occur. In order to confirm the validity of theoretic calculations in the $Sn_{1-x}Ca_xCh$ alloys, which predicted spinodal decomposition for samples with appropriate synthesis conditions, EDS mapping was employed to spatially resolve the chemical variation due to phase decomposition. $Sn_{1-x}Ca_xS$ samples did show spinodal decomposition as evidenced by spatial alternating intensity between Sn and Ca maps, with the results for the sulfide alloy shown in Figure 2.14 and discussed in Section 4.4.1. $Sn_{1-x}Ca_xSe$ samples were not as cooperative for EDS mapping and other methods were employed as discussed in the section below.

4.4 Imaging

4.4.1 Z-Contrast

As a microscope, a TEM can be considered primarily an imaging tool. However, because there are different methods of obtaining said images with the electron beam, different types of information may be extracted from the image. Some of the electrons are diffracted by the lattice of the material's crystal, while others are bent from their straight path through the sample stronger from their straight path than others due to proximity to the nuclei of atoms. The higher the atomic element, the stronger the deflection of the electron. This results in a spread of contrasts for the same image dependent upon the detection angle as shown in Figure 4.1. Images with higher collection angles or shorter camera lengths have bright regions corresponding to electrons deflected to a higher angle than can result from crystal diffraction. Such images are often called Z-contrasted, wherein the brighter the region the heavier the element present. This technique is useful for a general sense of uniformity when studying metastable materials that have elements with a fairly large difference in Z, such as materials in different rows of the periodic table (e.g. Ca and Sn), particularly if there is some concern of separation on a small scale. It is also useful if the sample is very beam sensitive as it does not require the high beam current nor long beam exposure demanded by EDS mapping. Additionally, the collection time (~1 sec) of such an image is much shorter than most EDS maps (often tens of minutes) so sample drift, which can occur in any

direction and may be a major issue in mapping, is unlikely to occur. It is known that EDS detectors also collect a large number of counts from the grid (usually Cu) the sample is attached to, from the sample holder itself (again often Cu, but sometimes Be), and other things within the TEM column. While this can qualitatively give information about the spatial composition of the sample, quantitative data must come from other techniques, such as EDS or EELS point spectra or line scans. Additionally, this technique does not work well if there are two materials of interest in that are close in Z and that need to be resolved (e.g. Cu and Zn).

As mentioned above, a $Sn_{1-x}Ca_xSe$ sample was being tested for spinodal decomposition, but EDS mapping failed to show any compositional modulation, likely due to sample drift. Z-contrast imaging was therefore applied to determine if there as some amount of composition variation. From the image, we could clearly see the sample was not uniform and appeared to have some form of modulation. After z-contrast imaging, EDS line scans were performed to obtain more quantitative information at the appropriate locations. EDS line scans (which take only a few minutes, a fraction of the time a map does) were able to measure a large difference in composition where EDS maps had shown only a uniform sample. The results of these are shown in Figure 2.23 and discussed in section 2.5.1.

4.3.2 BF-TEM-imaging

Bright field (BF) TEM imaging is the result of the majority of electrons transmitted through the sample. These electrons are only lightly deflected or diffracted by the sample (as opposed to the electrons which encounter heavier elements and are deflected to higher angles) causing the regions with lighter elements to appear brighter. BF is also where crystalline regions can be viewed spatially through mapping of lattice fringes. This is useful for metastable materials that may be likely to separate into amorphous and crystalline regions which cannot be distinguished by larger scale methods like XRD or Raman spectroscopy.

An example where this is useful is the study of the MoN_x sample in Figure 4.3. The bulk composition by x-ray fluorescent spectroscopy show a composition of MoN_2, and x-ray diffraction indicates the sample to be rock salt cubic, which is not a phase that was expected and had not yet

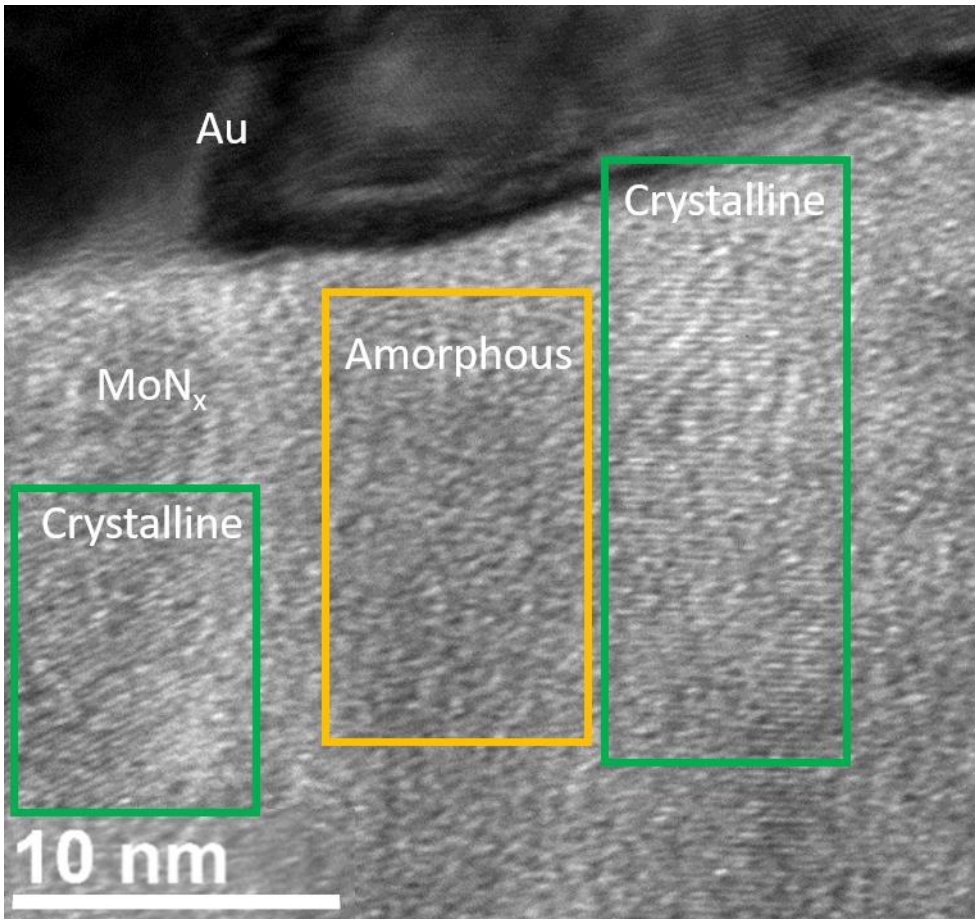

Figure 4.3. MoN_x cross-sectional TEM specimen showing crystalline regions by coherent lines indicating lattice fringes (in the green box) and amorphous regions (in the yellow box).

been observed. However, viewing the focused TEM image with fringes, one can see there are large regions of amorphous material between the crystalline regions. Combining this information with EDS, EELS or some other composition analysis tool helped determine the phase in XRD was more likely cubic MoN since the Mo in the sample appeared to be uniform in EDS but there seemed to be N-rich and -poor regions. However, because N emits very few counts relative to Mo, it is very difficult to accurately map so in this case was not definitive. If instead N had a higher atomic number, it would be easier to correlate with crystalline *vs.* amorphous regions. Even so, this technique can be difficult since the crystalline and amorphous regions may be interspersed enough that it can be difficult to distinguish them after switching to STEM mode (which is necessary for

EDS) and the image often shifts when switching between different settings on the TEM (such as to energy filtered TEM for EELS). So, part of success at mapping the same region analyzed for crystallinity depends on the operator's familiarity with that sample and whether the sample has distinguishable features.

4.4.3 EFTEM-thickness mapping and elemental mapping

Energy-filtered TEM is a technique exploiting the tendency for some electrons to be inelastically scattered when passing through the specimen and thus losing a certain amount of energy dependent upon the elements interacted with. This energy variation amounts to a 'chromatic' variation in the electrons' deflection which can be separated by passage through a magnetic prism (similar to light's chromatic spread after passing through a glass prism). One can select a particular color or energy of electrons to view the image in by placing a slit at the correct spot to filter only that energy. Since particular energy losses correspond to interactions with certain element types, by selecting one particular energy, an image which spatially shows the relative amount of that material can be obtained. Such an image is often obtained by what is called the jump-ratio technique wherein the intensities in an image recorded at the energy of the maximum of absorption peak for the desired element (also known as the post-edge image) is divided by the intensities in an image taken just before that peak (also called the pre-edge image). A jump-ratio image, like the one in Figure 4.4a, usually is only used for qualitative purposes, but, by taking more images at appropriate energies and for other elements, one can refine the image and obtain quantitative information such as elemental ratios, and, if enough images are taken, the electron energy loss spectrum can be constructed. EFTEM imaging can take only a few seconds, so can be helpful with metastable materials that are slightly beam sensative and cannot survive long exposures (minutes to tens of minutes) to the beam often required of EDS mapping, particularly since it only requires two images to be taken. It can also be helpful when EDS fails to distinguish between two materials which have peaks close to one another (a second opinion never hurts). In addition to elemental mapping, EFTEM allows for relative thickness mapping in which the zero-loss image (image from unscattered electrons) is subtracted from the unfiltered image. This is useful for metastable materials since, even when samples appear to be uniform by chemical analysis, non-uniformity in thickness may appear as contrast in images (which might be interpreted as chemical variaitons).

One example of this is a $Sn_{1-x}Ca_xSe$ sample which appeared to have layers in all TEM and STEM images. Because of the layering technique employed to make the samples, these layers were thought to be purely a lack of intermixing. However, the thickness of the observed layers were much larger (~ 10 nm) than those that would occur from the layering process (~1-2 nm). Additionally, EDS maps and line scans showed hardly any variation in composition (±3% Ca). Obtaining the thickness map in Figure 4.4b by EFTEM analysis showed the modulations in contrast seemed to result from a variation in the thickness throughout the sample (lighter is thicker for materials of the same density). This thickness variation likely was a result of focused ion beam thinning during the preparation of the TEM specimen.

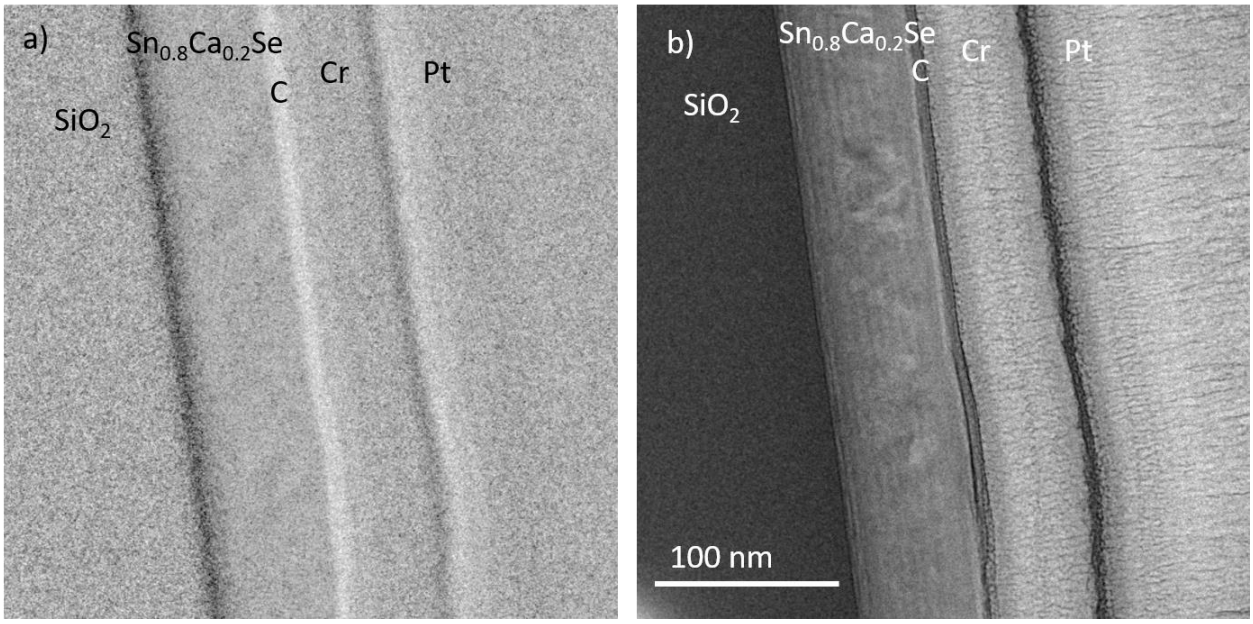

Figure 4.4 a) C jump-ratio EFTEM map of the $Sn_{1-x}Ca_xSe$ sample in b. b) $Sn_{1-x}Ca_xSe$ thickness map.

4.5 In-situ TEM

In-situ TEM, as it sounds, is a technique in which experiments are conducted inside the TEM. The ability to view the material on a microscale as it experiences different external probes is incredibly powerful, particularly when the changes are only observable on the nanoscale such as spinodal decomposition. The innovation in this area is currently quite high and new experiments are rapidly being developed and fine-tuned. Some of the possible basic experiments, many of which can be combined, include: localized sample heating, applying biased voltage, viewing the sample under different environments or atmospheres (instead of the TEM ultra-high vacuum), viewing small

volumes of liquid, and applying mechanical stresses.[4] While all of these are very powerful tools for studying metastable materials only a few will be discussed here for brevity's sake. Because metastable materials are concerned with energy states, an example in-situ electrochemistry will be discussed.

Heating stages in TEMs allow for real-time visualization of crystallization fronts, of compositional phase separation, of compositional intermixing, of evaporation of some species, or of other morphology changes. Thus, these tools provide key information about some of the basic science of metastable materials, particularly what does the cascade from a metastable state to a more stable state look like, but also, at the higher temperatures that can be obtained by localized temperature heating, what do the higher energy states look like.

A more complex in-situ TEM experiment that has only recently achieved viability is electrochemistry. Such an experiment usually requires vacuum-tight, electron-transparent environmental or liquid cells, which means a very small volume of liquid and likely reduced resolution. Some issues may occur as cells of this sort may burst or crack as the window is very thin. Nevertheless, the value of visually recording the crystallization in conjunction with the input voltage and current during these experiments yields invaluable data for materials studies. In addition to the visual data, the (S)TEM techniques discussed previously can be employed, particularly the z-contrasting, which may allow in-situ TEM to provide more information per experiment than other in-situ microscopy techniques. This technique could be particularly helpful in studying metastable materials grown by electrochemistry since each stage of the process may be observed and analyzed by diffraction and spatial chemical analysis and could be easily used for mapping the growth routes of various phases.

One example of an in-situ TEM electrochemical study is by White et al.[5] In the study, they observe the growth of crystalline lead structures on gold plates immersed in a lead nitrate aqueous solution. Applying voltage across the gold, they were able to reversibly plate the cathode and grow lead dendrites (small tree-like structures in the metal which often cause shorts in batteries) of various sizes. They found they could reproducibly cycle the growth of the dendrites and image them at different points in the cycle. Figure 4.5 shows a time series of STEM images of their cycle, the graph below shows the time, voltage, current, and image intensity in the region of interest (ROI, in the green box in a) and the global intensity in the general field of view (G, 'white space' in the

image) for each frame a-l. These images as a time series hold a wealth of information. They found that by inputting current pulses with 10 sec decay times (as shown in the graph) would produce cyclical dendrite growth. The image intensity in ROI correlated with the concentration of Pb^{2+}, and the intensity in G corresponded to the total Pb deposited (since this is an enclosed cell and Pb appears bright in STEM any deposited on the windows would appear bright). These allowed the authors to follow the chemistry and more fully understand what was needed to prevent dendrites from occurring.

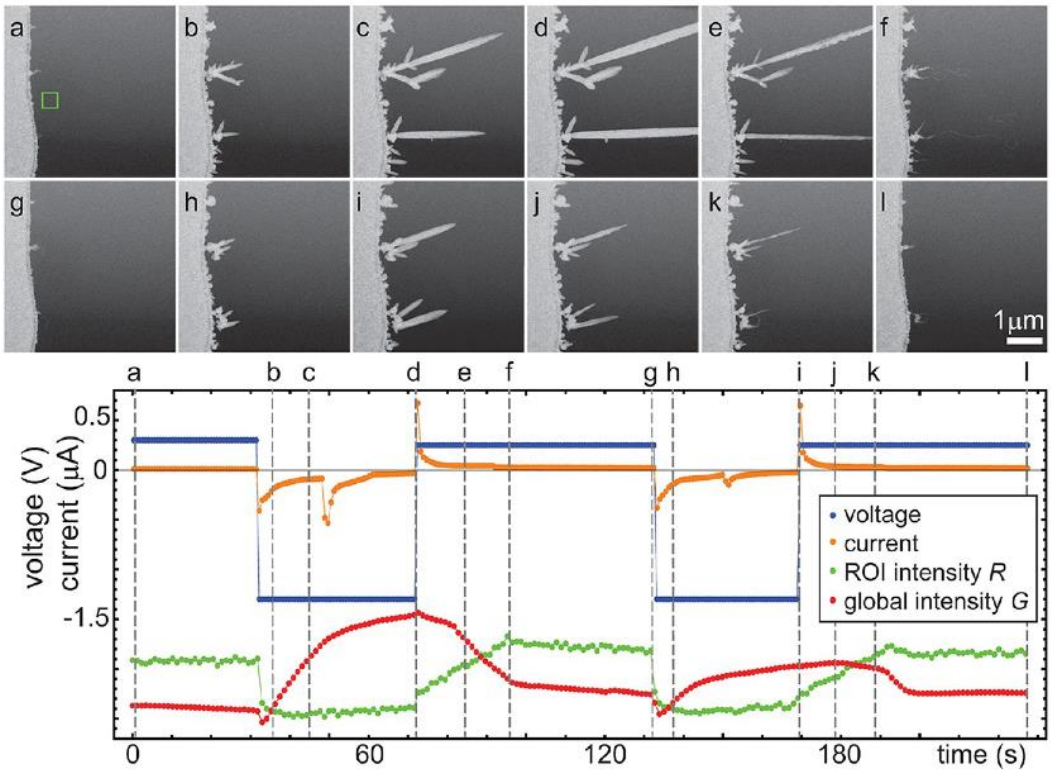

Figure 4.5 a)-l) Time series of STEM images taken at the indicated points in the graph below the STEM images reporting the voltage (blue), current (orange), image intensity in the region of the green box in a (green) and the intensity in the general field of view (red).[5]

4.5 Summary

To conclude S/TEM as a tool for material analysis in general has become extremely powerful. Many of even the simplest techniques can be extended to metastable materials to help understanding of the pathways between states. Here we have outlined a few techniques which are useful for the study of metastable materials. A few examples of where these TEM or STEM techniques are applied and the results for each are described. While these techniques might not be

helpful for every material, and some materials may be too delicate to even image in TEM, they have shown promise for being helpful for a broad range of materials.

---

[1] DENSsolutions in-situ TEM company website www.denssolutions.com

[2]D.A Muller, J. Grazul. "Optimizing the Environment for Sub-0.2 nm Scanning Transmission Electron Microscopy". *J. Electron. Microsc.* **2001.** 50(3). 219–226

[3] X. Sang, A. R. Lupini, R. R. Unocic, M. Chi, A. Y. Borisevich, S. V. Kalinin, E. Endeve, R. K. Archibald, S. Jesse. "Dynamic Scan Control in STEM: Spiral Scans". *Advanced Structural and Chemical Imaging.* **2016.** 2**(**6)

[4] M. L. Taheri, E. A. Stach, I. Arslan, P. A. Crozier, B. C. Kabius, T. LaGrange, A. M. Minor, S. Takeda, M. Tanase, J. B. Wagner, R. Sharma. "Current Status and Future Directions for In Situ Transmission Electron Microscopy." *Ultramicroscopy.* **2016.** 170

[5] E. R. White, S. B. Singer, V. Augustyn, W. A. Hubbard, M. Mecklenburg, B. Dunn, B. C. Regan. "In-situ Transmission Electron Microscopy of Lead Dendrites and Lead Ions in Aqueous Solution." *ACSNANO*. **2012**. 6 (7)

Chapter 5 Conclusion/Summary

5.1 $Sn_{1-x}Ca_xCh$ Alloys

Metastable heterostructural alloys of $Sn_{1-x}Ca_xS$ have been kinetically stabilized in single phase thin films by RF magnetron sputtering and PLD and of $Sn_{1-x}Ca_xSe$ by PLD. PLD deposited alloys are formed by layering of SnCh (Ch = S, Se) and CaCh with low substrate heating (300-500^o C) for layer intermixing. Structural transitions from orthorhombic to rock salt cubic are observed for both $Sn_{1-x}Ca_xCh$ alloys, at x = 0.25 for the sulfide and x = 0.18 for the selenide which are close to the values predicted by theory. Phase decomposition pathways were explored by STEM EDS in cross-sectional TEM specimens which were found to spinodally phase separate, in agreement with the predicted phase diagrams. The agreements between experiment and theory here indicates that metastable materials can be successfully predicted by theory. These metastable alloys represent a new class of interesting alloys which, due to the structural transition, allow for property tuning by both structure and composition.

Optical band gaps were calculated from transmission and reflection measurements for select compositions and compared to predicted values. The $Sn_{1-x}Ca_xS$ band gap trend showed a slight dip near the transition composition where the calculated trend showed a discontinuous drop in the band gap. The direct band gap trend roughly followed the predicted trend, but the indirect band gaps were fairly flat at ~1.5 eV which is close to that of SnS, suggesting there may have been some amorphous SnS in the samples. The $Sn_{1-x}Ca_xSe$ experimental band gap trend followed the predicted trend much more closely. Both $Sn_{1-x}Ca_xS$ and $Sn_{1-x}Ca_xSe$ alloys exhibited p-type conductivity. $Sn_{1-x}Ca_xS$ samples were found to be very resistive; even small additions of Ca to SnS resulted in large increases in the resistivity, from 10^2 Ωcm at SnS to 10^4 Ωcm at x = 0.1. For composition x > 0.1, samples resistances were not reliably measurable. Conversely, $Sn_{1-x}Ca_xSe$ samples were much more conductive and had a very interesting trend, dropping 3 orders of magnitude across the transition composition. Samples initially became more resistive with added Ca (15 Ωcm for SnSe to 30 Ωcm at x = 0.06) until near the transition composition, then became more conductive until about x = 0.4 (0.1 Ωcm at x = 0.16 to 0.02 Ωcm at x = 0.4), after which they rapidly increased in resistivity. In addition to a high conductivity, $Sn_{1-x}Ca_xSe$ exhibited excellent thermoelectric properties. While there was a decrease in the Seebeck coefficient with the increase of conductivity, it was a more modest one order of magnitude, leading to a powerfactor that was more than an order of magnitude higher in the cubic structure than at SnSe in the orthorhombic

structure. The power factor peaked at PF = 2 $\mu W cm^{-1} K^{-2}$ at $x = 0.16$, which is comparable to the standard high performing thermoelectrics like Bi_2Te_3. These successes at stabilizing predicted metastable materials with functional properties confirm that searching the metastable space for new materials, while challenging, can yield novel and extraordinary materials.

While these alloys have very intriguing properties, there is still not a full understanding of why the selenide alloy system becomes more conductive in the rock salt structure and with added Ca. Therefore, one next step for understanding the basic science in these alloys would be defect calculations to explore the mechanism behind the increase in carrier density, which could be very enlightening for future materials design.

5.2 Nitrides

Thin films of transition metal nitrides Zn-W-N and Zn-Mo-W-N are synthesized by RF magnetron sputtering for 30-95 and 25-90 Zn cat% respectively. The predicted WZ structure stable for Zn_3WN_4 is observed and stabilized at room temperature for 60-87 Zn cat%. A WZ phase was also observed in the Zn-Mo-W-N system for 55-80 Zn cat% and was relatively independent of the Mo :W ratio. The optical absorption coefficient determined from transmission and reflectance was above 10^5 cm^{-1} for all Zn-W-N and Zn-Mo-W-N samples, and these samples were more absorbing in the visible and near IR at lower Zn concentrations. Absorption for different Mo : W ratios showed little variation for the same Zn concentration, showing that Zn had the dominant effect on the optical properties. Zn-W-N samples had almost a constant resistivity of 4×10^4 Ωcm in the WZ phase for all compositions. Between 50-60 Zn cat%, samples are amorphous and experience a sharp increase in conductivity of over 2 orders of magnitude with decreasing Zn, resulting in an interesting step-function-like resistivity profile for Zn-rich samples. Zn-Mo-W-N samples are generally much more conductive and exhibit a broader range of resistivities in the WZ phase changing 4 orders of magnitude from 60 Zn cat% (4 Ωcm) to 80 Zn cat% (4×10^4 Ωcm) at a 2:1 Mo : W ratio. Such a profound difference in conductivity between Zn-W-N and Zn-W-Mo-N shows the immense influence that elements have in property manipulation independent of crystal structure. Samples with < 30 Zn cat% were even more conductive (< 1 Ωcm). Cross-sectional TEM specimen were analyzed by STEM EDS to spatially determine film composition. Room temperature samples with concentrations below 30% Zn, far from the stable composition, had W-rich layers, but those grown at 200^o C were more uniform, where a higher temperature allowed

better film homogenization. Many of the optoelectronic properties that are relevant for these two systems, such as the bad gap, carrier mobility, and carrier type. were not thoroughly investigated, so there is still much work to be done in the future. Although a wide range of Zn concentrations was studied for these two nitrides, only the range 25-40 cat% Zn was studied in these systems at higher temperatures (up to 400^{o} C). Because most of the room temperature samples were amorphous, a higher temperature study would help elucidate of what other structures and phases might be accessible in this system. Because of the WZ structure, these two nitrides should exhibit piezoelectric properties, so analysis of which composition and orientation they produce the best piezoelectric coefficients would also be an intriguing study.

5.3 Electron Microscopy

Finally, some electron microscopy techniques were discussed that are useful in studying metastable materials and were employed for both the chalcogenide alloys and the nitride compounds. Energy filtered TEM was used to explore what appeared to be a compositional variation in the form of layers in a $Sn_{1-x}Ca_xSe$ cross-sectional specimen. Energy filtered maps were collected as were thickness maps. Energy filtered elemental maps showed the sample to be fairly uniform, but the thickness map clearly showed the variation in thickness of the cross-section. Z-contrasted STEM images were used to show composition variation in a spinodally decomposed $Sn_{1-x}Ca_xSe$ TEM specimen (which was finally confirmed by an EDS line scan), while EDS mapping failed to show any variation. BF TEM images were used in conjunction with lattice fringes to map the relative regions of crystallinity in a MoN_x sample and compared to EDS maps of the nitrogen content to ascertain whether the crystalline phase observable by XRD was N-rich or not. These examples show that electron microscopy offers a variety of techniques that may be used together to form a full picture of the structure and composition of alloyed matrials, which is particularly important in metastable materials.